

**ANALYZING THE THREE-DIMENSIONAL
DEFORMATION BEHAVIOUR OF AN EMPTY
CANDU FUEL BUNDLE USING THE FINITE
ELEMENT METHOD**

**ANALYSE DU COMPORTEMENT DE LA
DÉFORMATION TRIDIMENSIONNELLE D'UNE
GRAPPE DE COMBUSTIBLE CANDU VIDE À
L'AIDE DE LA MÉTHODE DES ÉLÉMENTS FINIS**

A Thesis Submitted to the Division of Graduate Studies
of the Royal Military College of Canada
by

2Lt. Rabia Soni

In Partial Fulfillment of the Requirements for the Degree of
Masters of Applied Science

March 2017

© This thesis may be used within the Department of National Defence but
copyright for open publication remains the property of the author.

ACKNOWLEDGEMENTS

I would like to thank my supervisors, Dr. Paul Chan and Dr. Diane Wowk, for providing me with this opportunity. The mentorship and the expertise they have offered throughout the past two years have been an instrumental component of this work. Additional gratitude to them is warranted for providing me the incredible opportunity to work at the Canadian Nuclear Laboratories for three months. I would like to thank Dr. Anthony Williams, whose supervision and assistance with ANSYS at CNL was crucial in helping me achieve the challenging objectives of my thesis research. Additionally, it would be remiss of me if I did not acknowledge the modeling guidance of my colleagues at CNL, in particular Dr. Markus Piro and Dr. Andrew Prudil, and Dr. Bonin`s assistance with the translation of the abstract.

I would like to acknowledge CNL and COG for providing the experimental data that supported the development of a 3-D computational fuel bundle model. I would also like to extend my gratitude to Kathy Colins, Ray Dickson, and Catherine Thiriet for answering my queries about the setup and results of the bundle heat-up experiment. Their skill facilitated the development of the model presented in this work.

I am grateful to Defense Research and Development Canada (DRDC) for providing me with the opportunity to pursue this research endeavor. The provision of funds and resources by the Department of National Defense (DND) and Natural Sciences and Engineering Research Council of Canada (NSERC) are also appreciated.

Most of all, I would like to thank my family and friends. Their love, encouragement and support throughout the past two years have been immense.

ABSTRACT

Soni, Rabia. (Nucl. Eng.). Royal Military College of Canada, March 2017. Analyzing the Three-Dimensional Deformation Behaviour of an Empty CANDU Bundle Using the Finite Element Method. Supervisors: Dr. Paul Chan and Dr. Diane Wowk.

During off-normal or accident conditions, a CANDU fuel bundle may be subjected to thermal and mechanical loads when it is heated above its normal operating temperature. In these conditions, the fuel elements may deform due to two mechanisms: bowing of the fuel elements due to changes in mechanical properties caused by thermal gradients and sagging of the fuel elements under their self-weight. The resulting deformation may impede heat transfer from the fuel elements to the coolant and exacerbates the cooling of the bundle. Therefore, it is important to understand and quantify the conditions under which the fuel bundle will sufficiently deform such that the coolant flow distribution and the ability of the coolant to cool the fuel is not adversely impacted.

A model capable of predicting the fuel performance and the 3-D deformation of a bundle has not been developed yet. This thesis presents a detailed 3-D deformation model of an empty fuel bundle in order to set the stage for the development of such a model. The bundle deformation model presented in this work is capable of simulating the sag of the elements and the end-plates, differential thermal expansion of the bundle, fuel element bowing, and creep deformation of the bundle. The deformation results were validated against experimental results, which were made available for the first time for simulation purposes by Canadian Nuclear Labs (CNL). The results show good agreement with the experimental results, indicating that the model was able to capture the overall trends observed in the experiment. The feasibility of a bundle deformation model, which includes contact between adjacent elements, non-uniform temperature gradients, and creep deformation at off-normal conditions, was demonstrated.

RÉSUMÉ

Soni, Rabia. (Nucl. Eng.). Collège militaire royal du Canada, Mars 2017. Analyse du Comportement de la Déformation Tridimensionnelle d'une Grappe de Combustible CANDU Vide à l'aide de la Méthode des Éléments Finis. Directeurs de thèse: Dr. Paul Chan et Dr. Diane Wowk.

En cas de conditions accidentelles, une grappe de combustible CANDU peut être soumise à des charges thermiques et mécaniques lorsqu'elle est chauffée au-delà de sa température normale de fonctionnement. Dans ces conditions, les éléments de combustible pourraient se déformer selon deux mécanismes: la flexion des éléments de combustible à cause des changements de propriétés mécaniques provoqués par des gradients thermiques, et l'affaissement des éléments de combustible sous leur propre poids. La déformation résultante peut restreindre le transfert de la chaleur des éléments de combustible vers le caloporteur et nuire au refroidissement de la grappe. Il est donc nécessaire de comprendre et de quantifier les conditions dans lesquelles la grappe de combustible se déforme suffisamment afin que la distribution du flux de caloporteur et sa capacité à refroidir le combustible nucléaire ne soient pas affectées négativement.

Un modèle capable de prédire la performance du combustible et la déformation 3-D d'une grappe entière n'a pas encore été développé. Cette thèse présente un modèle de déformation 3-D détaillé d'une grappe de combustible vide afin de préparer la voie pour le développement d'un tel modèle. Le modèle de déformation présenté dans ce travail est capable de simuler l'affaissement des crayons de combustible et des plaques d'extrémité, la dilatation thermique différentielle de la grappe, l'inclinaison des éléments de combustible et la déformation par fluage de la grappe. Les résultats de la déformation ont été validés en comparant avec des données expérimentales qui ont été mises à disposition pour la première fois pour les besoins de la simulation par les Laboratoires Nucléaires Canadiens. Les résultats montrent un bon accord avec les résultats expérimentaux. Ceci indique que le modèle a correctement prédit les tendances globales observées dans l'expérience. On a démontré la faisabilité d'un modèle de déformation d'une grappe qui inclut le contact entre des éléments adjacents, des gradients de température non uniformes et une déformation par fluage dans des conditions accidentelles.

TABLE OF CONTENTS

SECTION	PAGE NUMBER
LIST OF FIGURES	VIII
LIST OF TABLES	XII
LIST OF ACRONYMS	XIII
LIST OF SYMBOLS	XIV
1 INTRODUCTION	1
2 RESEARCH OBJECTIVES	8
3 BACKGROUND	10
3.1 DRY-OUT CONDITIONS	10
3.2 TRIP PARAMETER FOR SAFETY ANALYSIS	12
3.3 DEFORMATION MECHANISMS	13
3.3.1 Elastic Deformation	13
3.3.2 Plastic Deformation	15
3.3.2.1 Yield Criterion	15
3.3.2.2 Hardening Rule.....	16
3.3.3 Thermal Expansion.....	18
3.3.4 Creep.....	19
3.4 FUEL ELEMENT BOWING	21
3.5 SHEATH OXIDATION	22
3.6 PRESSURE TUBE CREEP AND GROWTH	23
4 STATE OF ART	26
4.1 INDUSTRY STANDARD TOOLSET	26
4.2 MULTIPHYSICS MODELS	27
5 MODEL DEVELOPMENT	34
5.1 FINITE ELEMENT METHOD.....	34
5.1.1 Nonlinear Simulations	37
5.1.2 Contact Algorithms.....	38
5.1.3 Newton-Raphson Method.....	42
5.2 FUEL BUNDLE HEAT-UP EXPERIMENT.....	43
5.3 MATERIAL PROPERTIES	47
5.3.1 Zircaloy-4 Properties	47
5.3.1.1 Density.....	48
5.3.1.2 Modulus of Elasticity.....	48
5.3.1.3 Material Plasticity.....	49
5.3.1.4 Poisson’s Ratio	50
5.3.1.5 Thermal Expansion.....	50

5.3.1.6 Creep.....	51
5.3.2 Quartz Properties	52
6 PRELIMINARY MODELS.....	54
6.1 FLEXURAL RIGIDITY	54
6.2 THERMAL BOWING	59
6.3 CREEP DEFORMATION	64
6.4 CONCLUSION	69
7 FUEL ELEMENT DEFORMATION MODEL.....	70
7.1 MODEL DESCRIPTION	70
7.1.1 Physical Geometry.....	71
7.1.2 Material Properties.....	71
7.1.3 Element Type and Mesh	71
7.1.4 Loading and Boundary Conditions.....	76
7.1.5 Solution.....	79
7.2 RESULTS	80
7.3 DISCUSSION	86
7.3.1 Creep Deformation	86
7.3.2 Model Validation	89
7.4 CONCLUSION	92
8 FUEL BUNDLE DEFORMATION MODEL	93
8.1 MODEL DESCRIPTION	93
8.1.1 Physical Geometry.....	94
8.1.2 Material Properties.....	96
8.1.3 Element Type and Mesh	96
8.1.4 Loading and Boundary Conditions.....	99
8.1.4.1 Contact Modeling	99
8.1.4.2 Temperature Distribution.....	104
8.1.4.3 Boundary Conditions	106
8.1.5 Solution.....	108
8.2 RESULTS	108
8.3 DISCUSSION	115
8.3.1 Creep Deformation	117
8.3.2 Model Validation	122
8.3.3 Limitations	130
8.4 CONCLUSION	132
9 SUMMARY AND CONCLUSIONS.....	134
10 REFERENCES	136

APPENDICES.....	139
APPENDIX A – EXPERIMENTAL RESULTS.....	140
APPENDIX B – SAMPLE CALCULATIONS	144
APPENDIX C – INITIAL CONTACT INFORMATION	148

List of Figures

Figure 1: Schematic of a CANDU reactor. Image courtesy of The Essential CANDU textbook [1].....	2
Figure 2: Detailed schematic of a 37 element CANDU fuel bundle. Reproduced with permission from [7].	3
Figure 3: Schematic view of a CANDU fuel bundle and the reactor vessel. Reproduced with permission from [7].	4
Figure 4: Illustration of the two-phase flow patterns occurring in a heated horizontal channel. Reproduced with permission from [1]	11
Figure 5: Von-Mises yield surface in the 3-D σ_1 - σ_2 - σ_3 space. Reproduced with permission from [21].	16
Figure 6: Behaviour of the kinematic hardening model. Image courtesy of [21].....	17
Figure 7: Behaviour of the isotropic hardening model. Image courtesy of [21].	18
Figure 8: Deformation graph showing the stress and temperature domains where different creep mechanisms are most likely to occur. μ is the shear modulus and T_m is melting temperature of Zircaloy. Image courtesy of [28]......	20
Figure 9: Pressure Tube Sag. Image courtesy of [35].	24
Figure 10: Interpenetration of the contact and target surfaces when no contact compatibility is specified. Image courtesy of ANSYS, Inc. [46]......	40
Figure 11: Schematic illustrating the penalty method. Image courtesy of Ansys, Inc.[46].	41
Figure 12: Bilinear plasticity model for Zircaloy-4.....	49
Figure 13: Dimensioned drawings of (a) the sheath cross-section, (b) the fuel sheath, and (c) the brazed appendages. All measurements are given in mm.....	55
Figure 14: Boundary and loading conditions of the flexural rigidity model.	57
Figure 15: Vertical deformation of the flexural rigidity model [mm]......	57
Figure 16: Temperature gradient of 200 K across the diameter of the sheath.....	61

Figure 17: Deflection of the fuel element due to thermal gradients ranging from 50 K to 200 K.	62
Figure 18: Boundary conditions of the creep verification model.	66
Figure 19: Strain as a function of time.	66
Figure 20: Comparison of simulation and analytical creep strain.	68
Figure 21: Physical structure used in the fuel element deformation model.	71
Figure 22: Finite element mesh of the solid (left) and shell-solid models (right).	73
Figure 23: Total deformation of the fuel element using the solid model and the shell-solid model.	73
Figure 24: Composite mesh composed of higher order elements for the fuel element deformation model.	76
Figure 25: Contact pairs of the 3-D shell-solid assembly.	77
Figure 26: Loading and boundary conditions of the assembly.	78
Figure 27: Axial deformation of the fuel element in [mm].	80
Figure 28: Cylindrical coordinate system.	81
Figure 29: Diametric deformation of the fuel element.	82
Figure 30: Vertical displacement across the length of the fuel element [mm].	83
Figure 31: Normalized vertical deflection of the fuel element due to bending [mm].	83
Figure 32: Equivalent Von-Mises stress [MPa] across the fuel element due to bending. .	84
Figure 33: Equivalent Von-Mises stress [MPa] at the bearing pads.	85
Figure 34: Equivalent Von-Mises stress [MPa] at the bottom of the fuel element as a function of time.	87
Figure 35: Strain as a function of time.	88
Figure 36: Image of the physical structure used in the fuel bundle deformation model. ..	94

Figure 37: Dimensional drawings of (a) the end-plate, (b) the fuel bundle, and (c) the pressure tube. All measurements are given in mm.	95
Figure 38: Mesh of the (a) end-plate and the end-caps; and (b) partial empty fuel bundle of 12 elements.	97
Figure 39: Bonded Contact between the edges of the element and end-cap.	98
Figure 40: Higher order quadrilateral mesh of the quartz tube	99
Figure 41: Numbering convention of the fuel bundle.	100
Figure 42: Contact between the spacer pads of adjacent elements. The contact surfaces (red) were represented by CONTA174 elements while target surfaces (blue) were represented by TARGE170 elements.	102
Figure 43: Entire assembly and cross-section of the geometry of two adjacent fuel elements.	103
Figure 44: Reaction of the element on the right in response to applied load.	104
Figure 45: Variable temperature load from the experiment. Reproduced from [17].	105
Figure 46: Temperature distribution of the partial bundle in ANSYS in [K].	106
Figure 47: Loading and boundary conditions of the assembly.	107
Figure 48: Images illustrating the (a) axial deformation of the partial bundle, and (b) deformation behaviour of the upstream (left) and downstream (right) end-plates.	109
Figure 49: Vertical deformation of the partial bundle [mm].	111
Figure 50: Lateral deformation of the partial bundle [mm].	113
Figure 51: Equivalent Von-Mises stress [MPa] of the bearing pads (left) and the partial bundle without the end-plates (right).	114
Figure 52: Radial bow of the partial assembly.	116
Figure 53: Predicted radial bow of outer elements. Reproduced from [59].	117
Figure 54: Equivalent Von-Mises stress at the downstream end of the fuel element as a function of time.	118

Figure 55: Strain as a function of time.	119
Figure 56: (a) Lateral gap between elements 8 and 9 as a function of time; and (b) Vertical gap between elements 9 and 24 as a function of time.	120
Figure 57: Radial deformation results of element 7 from the experiment (left) and simulation (right).	122
Figure 58: Radial deformation results of element 8 from the experiment (left) and simulation (right).	123
Figure 59: Radial deformation results of element 9 from the experiment (left) and simulation (right).	124
Figure 60: Radial deformation results of element 10 from the experiment (left) and simulation (right).	125
Figure 61: Radial deformation results of element 11 from the experiment (left) and simulation (right).	125
Figure 62: Radial deformation results of element 12 from the experiment (left) and simulation (right).	126
Figure 63: Radial deformation results for the outer elements at (a) 150 mm and (b) 300 mm along the length of the element.	127
Figure 64: Lateral and vertical deflections and radial deformation as a function of the axial position of elements 7 and 8 during high-temperature phase.	141
Figure 65: Lateral and vertical deflections and radial deformation as a function of the axial position of elements 9 and 10 during high-temperature phase.	142
Figure 66: Lateral and vertical deflections and radial deformation as a function of the axial position of elements 11 and 12 during high-temperature phase.	143

List of Tables

Table 1: Comparison of Industry and Multiphysics Nuclear Fuel and Bundle Deformation Models.	33
Table 2: Diffusional Creep Constants.....	51
Table 3: Material Properties of Fused Quartz.....	53
Table 4: Validation of Sheath Rigidity Results.	58
Table 5: Comparison of Deflection Results due to Thermal Bowing.	63
Table 6: Comparison of the Results of the Solid and Shell Models to the Analytical Solution.....	74
Table 7: Comparison of the Deformation Results of the Fuel Element Model with the Analytical Solution.	89
Table 8: Comparison of deformation results between the two load steps.	90

List of Acronyms

AECL	Atomic Energy of Canada Limited
BC	Boundary Condition
BOW	Computer code to predict lateral deflections of composite beams
BWR	Boiling Water Reactor
CANDU	CANada Deuterium Uranium
CHF	Critical Heat Flux
CNSC	Canadian Nuclear Safety Commission
CNL	Canadian Nuclear Laboratories
CTF	Curvature Transfer Factor
dof	degrees of freedom
DO	Dry-out
ELESTRES	ELEment Simulation and sTRESses
ELOCA	Element Loss of Coolant Analysis
FEA	Finite Element Analysis
FEM	Finite Element Method
FP	Fission Products
HT	Heat Transfer
HORSE	HORizontal nuclear fuel Simulation Environment
IST	Industry Standard Toolset
LB-LOCA	Large Break Loss of Coolant Accident
LOCA	Loss of Coolant Accident
LWR	Light Water Reactor
MATPRO	MATerial PROperties library
MOOSE	Multiphysics Object-Oriented Simulation Environment
NOC	Normal Operating Conditions
PDE	Partial Differential Equation
PDO	Post-dry-out
PHTS	Primary Heat Transport System
PT	Pressure Tube
PWR	Pressurized Water Reactor
REF	Rigidity Enhancement Factor
RMCC	Royal Military College of Canada
SCC	Stress Corrosion Cracking

List of Symbols

α	Coefficient of Thermal Expansion
d	Grain Size
E	Young's Modulus
ϵ_{xx}	Strain
$\dot{\epsilon}_{gb}$	Creep Rate due to Grain Boundary Sliding (Diffusional Creep)
F	Creep Rate Coefficient
G	Shear Modulus
k	Thermal Conductivity Coefficient
ν	Poisson's Ratio
Q	Activation Energy divided by Universal Gas Constant
R	Universal Gas Constant
σ_a	Applied Stress
δ	Displacement

1 Introduction

It is universally acknowledged that for a nation to be prosperous, uninterrupted access to an energy source is crucial. Supply of energy empowers nations to invent new technology and provides opportunities for economic growth. Nations with readily available sources of energy have developed rapidly while other nations have had to use their resourcefulness to generate power and energy to facilitate economic development [1]. Generating electrical power through fossil fuels produces pollutants such as fly ash and sulphur dioxide, which adversely impact the environment [2]. In order to reduce anthropogenic climate change, nuclear power generation is a viable long-term solution.

In Canada, the pressurized heavy water CANDU®¹ (CANada Deuterium Uranium) reactor is used for generating electric power. A CANDU power plant generates electricity in a manner similar to generation sites that use fossil fuels. The heat generated from the reactor is used to boil water and generate high-pressure steam. The steam is expanded in the turbine producing work, which is used by the electrical generator to produce electricity [3]. The energy conversion process is illustrated in Figure 1.

The heat generated by the CANDU reactor is produced by nuclear fission of natural uranium, which contains 0.71 wt% fissile isotopes of U-235. Nuclear fission occurs when the nucleus of the heavy atom (U-235) is split into two smaller nuclei through the absorption of a slow neutron, called thermal neutron. For every U-235 fission event that occurs, approximately 200 MeV of kinetic energy is liberated, along with radioactive fission products, energetic or fast neutrons and heat [4].

CANDU® is a registered trademark of Atomic Energy of Canada Limited (AECL).

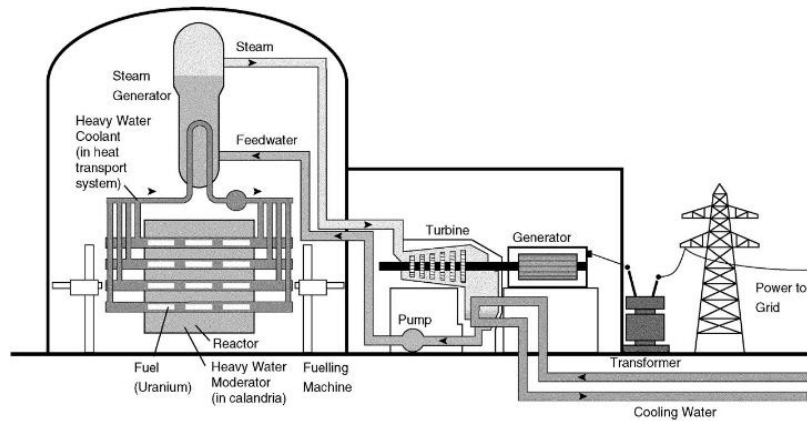


Figure 1: Schematic of a CANDU reactor. Image courtesy of The Essential CANDU textbook [1].

Fast neutrons cannot sustain the fission chain reaction and must be slowed down using a moderator such as heavy water to ensure that further fissions can be induced. Slowing fast neutrons increases the probability of generating more neutrons and of establishing a chain reaction [1, 5].

As stated above, CANDU reactors use natural uranium as nuclear fuel in the form of sintered ceramic pellets of uranium dioxide (UO_2). These pellets are contained within Zircaloy-4 sheaths, which are comprised of cylindrical tubes with bearing and spacer pads brazed to the outer surface. The alloy is used to manufacture the fuel sheath because it absorbs fewer neutrons compared to alternative materials and allows for the fission chain reaction to be sustained. The fuel sheath provides a collapsible support structure for the UO_2 fuel in order to improve heat transfer from the fuel pellets to the coolant to prevent fuel melting [6]. Furthermore, the sheath contains the radioactive fission products generated in the fuel.

With UO_2 pellets stacked inside it, the fuel sheath is sealed at both ends with endcaps to form a fuel element. Individual fuel elements are welded onto endplates to form a fuel bundle. Depending on reactor design, the fuel bundle may be composed of 19 to 43 individual fuel elements [1]. The fuel bundles are contained in pressure tubes that have heavy water coolant flowing through them. The spacing between the fuel elements is maintained by brazed spacer pads on the outer surface of the sheath and the spacing between the fuel bundle and pressure tube is maintained by brazed bearing pads on the outer fuel elements of the bundle [3]. The geometric configuration of the 37 element fuel bundle is shown in Figure 2.

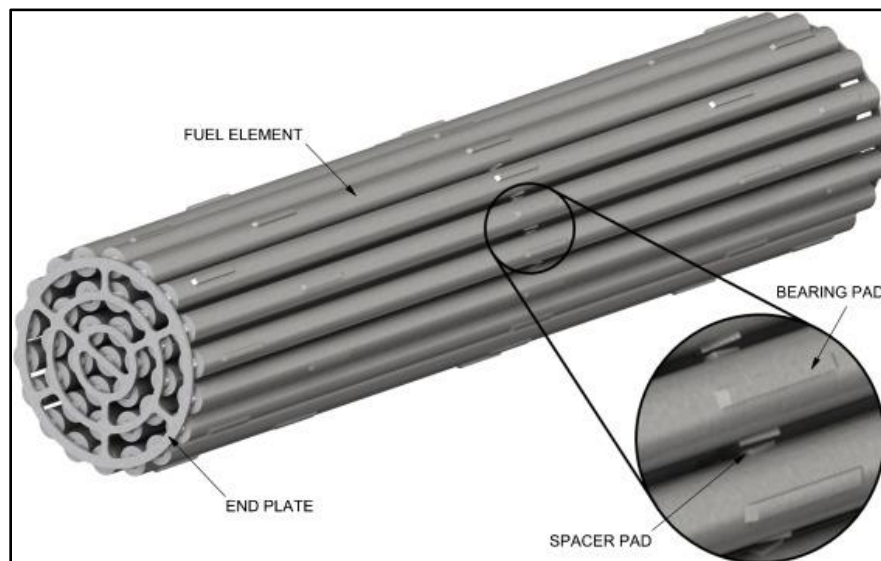


Figure 2: Detailed schematic of a 37 element CANDU fuel bundle. Reproduced with permission from [7].

The spacing between each element forms passages in the pressure tube, called sub-channels, where heavy water can pass to extract the heat generated from the fission reaction. The pressure tube is enclosed within a calandria tube in a horizontal arrangement

as illustrated in Figure 3. To keep the coolant from heating the unpressurized heavy water moderator contained in the calandria, the pressure tube and the calandria are separated by garter springs and the remaining space is filled with carbon dioxide acting as a thermal insulator to limit the heat lost to the moderator [8].

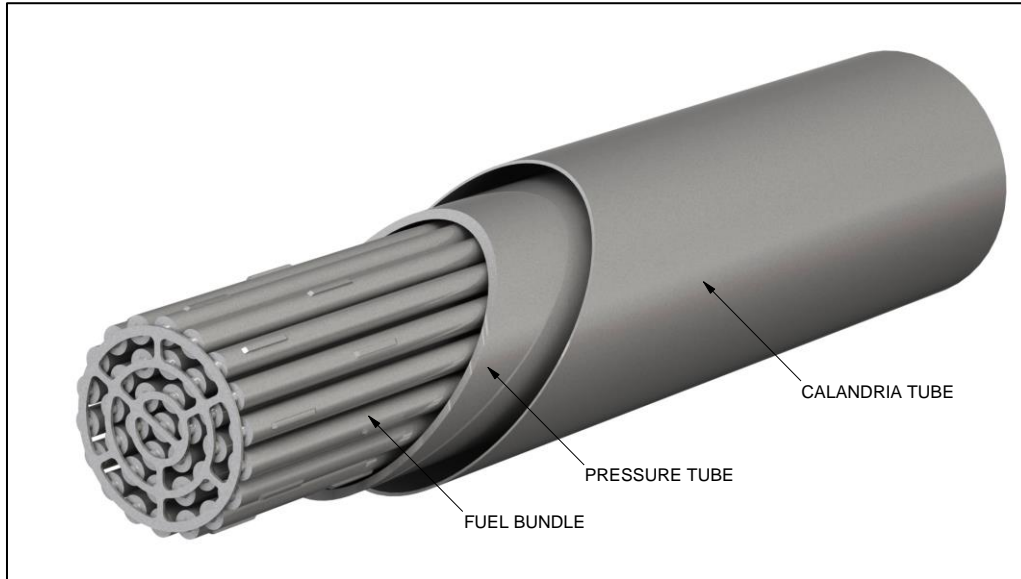


Figure 3: Schematic view of a CANDU fuel bundle and the reactor vessel. Reproduced with permission from [7].

Over the course of its residence in a nuclear reactor, a CANDU fuel bundle is subjected to a standard operating range of thermal and mechanical loads. These loads would be exceeded when it is heated above its normal operating temperature. In these conditions, the fuel elements may deform by two mechanisms: by bowing of the fuel elements due to differential thermal expansion caused by thermal gradients or by sagging of the fuel elements due to gravity [9]. The resulting deformation alters the coolant flow distribution through the bundle such that there is less flow between some sub-channels, and the coolant goes over the top of the bundle [10] [11]. Due to the reduced coolant flow

in the sub-channels, localized undercooling occurs. This impedes heat transfer from the fuel elements to the coolant causing further deformation and reduces the cooling of the bundle [3]. Hence, it is important to understand and quantify the conditions under which the fuel bundle will deform such that the coolant flow distribution and the ability of the coolant to remove heat from the reactor core is not adversely impacted.

During anticipated operational occurrences and design based accidents, a specific safety concern is the bowing deformation of the fuel elements. Thermal differentials across the length or the radius of the fuel element may cause it to bow into contact with the pressure tube [9]. The thermal and mechanical loading on the pressure tube due to contact with the fuel elements could compromise the integrity of both the fuel elements and the pressure tube. The compromised fuel sheath and pressure tube are important reactor safety concerns as they may lead to fuel failure and the subsequent release of fission products to the environment. In order to prevent direct and consequential fuel failure, the Canadian Nuclear Safety Commission (CNSC) has published trip parameters for the reactor shutdown systems such that the integrity of the fuel and of the primary heat transport system is maintained.

Given limited existing experimental data on fuel bundle behaviour, there exists a potential to relax the trip parameters if it can be conclusively demonstrated that the fuel geometry and fuel sheath integrity are maintained under transient conditions. An improvement in the optimization of reactor operation margins would result in the production of a greater amount of energy from the same amount of raw fuel while decreasing the amount of radioactive waste produced. There is a significant interest in

maximizing the amount of power that can be yielded safely from existing nuclear power reactors.

The ability to model the deformation behaviour of a fuel bundle accurately during transient conditions would provide valuable insight into improving CANDU reactor operational margins and preventing fuel failure. In the past, some research efforts have been directed towards the development of such a model; however, these models have typically used beam elements to represent the fuel element [12] [13]. There are concerns that the use of composite beam elements simplifies the fuel element geometry and cannot adequately capture the fuel pellet-to-fuel sheath interaction that contributes to the bowing and sagging behaviour of the fuel bundle [14] [15].

A model capable of predicting the deformation for a full bundle has not been developed and accepted by the CANDU industry. It is necessary to have this type of model for refining the safety margins in reactor licensing. A complete model would be able to simulate the fuel performance and the mechanical response while taking into account the interaction between the pellets and the sheath and the dynamics of the coolant flow. It would also need to be valid over a range of temperatures, extending to off-normal conditions. As a necessary first step in developing such a model, this thesis presents a detailed 3-D finite element model of an empty fuel bundle. The model focuses on predicting the mechanical behaviour of the bundle by excluding fuel-related phenomena. It considers the complex interaction between adjacent fuel elements under conditions similar to those of dry-out and Large-Break Loss of Coolant Accident (LB-LOCA). The deformation results will be compared to the results generated during the fuel bundle heat-

up experiment conducted by Canadian Nuclear Labs (CNL). This model sets the groundwork for fuel pellets and the corresponding phenomena to be added later such that a comprehensive licensing tool capable of predicting fuel performance and 3- D bundle deformation can be realized.

This thesis is the first attempt at modeling the deformation of a full bundle, albeit without fuel pellets. In the lead-up to the development of the bundle deformation model, a number of preliminary models were developed to prove that deformation, creep, and non-uniform temperature gradients were being simulated correctly. The general deformation behaviour of a single fuel element was also modeled to illustrate confidence in the results of the bundle deformation model.

2 Research Objectives

The goal of this thesis is the development of a 3-D Finite Element model to predict the geometric deformation of an empty CANDU fuel bundle in response to given thermal and mechanical loads occurring under conditions similar to those of dry-out, such as small- and Large-Break Loss of Coolant Accident (LB-LOCA). This is to be accomplished using the commercial finite element analysis software, ANSYS, to represent the complex interaction between adjacent fuel elements and between the outer fuel elements and the pressure tube. This work is an evolution of the model previously developed at the Royal Military College of Canada by Krasnaj [16].

This fuel bundle deformation model focuses on contact between adjacent elements and between the bundle and the PT by excluding UO_2 fuel pellets and fuel-related phenomena. Isolating the deformation behaviour of an empty bundle under transient conditions is the first step in the lead up to the development of a more comprehensive fuel bundle deformation model. Although it would be desirable to develop a 3-D model capable of predicting both fuel performance and deformation, the development of that model is not the objective of this thesis given the complexity of the issue. The intent is to utilize the robust numerical contact algorithms in ANSYS to simulate the response of an empty fuel bundle to thermal conditions that may result in contact between adjacent fuel elements and between the outer fuel elements and the pressure tube.

The deformation model represents the thin fuel sheath using 3-D shell elements rather than one-dimensional thin-walled tube approximations used in some models [12]. This ensures that when fuel pellets are eventually added to this model, the fuel pellets and

sheath will be modeled as separate components. Modeling the pellets and sheath as separate components reduces the simplifying assumptions currently used in existing CANDU deformation models by allowing the interaction between the pellets and the sheath to be simulated directly. The interaction can change for different conditions.

Furthermore, the model seeks to provide insight into the bowing and sagging deformation of the fuel bundle under transient conditions. Bowing of the fuel elements can greatly affect fuel coolability and pressure tube integrity because bowed elements may reduce sub-channel flow or come into contact with the pressure tube. Since fuel coolability and pressure tube integrity are important reactor safety concerns, examining the deformation behaviour of the fuel bundle is crucial in understanding the influence of deformation on the sub-channel geometry and the ability of the fuel to maintain its coolable geometry.

The thermal-mechanical loading conditions and the boundary conditions applied in this deformation model mimic those of an empty bundle heat-up experiment conducted by CNL [17]. This ensures that the model can be validated subsequently against the experimental deformation results provided by CNL to demonstrate proof of concept.

3 Background

The aim of this section is to provide the background knowledge relevant to this thesis. Section 3.1 describes the transient conditions that are of interest to the development of the deformation model. This provides context to the significance of this simulation with respect to the safety of the fuel bundle in the reactor core. Section 3.2 details the current trip parameters that govern the operational margin of the reactors. Section 3.3 reviews the multiple mechanisms that contribute strains and deformation to the material. Section 3.4 explains the mechanisms and the relevance of bowing phenomena in fuel bundle deformation models. Section 3.5 briefly outlines sheath oxidation and its impact on sheath deformation. Finally, Section 3.6 describes the long-term deformation of the pressure tube under temperatures of interest in off-normal conditions due to creep.

3.1 Dry-out Conditions

In order to ensure safe operation of CANDU reactors, the fuel elements must be continuously cooled. The surfaces of the fuel elements are surrounded by pressurized heavy water to remove the heat generated by fission [6]. The heavy water serves a two-fold purpose as it cools the fuel elements and facilitates energy transfer by forced convection. At low sheath temperatures of 603 K, the heat transfer regime in a horizontal heated channel corresponds to single-phase flow between the fuel elements and the coolant. During transient conditions, the surface temperature of the sheath increases. When the liquid adjacent to the sheath is superheated, bubbles begin to nucleate on the sheath surface due to latent heat of evaporation. The bubbles encounter the surrounding coolant and condense, releasing latent heat of vaporization to the coolant [18]. This process

initially improves heat transfer because of increased turbulence near the sheath and the evaporation of the liquid. It can be argued that a minimal increase in sheath temperature is a small compromise for operating at optimal heat flux.

However, if the heat flux of the system continues to increase beyond critical heat flux (CHF) such that continuous liquid contact can no longer be maintained on the surface of the heated fuel element, the bubble density increases to the point that they begin to impede liquid flow back to the surface of the sheath [3]. The bubbles coalesce, forming voids that reduce the rate of heat transfer and subsequently increase the sheath temperature [18]. The increase in the superheating of the sheath results in the entire sheath being blanketed by vapor which strips liquid film on the surface of the sheath. Due to the lack of liquid film which typically cools the fuel sheath, the sheath overheats and dry-out occurs. This flow regime is illustrated in Figure 4.

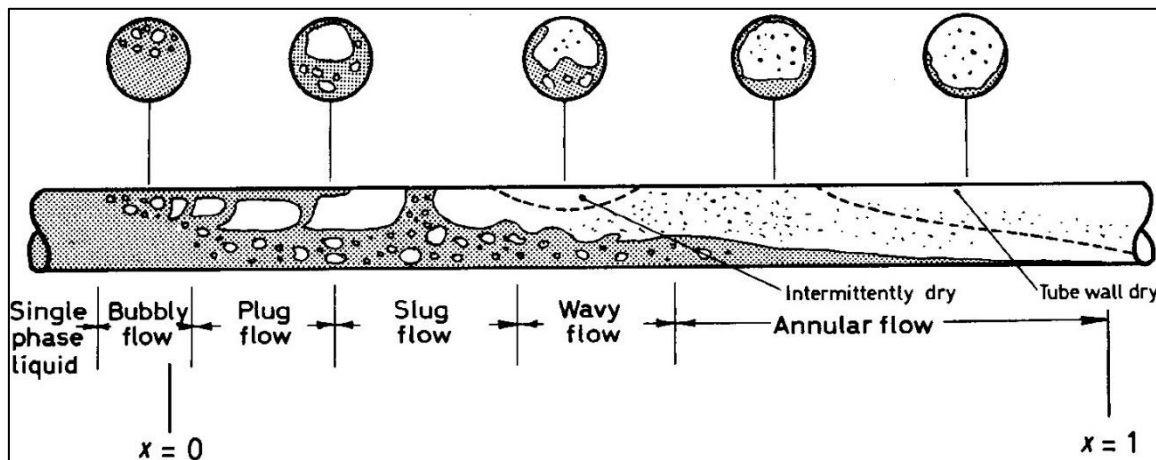


Figure 4: Illustration of the two-phase flow patterns occurring in a heated horizontal channel. Reproduced with permission from [1].

Some scenarios leading to dry-out are loss of power regulation, pump trip, small and large break loss of coolant accidents [11]. Post-dry-out heat transfer is initiated at heat flux

levels above CHF and continues until the sheath is quenched. During post-dry-out heat transfer, the fuel elements may experience differential thermal expansion due to non-uniform heating. The non-uniform heat transfer between the fuel and the fuel sheath may result in deteriorated cooling capacity of the fuel sheath due to changes in sheath geometry and integrity.

3.2 Trip Parameter for Safety Analysis

The Canadian Nuclear Safety Commission (CNSC) is the regulatory body of nuclear power and materials in Canada. In order to provide guidance to licensees who wish to operate CANDU nuclear power plants, the CNSC published the regulatory guide G-144 specifying trip parameters that preclude direct or consequential reactor fuel and PT failure under all design based accidents. The performance requirement for reactor shutdown systems state that the integrity of the fuel and of the primary heat transport system should not be compromised. Since dry-out results in fuel failure and/or PT failure, the avoidance of fuel sheath dry-out is considered a conservative, acceptable surrogate criterion to determine safety margins of reactor operation [19].

Under normal operating conditions, continuous heat transfer from the fuel to the coolant would prevent heat buildup within the fuel bundle. However, as plant operators want to run the reactor with a higher power yield, boiling may occur which invariably leads to conditions under which dry-out could occur. While the limit in conductivity of the nuclear fuel would restrict the increase in fuel sheath temperature, it is arguable whether there would be sufficient time to shut the reactor down if fuel integrity was jeopardized.

Consequently, trip parameters are required to measure and monitor the values of important plant parameters such as pressure, temperature, neutron flux, etc.

The trip parameters that the CNSC encourages licensees to account for in their safety analyses include the following:

1. The predefined trip parameter limit on the shutdown systems should be selected such that the onset of intermittent fuel sheath dry-out is prevented; and
2. The backup trip parameters predefined limit on the shutdown system should be selected such that:
 - a) fuel sheath temperature does not exceed 873 K; and
 - b) duration of post-dry-out heat transfer operation does not exceed 60 seconds [19].

3.3 Deformation Mechanisms

There are a number of mechanisms that contribute strains to the material. The total strain in the Zircaloy-4 sheath is the sum of strains caused by elastic behaviour, plastic behaviour, thermal expansion, and creep.

3.3.1 Elastic Deformation

Elastic deformation occurs when a material recovers its original shape when the applied load is removed [20]. The material can recover its original shape because the magnitude of the applied load was less than the yield stress of the material. The yield stress of a material is dependent on a number of factors such as temperature, manufacturing process and microstructure.

The relation between stress and strain of the material determines the response of an assembly to applied forces. For linearly elastic materials, the relation is related by the following equation:

$$\sigma = E \varepsilon_{el} \quad (3.1)$$

where σ is stress, E is the proportionality constant known as Young's Modulus and ε_{el} is elastic strain.

This relationship can be generalized to three directions by separating the stress and strain components by the three dimensions and adding the shear stresses, τ , and shear strains, γ [21]. Written in matrix notation, the stress-strain relationship is:

$$\begin{bmatrix} \varepsilon_x \\ \varepsilon_y \\ \varepsilon_z \\ \gamma_x \\ \gamma_y \\ \gamma_z \end{bmatrix}_{el} = \begin{bmatrix} 1/E_x & -\nu_{yx}/E_y - \nu_{zx}/E_z & 0 & 0 & 0 \\ -\nu_{xy}/E_x & 1/E_y & -\nu_{zy}/E_z & 0 & 0 & 0 \\ -\nu_{xz}/E_x - \nu_{yz}/E_y & 1/E_z & 0 & 0 & 0 & 0 \\ 0 & 0 & 0 & 1/G_{xy} & 0 & 0 \\ 0 & 0 & 0 & 0 & 1/G_{xz} & 0 \\ 0 & 0 & 0 & 0 & 0 & 1/G_{xz} \end{bmatrix} \begin{bmatrix} \sigma_x \\ \sigma_y \\ \sigma_z \\ \tau_{xy} \\ \tau_{xz} \\ \tau_{yz} \end{bmatrix} \quad (3.2)$$

where G is the shear modulus and ν is Poisson's ratio.

For isotropic materials, the shear modulus is related to the Young's Modulus and Poisson's ratio by the following equation [20]:

$$G = \frac{E}{2(1 + \nu)} \quad (3.3)$$

The set of equations described in 3.2 allow for different elastic properties in each of the directions. Having different material properties in different directions is termed anisotropy. The Young's modulus of the fuel sheath is anisotropic. However, at the temperatures of interest in off-normal conditions, the deformation resulting from the elastic strain is much smaller compared to the deformation resulting from plastic and thermal

strain components. As a result, the anisotropy of the elastic strain was omitted for the simulations in this thesis.

3.3.2 Plastic Deformation

Plasticity describes the response of a material beyond its yield strength. Plastic deformation occurs as a result of dislocation motion between planes of atoms due to shear stresses; this motion is essentially a rearrangement of atoms in the crystal structure [22]. After the loads are removed, the resulting deformation is permanent because the magnitude of the applied load exceeds the yield strength of the material. Like elasticity, plasticity defines time-independent mechanical responses to loading.

The relation between increments of stress and strain of the material is determined by the following components in ANSYS: yield criterion, and hardening rule [23].

3.3.2.1 Yield Criterion

A one-dimensional stress-strain curve is typically used to represent the data obtained from a uniaxial tensile test. In 3-D cases, the structures exhibit multiaxial stress states. For these cases, the yield criterion is used to provide a scalar measure of the multiaxial stress state in order to compare it with the uniaxial case [23]. ANSYS uses the von Mises criterion as the yield criterion. The von Mises criterion predicts that a stress state reaches yield state when the distortional energy of a volume equals the distortional energy of the same volume when loaded uni-axially to the yield strength [24]. The von Mises equivalent stress, σ_e , is given by the following equation:

$$\sigma_e = \sqrt{\frac{1}{2}[(\sigma_1 - \sigma_2)^2 + (\sigma_2 - \sigma_3)^2 + (\sigma_3 - \sigma_1)^2]} \quad (3.4)$$

where σ_1 , σ_2 and σ_3 are principal stresses.

Yielding occurs when the von Mises equivalent stress exceeds the yield strength of the uniaxial material. When plotted in the 3-D σ_1 - σ_2 - σ_3 space, the von Mises yield surface is a cylinder aligned with the σ_1 , σ_2 and σ_3 axis as illustrated in Figure 5 below.

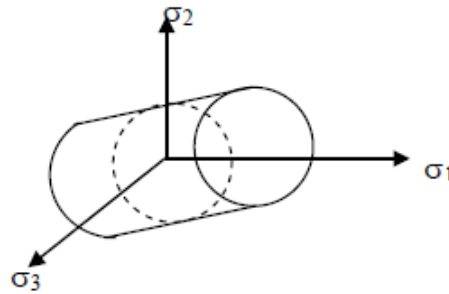


Figure 5: Von-Mises yield surface in the 3-D σ_1 - σ_2 - σ_3 space. Reproduced with permission from [21].

A stress state on the surface of the cylinder indicates that yielding will occur. No stress state can exist outside of the yield surface of the cylinder because the radius or the location of the yield surface will change [23]. The rule that defines how the yield surface changes with respect to yielding is called the hardening rule.

3.3.2.2 Hardening Rule

The hardening rule describes the changes in the yield surface as the material hardens due to plastic deformation. There are two basic hardening rules implemented in ANSYS: (a) kinematic hardening, and (b) isotropic hardening [23].

Kinematic hardening assumes that the yield surface remains constant in size but shifts in the direction of yielding. The stress-strain behaviour for kinematic hardening is illustrated in Figure 6.

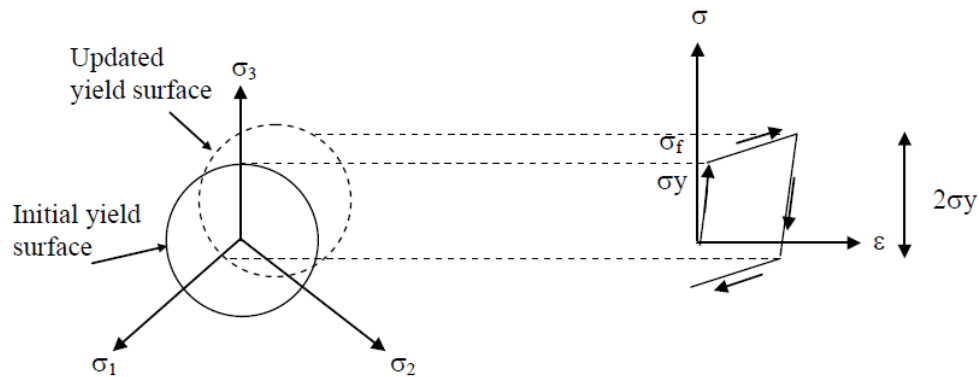


Figure 6: Behaviour of the kinematic hardening model. Image courtesy of [21].

The kinematic hardening model accounts for the Bauschinger effect. The effect refers to the material property wherein an increase in tensile yield strength correlates to a decrease in compressive yield strength such that a $2\sigma_y$ difference between the yield strengths is maintained [24].

In contrast to the kinematic hardening model, isotropic hardening assumes that the yield surface expands uniformly in all directions with plastic flow but preserves the original axis of the surface as illustrated in Figure 7.

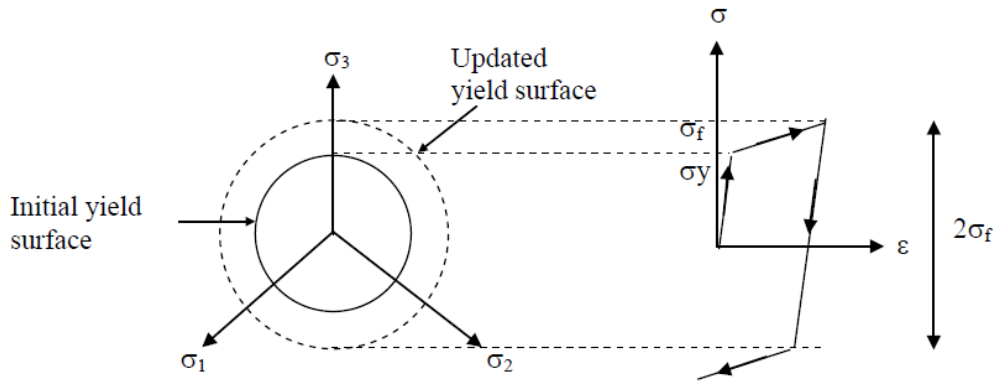


Figure 7: Behaviour of the isotropic hardening model. Image courtesy of [21].

The isotropic hardening model postulates that under uniaxial loading conditions, even when the yielding takes place only in tension, the yield stress in compression also increases in magnitude [21]. This indicates that if an object is loaded in tension past yield, then unloaded and reloaded in compression, it will compress elastically until the maximum tensile flow stress past yield is achieved and then the specimen yields at $2\sigma'$ in compression.

3.3.3 Thermal Expansion

When a material is heated or cooled, the material experiences a change in length by an amount proportional to its original length and the change in temperature [20]. The proportionality constant is a material property termed the coefficient of thermal expansion.

The coefficient of linear thermal expansion of a material can be expressed as:

$$\alpha = \frac{1}{L} \left(\frac{\partial L}{\partial T} \right) \quad (3.5)$$

where α is the linear thermal expansion coefficient, L is the length of the specimen. The thermal strain, ε_{th} , caused by the thermal expansion can be calculated by re-writing Equation 3.5 as follows:

$$\varepsilon_{th} = \alpha(T - T_{ref}) \quad (3.6)$$

where T is the temperature and T_{ref} is the reference temperature corresponding to zero thermal strain. The material model for the thermal expansion of Zircaloy-4 is detailed in Section 5.3.1.5.

3.3.4 Creep

Creep is a time-dependent plastic deformation that occurs due to microstructural changes at high temperatures and at stress levels below the yield strength of the material [25]. Temperature has a significant impact on creep deformation since changes in anisotropy, grain size, and phase transformation ($\alpha \rightarrow \beta$) are accelerated at higher temperatures [26]. Due to this temperature dependence, models describing creep strain rate are divided into low temperature creep models for normal operating conditions (NOC) and high temperature creep models for operating temperatures above 700 K [27].

The microstructural creep model developed by Sills and Holt [28] was used to describe the high-temperature creep behaviour of the sheath in this work. The model is applicable between 700 K and 1600 K. It describes total creep rate as the sum of three components: diffusional creep, dislocation creep and transition creep. The domains where each creep component is dominant are illustrated in Figure 8 below.

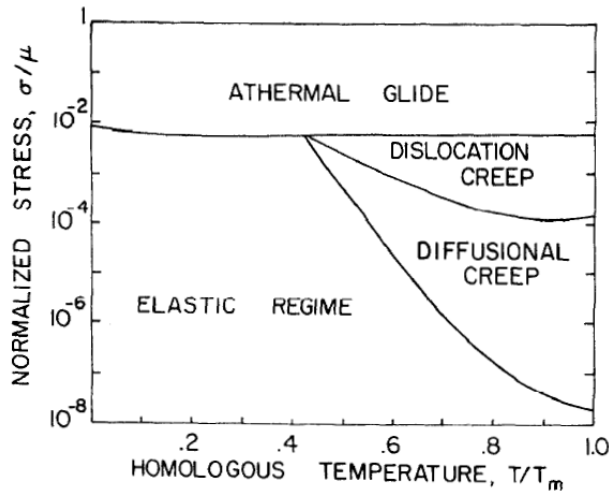


Figure 8: Deformation graph showing the stress and temperature domains where different creep mechanisms are most likely to occur. μ is the shear modulus and T_m is melting temperature of Zircaloy. Image courtesy of [28].

Assessing the temperature and stress observed in the experimental study, it was decided to limit the creep mechanism in this study to diffusional creep as that would be the dominant creep deformation mechanism for the conditions of interest. This simplification is justified as diffusional creep is more sensitive to high temperatures than other creep mechanisms. Solid-state diffusion is heightened at high temperatures because the activation energy needed to overcome the energy barriers to atomic displacements is provided by thermal energy [30].

Diffusional creep refers to creep that occurs due to grain boundary sliding, $\dot{\epsilon}_{gb}$. Boundaries between crystals are weakly bonded. When a load is applied, these boundaries can slide past each other [28]. The resulting deformation is called diffusional creep. [26].

3.4 Fuel Element Bowing

The bowing of a fuel bundle is described as the lateral deflection of an element from the centreline of the axis. These deflections are generated due to bending moments caused by a non-uniform temperature distribution both within the sheath and between the fuel and the sheath [9]. As the temperature gradient along the length of and across the fuel element increases, the element bows in the direction of the hotter side to compensate for the shift in axial strain. The temperature asymmetries in the sheath are caused due to a combination of the effects of (i) non-uniform coolant temperature in the vicinity of the elements due to unsatisfactory mixing, (ii) non-uniform heat transfer between the coolant and sheath due to changes in sub-channel geometry, (iii) non-uniform heat transfer between the fuel and the fuel sheath and (iv) disproportionate heat generation caused by neutron flux gradients along a fuel element [11].

Under NOC, thermal gradients may exist between the fuel pellet and the fuel sheath due to the power gradients that arise from varying neutron flux gradients along the element. If the fuel sheath is stressed and crept as a result of this gradient, the permanent strain causes a small bow in the material [9]. Under accident conditions, thermal gradients in the radial and axial direction of fuel element become large as the temperature of the regions where local dry-out occurs is greater than the temperature of the sheath that remains wetted by the coolant [14]. As such, the extent of bowing is greater than under NOC. Moreover, as the plasticity of the sheath is increased, there is a greater potential for permanent bowing, depending on the duration of the transients.

The consequence of fuel element bowing is reducing the gap between adjacent fuel elements. The gap where the coolant passes through the fuel bundle to transfer the heat generated from fission is defined as a sub-channel [11]. As the sub-channel area decreases, local coolant starvation occurs because the coolant flow is re-distributed. This leads to further element deformation due to localized overheating of the fuel, increasing the probability of fuel deformation. The positive feedback loop jeopardizes the integrity of the fuel and of the surrounding components as it can lower the critical heat flux value which determines where dry-out will occur. As a result, the trip parameter no longer applies and the safety margin decreases.

3.5 Sheath Oxidation

Since the average sheath temperature is approximately 613 K at NOC, the oxidation of the Zircaloy sheathing is not a significant concern at these relatively low temperatures. However, at higher sheath temperatures reached during transient conditions, the reaction between the Zircaloy sheath and the heavy water coolant becomes an important consideration. The chemical reaction is given by the following formula [27]:



The interaction between the heavy water vapour and the Zircaloy sheath results in the formation of an oxide layer. The oxide layer will crack if it is subjected to a sufficient amount of stress. The cracking increases localized deformation and compromises the integrity of the fuel sheath. The oxide layer also impacts the ability of the coolant to remove heat from the fuel by increasing the thermal resistance of the fuel sheath to the coolant

[31]. Fuel coolability is further exacerbated as the reaction is exothermic and releases 586 kJ mol⁻¹ of energy, which heats the fuel and the fuel sheath [32]. Severe sheath oxidation can cause failure of the fuel sheath due to embrittlement. The material strength and ductility of the Zircaloy sheath is also affected because the deuterium diffuses into the Zircaloy sheath [33]. Sheath oxidation was not considered in the model because oxidation was not seen on the bundle after the experiment.

3.6 Pressure Tube Creep and Growth

As components are aged during their operating life, there are certain physical effects that are induced on the nuclear system components. These physical effects are termed the aging phenomena and generally have a negative impact on the normal operating conditions of a reactor as they affect the safety margins of the plant. The aging mechanism relevant to modeling the deformation of a CANDU fuel bundle includes the ageing of pressure tubes. The primary function of the pressure tube is to support the fuel bundle in the reactor vessel and to allow the pressurized coolant to remove the heat generated from fission. As such, the pressure tubes must be resistant to corrosion, as well as to creep and growth. However, over plant life, the pressure tube undergoes axial deformation, diametric creep and sagging [34].

Axial elongation of pressure tubes results from thermal expansion and longitudinal creep. As the pressure tube operates at elevated temperatures for an extended period of time in high neutron fluxes, the crystal structure of the metal expands under thermal stress. This allows the lattice defects which are created by fast neutron damage to move about the lattice more easily, increasing the probability of deformation by creep. Given that PT axial

elongation is proportional to the flux distribution of the fuel channel, the elongation in the outer region is less than that in the inner region within a core [35].

Due to the constant force of gravity, high reactor operating temperatures and the effects of irradiation by neutron flux, the diameter of the PT begins to creep over time. The increase in local PT diameter reduces the hydraulic resistance in the channel and increases its coolant flow [10]. However, the flow is redistributed within the bundle such that there is less flow between the sub-channels as the increased flow tends to by-pass over the fuel bundle. Reduced flow in the sub-channels affects the rate at which heat is removed from the fuel. By allowing sub-cooled boiling to occur, it decreases the critical heat flux. Thus, the calculated trip set-points for dry-out may no longer be valid and the margin of safety decreases.

During the service time of a reactor, the PT may also sag under the weight of the fuel bundle and coolant contained within it. The sag occurs between the garter springs that separate the PT from the surrounding calandria tube [35]. This mechanism is illustrated in Figure 9.

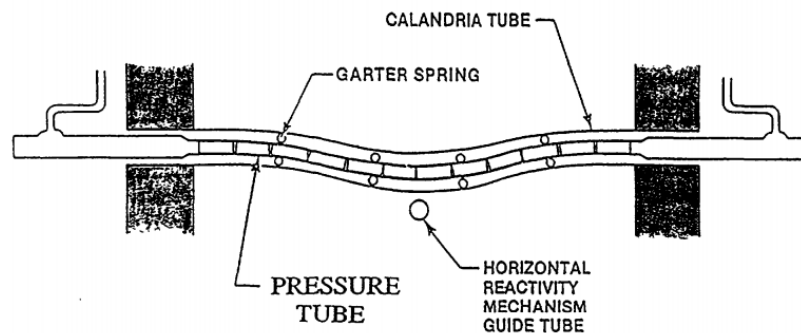


Figure 9: Pressure Tube Sag. Image courtesy of [35].

The creep and sag of the PT was not considered in the model because it was represented by a fused quartz tube in the experiment, instead of the Zircaloy-2 used in CANDU reactors. To maintain consistency with the experiment, the PT was modeled as a non-deforming boundary condition.

4 State of Art

Since the inception of the nuclear power industry, various independent fuel models have been developed for a variety of reasons. These models can be split into two major categories: fuel performance models and fuel element and bundle deformation models. Fuel performance models such as ELESTRES [36] or ELOCA [37] define fuel behaviour under normal operating conditions and transient conditions. The limitations of these models lie in the fact that they are essentially two-dimensional with no capability in predicting the deformation of fuel elements during transient conditions [38]. Fuel element and bundle deformation models determine the extent of thermo-mechanical deformation of the elements in a fuel bundle due to physical phenomena such as bowing, sagging, and creep. A number of the deformation models are discussed in Section 4.1 and 4.2. The listing is not comprehensive; the models discussed were selected for their relevance to this work.

4.1 Industry Standard Toolset

The industry standard toolset (IST) for fuel element and bundle bowing is aptly named the BOW code and was developed by AECL Sheridan Park (now SNC-CANDU Energy) [39]. The code represents the fuel elements as one-dimensional composite beam that can deform in 3-D space to simplify fuel element geometry. The code employs two user-defined inputs to compensate for the simplified geometry. The first input parameter is the Curvature Transfer Factor (CTF), which describes the extent to which a fuel pellet induces local curvature on the sheath. The value of the CTF varies between zero, which corresponds to the local curvature not being induced on the sheath, and one, which

corresponds to the full curvature being imposed on the sheath. The second input parameter is the Rigidity Enhancement Factor (REF), which defines the ability of the pellet to provide resistance to the bending moment. The value of the REF varies between zero, corresponding to no resistance being provided by the pellets, and one, corresponding to complete resistance of the bending moment by the pellets and sheath [39]. While these two parameters can be retro-fitted to match existing experiments, the BOW code is not qualified to predict element behaviour in transient scenarios. Therefore, it is necessary to have a 3-D contact model between the pellets and the sheath.

Despite its limitations, the BOW code considers a number of different physical phenomena including circumferential and axial deflections due to temperature variations in the fuel pellet and sheath, neutron flux gradients, pellet cracking, gripping and slipping between the pellet and sheath, hydraulic drag force, and sheath creep. The code uses the finite element method to numerically solve the governing equations that are based on the fundamental principles of solid mechanics. Additionally, the code has been verified against analytical solutions and benchmarked against post-irradiation examinations to demonstrate its precision and accuracy in modeling fuel behaviour deformation behaviour under NOC [39].

4.2 Multiphysics Models

To model real life experiments accurately, it is necessary to account for the multiple simultaneous physical phenomena interacting within the system. With multidimensional and multiphysics commercial software such as ABAQUS, ANSYS, COMSOL, and MOOSE being readily available, it has become easier to better represent coupled

phenomena such as solid mechanics, heat transfer, and fluid dynamics. The advantage of the multiphysics approach is that it requires fewer simplifications of the boundary conditions to solve the governing equations, providing more realistic results for nuclear applications. The suitability of these commercial software programs in modeling the deformation of fuel elements and the fuel bundle has been assessed below.

Using the finite element software ABAQUS, McCluskey [15] developed a 3-D model to predict the thermomechanical behaviour of a fuel element. The model accounts for the contact interaction between the fuel pellet and sheath and between the fuel pellets by coupling the heat transfer mechanism of both the fuel pellets and sheath with their mechanical behaviour. The model seeks to describe the structural deformation of a fuel element during in-reactor operation with the linear power varied from 20-30 kW m⁻¹. The model is limited in that it does not account for sheath creep and assumes symmetry along the axial direction due to memory restrictions. Despite these limitations, the model was compared against the ELESTRES fuel performance code by using performance parameters such as sheath temperatures and gap sizes between the fuel and the sheath. Furthermore, the model was successfully benchmarked against analytical calculations by comparing the resulting deflection with the deflection under simple beam loading conditions [15].

The deformation of a 3-D fuel element has also been modeled by Williams using ANSYS [40]. Given its robust ability to couple thermo-mechanical behaviour and solving contact interaction, ANSYS is an ideal platform to assess the thermal deformation behaviour of fuel elements. The objective of the model developed by Williams was to predict fuel element deformation behaviour due to temperature gradients under transient

conditions including LB-LOCA scenarios. Two planes of symmetry are used to model the full 31-pellet fuel element. Williams' model illustrates the mechanical and thermal contacts between individual pellets and between the pellet and the surface of the fuel sheath. The material properties of the fuel and sheath used in the model are temperature-dependent and are consistent with values used for the fuel performance codes ELESTRES and ELOCA. The model accounts for transient conditions by including time-dependent physical phenomena such as creep, volumetric heat generation, pellet-sheath gap heat transfer, and internal gas pressure. The model was compared against out-of-reactor experiments with excellent agreement and has the ability to predict fuel bowing and sagging under NOC and transient conditions. However, as with any other computer code, the model has limitations. The model experiences difficulties in obtaining a numerically converged solution owing to abrupt changes in contact definition between the pellets and fuel sheath during transient conditions. Modeling sheath detachment from the pellet during cooling cycles leads to rigid body motion of the pellets, which is difficult to resolve numerically. Furthermore, parameters such as coefficient of friction and initial pellet spacing must be defined to run the model; however, they are difficult to predict and require parametric studies to ensure that the initial parameters are not adversely affecting the results obtained from the model [40].

Another ANSYS model analyzing fuel element behaviour under post-dry-out conditions was developed by Krasnaj [16]. The primary objective of the work was to create a fuel element deformation model that could mimic deformation induced from non-uniform heat transfer caused by dry-out. The model geometry includes a solid outer fuel

element, in frictionless contact with a portion of the pressure tube. It used two different models, Individual Fuel Pellet Model and Cracked-Fuel Stack Model, and defined contact between the pellets and the sheath. The results from the model were compared against the analytical beam model postulated by Suk et al [41] and it was observed that the model overestimated the degree of deformation. Despite this overestimation, imposed drypatch thermal gradients of 873 K, corresponding to maximum sheath temperature of 1073K, did not lead to contact between the fuel element and pressure tube. Additional convective heat transfer conditions were added to generate an adequate thermal load to initiate contact between the fuel element and pressure tube. The model provides insight into the uncertainties associated in investigating contact between the fuel element and pressure tube under transient conditions and could be used to investigate relaxing the trip parameters specified by the CNSC [16].

In contrast to the solid element approach implemented in the ANSYS models, a CANDU bundle deformation model using beam element representation was developed by Bell [12] with COMSOL Multiphysics software. The model pairs the two-dimensional heat conduction analysis with the beam element approach of solid mechanics across a cross section of the fuel element. The fuel elements, including the fuel pellets and the sheath, were represented by beam elements. While the beam elements can deform in three spatial dimensions, they are fundamentally one-dimensional in nature. Despite their one-dimensionality, the elements provide a boundary condition for the fuel element by supposing that the endcaps are welded onto the end plates. The model includes physical phenomena such temperature dependent material properties of the fuel pellets and the

sheath, fuel burn up and heat generation accounting for radial flux depression. A ‘gripping factor’ is required to transfer the bending moment of the fuel pellets onto the sheath. This accounts for fuel pellet-sheath interaction, without explicitly including contact between the fuel pellets and sheath. It is also limited in that it does not include contact between the individual fuel pellets. The bundle deformation model was validated against the BOW code and an out-of-reactor bundle deformation experiment with satisfactory results and concluded that COMSOL was able to satisfactorily illustrate the deformation behaviour of the fuel and sheath [12].

The Multiphysics Object Oriented Simulation Environment (MOOSE) framework [42], created at the Idaho National Laboratory, was used to generate a 3-D fuel element deformation model by Gamble [43]. Unlike other platforms discussed above, MOOSE is mathematical software that is the foundation of the LWR nuclear fuel performance code BISON. To assess the deformation mechanism of CANDU fuel, an independent fuel performance code named Horizontal Nuclear Fuel Simulation Environment (HORSE) was created. The model geometry utilizes two planes of symmetry to generate the fuel element and accounts for temperature dependent properties of the fuel and sheath, fuel swelling, sheath creep, fuel pellet-to-fuel pellet and fuel pellet to sheath contact. The dimensionality effects on contact algorithms were also examined by conducting a two-dimensional and a 3-D contact analysis.

The converged results indicated that for frictional contact between the pellet and the sheath, the extent of penetration exceeded acceptable parameters, indicating that the contact stiffness of the frictional model needed to be modified such that the resulting

penetration is negligibly small. In addition to frictional contact, glued contact was also studied. Glued contact in MOOSE allows two bodies to come into contact and henceforth, stay in contact. While this algorithm is numerically robust, it does not allow the sliding between surfaces which leads to an overestimation of the contact pressure between the fuel pellet and sheath at higher burnup conditions. The overestimation of contact pressure results in the underestimation of deflection at higher linear power. Furthermore, analyzing the maximum deflection due to thermal bowing of a fuel element with individual pellets produced anomalous results. Due to the limitation of the framework, the glued contact algorithm was used to restrict the degree of lateral deflection resulting from external thermo-mechanical loading. In spite of the difficulties observed in modeling the deformation of the fuel element, the contact algorithms for isolated contact analyses were validated against ELESTRES and analytical solutions with acceptable results. It was concluded that further testing is required if MOOSE is to be used for CANDU fuel bowing analysis [43].

The models discussed above used a number of unique platforms that employ the finite element method to model the deformation of a fuel element. The variation between the models in a number of aspects such as element types, contact algorithms, physical phenomena modeled, and reactor conditions offers invaluable insight in the modeling of CANDU fuel deformation and is summarized in Table 1.

Table 1: Comparison of Industry and Multiphysics Nuclear Fuel and Bundle Deformation Models.

CODE	ELEMENT TYPE AND DIMENSION	MODELING CAPABILITIES	SOFTWARE	LIMITATIONS
BOW	Beam; 1D	Element	FORTRAN	Requires user defined values of CTF and REF.
McCluskey	Solid; 3D	Partial Element	ABAQUS	Does not account for sheath creep; Assumes symmetry along the axial direction.
Krasnaj	Solid; 3D	Element	ANSYS	Overestimates extent of deformation.
Williams	Solid; 3D	Element	ANSYS	Computationally-intensive and some difficulties achieving convergence associated with the contact modeling
Bell	Beam; 1D	Bundle	COMSOL	Requires user-defined ‘gripping factor’; does not explicitly include pellet-sheath interaction.
Gamble	Solid; 3D	Element	MOOSE	Difficulties were identified with the contact model leading to under estimation of deformation. Forced to use bonded contact to achieve convergence.

Comparing the models, it was noted that the limitations of beam element approach in modeling the radial deflections were improved by transitioning to a solid element approach. Prior research conducted in the field sets the stage for developing a 3-D fuel bundle deformation model. From the varying models, it was observed that while contact between the fuel pellets and the element and between adjacent elements is necessary, it is a complicating factor that is difficult to simulate correctly.

5 Model Development

To simulate the deformation of a bundle under high temperature conditions, a number of phenomena need to be simulated: sag of the elements and the end-plates, differential thermal expansion of the fuel elements, fuel element bowing, and creep deformation of the bundle. The finite element method was selected to model these phenomena because it is capable of considering the mechanisms of bundle deformation including temperature dependent material properties, interaction between adjacent elements in a bundle and lateral deformation of the bundle under different loads. Since the results from an in-laboratory experiment conducted to investigate bundle deformation behaviour were made available for simulation purposes for the very first time, the loading and boundary conditions from the experiment were applied to the simulation. Maintaining consistency with the experiment ensured that the simulation results could be verified against experimental results. This chapter summarizes the methodology used for the development of the fuel bundle deformation model. It details the thermal loading and boundary conditions, which were applied to the simulation, and defines the material properties used to solve for the deformation of the fuel bundle.

5.1 Finite Element Method

In general, engineering problems can be defined as mathematical models with differential equations and a corresponding set of initial and boundary conditions. Derived from the application of fundamental laws and principles to a system, these governing differential equations are solved to provide detailed behaviour of a system under the given conditions. However, an analytical solution is not always plausible because of the

complexities that arise in practical engineering problems such as complex restraints or complex loading. In such cases, the solution is found by numerical approximation methods such as the finite difference method and the finite element method. While the finite difference method replaces the derivatives by difference equations to produce a set of linear equations, the finite element method uses integral formulations to create a system of algebraic equations [44]. This distinction makes the finite element method a better candidate to approximate numerical solutions for problems with complex geometry, complex boundary conditions and non-isotropic materials.

The finite element method is a numerical technique used to solve boundary value equations by using the concept of piecewise polynomial interpolation. The complex geometry of the overall system is divided into several finite elements with simple geometry and the response to the model is determined by connecting all elements together. The finite elements selected for the mathematical model can be multi-dimensional ranging from one-dimensional bars and beams, two-dimensional shells to three-dimensional hexahedrals and tetrahedrals or any combination thereof [21]. The choice of finite element determines the translational and/or rotational degrees of freedom at nodal points that must be solved to approximate a solution to the boundary value problem. Beam and shell elements have translational and rotational degrees of freedom whereas bars and solids such as hexahedrals have only translational degrees of freedom. The field variable (i.e., temperature and displacement in this case) is solved at the nodes and is interpolated in between the nodes by polynomial functions called shape functions, which are dependent on the type of element used.

In addition to choice of element type, a number of simplifying assumptions need to be made in order to approximate the solution with the FEM. Loading and boundary conditions must be applied to ensure the system imitates the physical model and that rigid body motion does not occur. Rigid body motion describes the idealization wherein the deformation between two given nodes of the body remains the same, regardless of the external loading conditions applied. The model will solve if the individual elements undergoing rigid body motion are attached to others that are constrained. However, if the entire structure is undergoing rigid body motion, the model will not solve because a sufficient amount of boundary conditions have not been applied and the structure is free to move. This indicates that a good understanding of the type of behaviour expected under the applied loading and boundary conditions specified are required to produce an eminent and accurate solution [21].

Since assumptions and simplifications must be made for finite element analysis (FEA), the model will never be exact. FEA will provide an approximation to the solution. The error associated with the finite number of elements and degrees of freedom is termed the discretization error. Increasing the number of finite elements in the mesh can increase the accuracy of the model. Since additional nodes are added to the geometry from which data can be extracted, the increase in the number of elements is proportional to the model's ability to converge towards the solution of the system. The drawback is that the addition of elements requires increased computational time. Convergence studies are conducted for the optimization of the mesh size such that the proper solution is obtained in a reasonable amount of time.

Of the number of different commercial FEA software platforms that exist, ANSYS was chosen to model fuel bundle deformation behaviour for its multiphysics simulation capabilities. Unlike COMSOL, which has the ability to specify custom partial differential equations for modeling systems, ANSYS provides more robust contact algorithms, which are of greater relevance to this work. The software has the ability to couple multiple physics phenomena such as solid mechanics, fluid dynamics, and heat transfer using the FEM to describe the mathematical models [45]. This multiphysics coupling ability is particularly advantageous as the results from the thermal analysis can be used as input for the structural analysis and the deformation resulting from the thermal load can be calculated.

5.1.1 Nonlinear Simulations

In linear simulations, the deformation of the system and the applied loading are proportional. The relationship can be expressed as

$$\{F\} = [K]\{U\} \quad (5.1)$$

where the vector $\{F\}$ represents the external forces acting on the nodes, vector $\{U\}$ represents the nodal displacements and $[K]$ is the stiffness matrix based on material properties and geometry.

In nonlinear simulations, the stiffness matrix is no longer a constant matrix; it becomes a function of $\{u\}$ as the stiffness matrix changes as load is applied. Equation 5.1 can be rewritten as:

$$\{F\} = [K(U)]\{U\} \quad (5.2)$$

Solving the above equation poses challenges in nonlinear simulations, as the nodal displacement cannot be solved directly because the information needed to create the

stiffness matrix is not known. Moreover, the applied loads can also be a function of the deformation in cases including contact. Structural nonlinearities can be divided into three categories: geometric nonlinearity, material nonlinearity and contact.

In geometrically linear problems, the stiffness matrix is written before deformation occurs and does not account for deviation from the original geometry. The deformations are so small in magnitude that the change in geometry can be ignored. However, in cases of large deformation or displacement, the deviation from the original geometry cannot be ignored. When the deformation or displacements are sufficiently large that the equilibrium equations must be written in terms of the current deformed geometry of the structure, geometric nonlinearities develop.

Material nonlinearity occurs when the material's stress-strain relation is not linear or when the material properties are functions of other variables. The stress-strain properties of nonlinear materials are influenced by a number of factors such as environmental conditions, load history, and the amount of time that a load is applied. Material nonlinearities include material models with plasticity, hyper-elasticity, viscoelasticity, and creep.

Contact nonlinearity refers to a change in the topology of the structure which leads to an abrupt change in the stiffness matrix. Potential topology changes include the changes in contact status of adjacent objects and the failure of the structural material.

5.1.2 Contact Algorithms

A major motivation for selecting the finite element method was to utilize its ability to handle complex restraints such as contact to develop a 3-D computational model, intended

to simulate the deformation of an empty fuel bundle under off normal and accident conditions. A 3-D deformation model of the empty fuel bundle will set the basis for the future development of a full bundle model that will include the fuel pellets and sheath as distinct components. This approach seeks to counter the limitations posed by the beam approach by allowing the fuel pellet-to-fuel sheath and fuel element-to-fuel element interaction to be simulated directly. Given that the bundle deformation model will include frictional contact between fuel elements and between fuel elements and the pressure tube, the contact formulation used will be briefly discussed.

In ANSYS, two distinct surfaces are said to be in contact when they are mutually tangent. Surfaces in contact can transmit compressive normal forces and tangential frictional forces. When surfaces are able to move towards or away from one another, they are said to have changing-status nonlinearity because the stiffness of the system depends on whether the parts are touching or separated. The most important characteristic of surfaces in contact is that they do not interpenetrate as illustrated in Figure 10.

While physical contacting bodies do not interpenetrate because their surfaces are continuous, surfaces in the finite element method are not continuous because they are represented by a finite number of discrete nodes. Therefore, ANSYS must establish a relationship between the two interacting surfaces to prevent interpenetration and enforce contact compatibility.

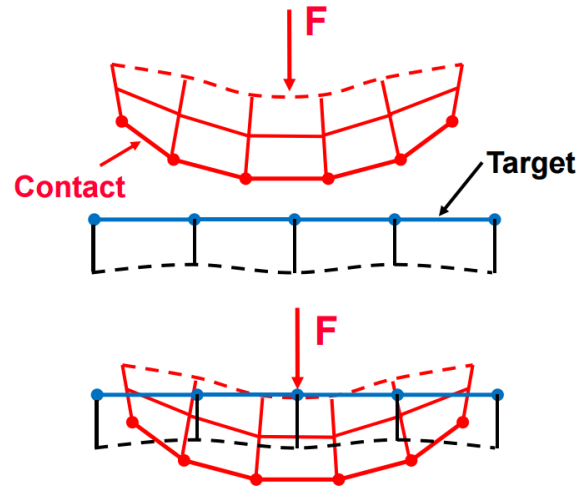


Figure 10: Interpenetration of the contact and target surfaces when no contact compatibility is specified. Image courtesy of ANSYS, Inc. [46].

The relationship is established using one of the several contact algorithms available in ANSYS Workbench. Of particular interest to this work are the penalty-based contact algorithms because they are recommended for general frictional contact problems: the penalty method and the Augmented Lagrange method.

The penalty method uses a simulated “spring” to generate stiffness between two contacting surfaces. The spring begins to simulate the surfaces resisting penetration once they begin to penetrate each other. A contact force is applied by the springs at the detection points which have penetrated the surface with the intent of reducing the amount of penetration to zero. The force at the contact detection points is calculated using:

$$F_{contact} = k_{normal}x_p \quad (5.3)$$

where k_{normal} is the contact stiffness and x_p is the penetration depth between the two surfaces as illustrated in Figure 11.

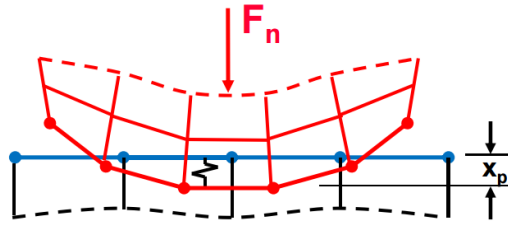


Figure 11: Schematic illustrating the penalty method. Image courtesy of Ansys, Inc.[46].

In an ideal situation, infinite contact stiffness would result in zero penetration; however, this is not numerically stable as the contact surface would be completely removed from the target surface and lead to non-convergence. There must be a finite amount of penetration in order for the contact force to be generated. The contact force needs to be large enough to push the contact surface back to the target surface and resist penetration; however, the contact force cannot be so large that the two surfaces are no longer mutually tangent. The challenging aspect here is that the magnitude of the contact force required to resist penetration is unknown beforehand; this necessitates an iterative solution until there is no significant change in the contact pressure.

In order to reduce the sensitivity to the magnitude of the contact stiffness, an internally calculated term, λ , can be added to equation 5.3 to augment the contact force calculation:

$$F_{contact} = k_{normal}x_p + \lambda \quad (5.4)$$

This method is termed the Augmented Lagrange method. Although the Augmented Lagrange method may require more iterations to achieve convergence, it should produce less penetration than the penalty method. Therefore, this method was chosen to define frictional contact between the fuel elements and between the outer fuel elements and the pressure tube in this model.

5.1.3 Newton-Raphson Method

When nonlinear behaviour is present in engineering problems, the displacement response cannot be calculated directly with a set of equations. An iterative process is required to approximate the solution to the problem. The Newton-Raphson Method is one such method that solves for the displacement vector and the associated stiffness matrix that makes the entire structure in equilibrium for the load applied. The method divides the applied load into a series of increments, which are applied over a number of specified sub-steps. The equations used in the Newton-Raphson method can be expressed as

$$\{F^a\} - \{F_i^{nr}\} = [K_i^T(U)]\{\Delta U_i\} \quad (5.5)$$

$$\{U_{i+1}\} = \{U_i\} + \{\Delta U_i\} \quad (5.6)$$

where $[K_i^T]$ is the Jacobian matrix (tangent stiffness matrix), $\{F^a\}$ is the vector of incremental applied loads, $\{F_i^{nr}\}$ is the restoring force vector calculated from the element stresses, and $\{\Delta U_i\}$ is unknown incremental field quantity vector.

An initial guess of the solution vector U_0 is used for the first time step to begin the iterative process. The updated tangent stiffness matrix is computed. The full load, F^a , is applied and a linear approximation is made to calculate the displacement using the initial stiffness matrix.

$$\Delta U_1 = \frac{F^a}{[K_0^T(U_0)]} \quad (5.7)$$

The stiffness K_1^T is recalculated based on the resulting displacement and the equilibrium force, F_1 , is determined with the updated stiffness matrix.

$$F_1 = K_1^T(U_1)(U_1) \quad (5.8)$$

The difference between the forces F^a and F_1 is termed the residual force. This residual force vector provides insight into the suitability of the load step taken towards the exact solution. The residual force is evaluated for convergence against a specified tolerance to determine if further equations are needed. If the convergence criterion is not met, the iterative process continues with the new load increment given by the residual force.

$$\Delta F = F^a - F_1 \quad (5.9)$$

Using the current tangent stiffness K_1^T , the new displacement U_2 is computed. The stiffness is then recalculated based on U_2 and the equilibrium force F_2 is calculated. The iterative process continues until $F^a = F_1$ within a specified tolerance.

5.2 Fuel Bundle Heat-Up Experiment

High temperature tests were performed by personnel at CNL on an empty 37-element fuel bundle in the Bundle Behaviour Test Apparatus to investigate the deformation of an empty CANDU bundle subject to temperature conditions related to post-dry-out and the onset of LB-LOCA. The major motivation behind examining the behaviour of a bundle without fuel pellets was to improve the understanding of the deformation mechanisms and interactions within bundle components. The bundle-heat up experiment was used to support the development of the 3-D fuel bundle model presented in this work and to validate whether the material properties and deformation behaviour are being modeled correctly. This experiment marks the first time that this set of data was made available for simulation purposes.

The test apparatus included a heated chamber composed of a fused quartz tube, which allowed optical views along the top, bottom and sides of the bundle. The inner

diameter of the quartz tube, 110 mm, was equivalent to the inner diameter of a 5.6% creep-pressure tube at its end-of-life [17]. Superheated steam from a low-pressure electric steam boiler was used to heat the empty bundle. In order to reach the required bundle temperature, it became critical to optimize the flow rate of the steam and reduce heat loss. To compensate for the radiative and convective heat losses through the transparent windows, two 10.5 kW and one 6.5 kW Air Torch electric heaters were added to the heated chamber to heat the air in the chamber to the temperatures required for the test.

For the experiment, the steam generator was preheated and the steam mass flow rate of 20g/s was established using the bypass line. Using an argon purge cylinder, the steam superheater was preheated to a temperature of 673 K. Argon was used to help prevent hydrogen from accumulating in the apparatus. The Air Torches were heated to 873 K, stabilizing the air temperature in the chamber at 643 K. Once the steam conditions had stabilized and the bundle temperature had reached 573 K, thermal and deformation data acquisition was started. The bundle temperature was gradually increased to the desired temperature of 1073 K by establishing a temperature program using the Air Torches and the superheated steam. When the temperature of the steam entering the tube reached 593 K, the temperature of the air inside the chamber was 818 K with the Air Torches at 1423 K. As the temperature of the steam increased to 1253 K to attain peak bundle test temperature of 1073 K, the air temperature inside the chamber correspondingly increased to 1028 K. Once the sheath temperatures increased above 1073 K, the empty bundle was held at this high-temperature plateau for approximately 400 s. The cooling phase was initiated at 3000 s into the experiment and lasted roughly 1000 s. [17].

It was observed that while the radial temperature difference of the empty fuel bundle was below 65 K, the temperature across the length of the bundle varied greatly. The axial temperature difference was greater than 100 K and up to 200 K especially during the phase when peak sheath temperature was reached. These temperature gradients were expected given that the method used to heat the bundle had superheated steam flowing in from the upstream end.

Since the deformation data was collected through laser sensors, only the deformation of the outer elements was recorded. The deflection measurements of the fuel elements relevant to this work are presented in Appendix A. Changes in the axial direction were not recorded in the experiment. It should be noted that there was a loss of data acquired by the laser sensors as areas of the fused quartz tube became opaque due to over-heating when the Air Torch temperatures increased above 1273 K. In areas where the tube became opaque, the temperature of the furnace tube was measured by the thermal imager instead of the bundle sheath temperature. Furthermore, discrepancies were observed between the thermal imaging data and the data obtained from the thermocouples. The discrepancy was attributed to the fixed region of interest on the thermal image frame. This meant that if a location of interest was sagging then the previously defined region of interest did not refer to the exact location anymore. By contrast, the thermocouples instrumented throughout the bundle measured the same location during the experiment. A temperature-dependent correction factor was suggested to correct the thermal imager measurements; however, it was deemed beyond the scope and budget of the experiment.

Uncertainties for the deformation measurements were associated with the thermoelastic motion of the quartz tube, where the bundle rests, relative to the laser sensor support frame. Efforts were made to quantitatively correct these results in the lateral direction. It was assumed that element 9 remained in contact with the quartz tube throughout the experiment and therefore, any horizontal displacement of the element would provide an estimate of the systematic error in lateral deformation values. A similar analysis was precluded for the vertical direction on account of differing causes for the vertical deflection of the bottom fuel elements. That is, in addition to the thermoelastic motion of the tube, thermoplastic deformation was observed for the fuel elements 9 and 10.

The sheath temperature distribution and the deformation data, obtained from this experiment, supported the development of the 3-D fuel bundle deformation model in this work. Deformation models typically have fuel linear power and coolant temperatures as boundary conditions [15] [16]. These boundary conditions require the use of a coupled thermal mechanical analysis in order to determine the temperature distribution of the fuel and the sheath before simulating the mechanical deformation. By using the sheath temperature distribution from this experiment as a boundary condition in the bundle deformation model, an uncoupled mechanical analysis can be conducted instead to reduce computational time. Moreover, using the temperature distribution from this experiment meant the deformation data from the model could be validated against the experimental deformation data.

5.3 Material Properties

In order to determine the deformation behaviour of the fuel bundle accurately, it is crucial to first define the parameters specifying the mechanical response of the material. These parameters, known as material properties, are dependent on factors such as temperature, grain size, composition and manufacturing history. The stresses and strains induced in the model due to thermal loading are determined by a number of material properties of the fuel sheath, Zircaloy-4. Since these properties need to be entered in the ANSYS engineering database to define the behaviour of the bundle under the thermal conditions defined above, the range of possible models is limited to those that can be implemented in the finite element software. As fuel pellets will not be modeled, the material properties associated with the fuel pellets are excluded. The material property models used in the deformation model are presented in Section 5.3.1 and 5.3.2.

5.3.1 Zircaloy-4 Properties

To solve the mechanical response of the system, the Zircaloy-4 properties needed for the simulation were density, modulus of elasticity, material plasticity and Poisson's ratio. These properties help determine the sagging of the fuel elements under their self-weight. Since thermal gradients cause axial elongation of the bundle and lead to fuel element bowing, a correlation for thermal expansion was necessary to calculate the thermal response of the simulation. Correlations for thermal conductivity were not needed because measured sheath temperatures were entered as a loading condition for the simulation; this meant that the temperature did not need to be calculated. Moreover, a microstructural creep model was needed to account for bundle slump at high-temperatures.

5.3.1.1 Density

The density of Zircaloy-4 was taken to be $\rho_{Zr-4} = 6550 \text{ kg}\cdot\text{m}^{-3}$ at a reference temperature of 300 K. The density decreases with increasing temperature such that the density at 1200 K is $\rho_{Zr-4} = 6418 \text{ kg}\cdot\text{m}^{-3}$.

5.3.1.2 Modulus of Elasticity

Elasticity describes the ability of an object to resist deformation induced by thermal and mechanical stresses and to return to its original shape when the stress is removed. The property that measures the elasticity of a material is termed the modulus of elasticity or Young's modulus. The correlation describing the modulus of elasticity for Zircaloy-4 as a function of temperature is provided by the following equation [29]:

$$E_{Zircaloy-4} = \begin{cases} 1.088 \times 10^{11} - 5.470 \times 10^7 T & T \leq 1090 \text{ K} \\ 1.017 \times 10^{11} - 4.827 \times 10^7 T & 1090 \text{ K} \leq T \leq 1240 \text{ K} \\ 9.210 \times 10^{11} - 4.050 \times 10^7 T & 1240 \text{ K} \leq T \leq 2030 \text{ K} \\ 1.0 \times 10^{11} & T \geq 2030 \text{ K} \end{cases} \quad (5.10)$$

where T is the temperature in Kelvin and the modulus of elasticity is given in Pa.

This correlation for Young's modulus does not account for the cold-worked manufacturing process of Zircaloy-4, neglecting the effects of material anisotropy. Additionally, the correlation neglects the hardening effects of fast neutron irradiation or the presence of oxygen. Using this approximate model for the modulus of elasticity is justifiable since the plastic strains induced by sheath creep are greater than the relatively small elastic strains.

5.3.1.3 Material Plasticity

Plastic strain was specified using a bilinear model derived by Williams at CNL using the information provided by the MATPRO handbook. The bilinear plasticity model uses a variation of the yield stress model specified in the handbook to provide the plasticity strain component of the mechanical response. The resulting temperature-dependent bilinear curves are illustrated in Figure 12.

The plasticity model used to define Zircaloy-4 is an elastic perfectly plastic material model [22]. The input stress and strain components are true stress and strain values as they are more representative of the state of the material than engineering stress-strain values [29]. The stress increases linearly until the yield strength of the material is reached. After the yield strength, the material does not offer resistance to deformation as shown in the bilinear plasticity model i.e. stress does not increase.

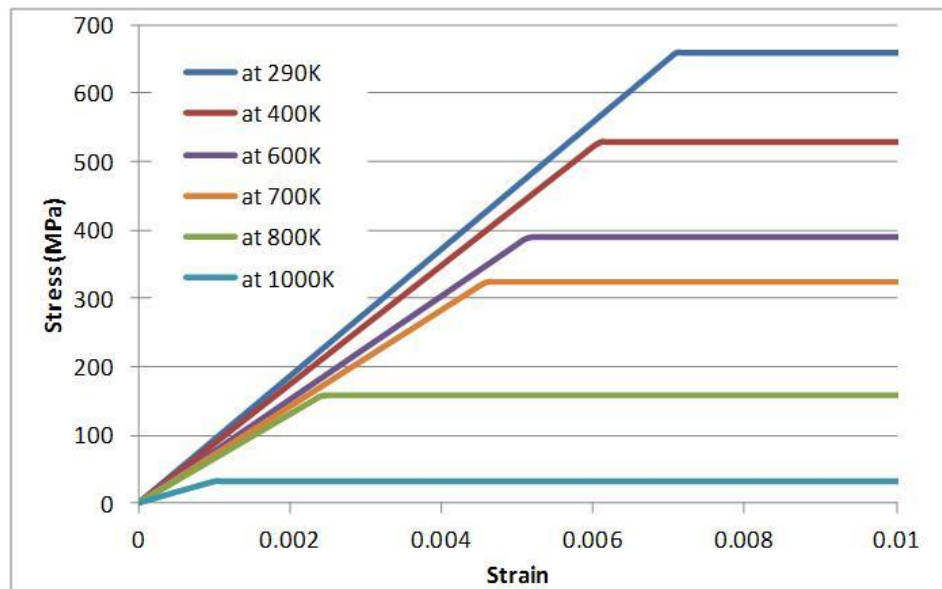


Figure 12: Bilinear plasticity model for Zircaloy-4.

The material model does not account for kinematic strain hardening properties of Zircaloy-4 [47] because the deformation at temperatures above 900 K becomes significantly more strain-rate dependent. Since the strength of the material decreases rapidly with increasing temperature, the strain hardening produced by plastic deformation is countered by thermal creep at high temperatures [25].

5.3.1.4 Poisson's Ratio

Another elastic property that needs to be defined to model the mechanical response of the system is Poisson's ratio. It defines the ratio of the transverse contraction strain to the axial strain. The contraction strain is normal to the applied load while the axial strain is in the direction of the applied load. A value of $\nu_{\text{Zircaloy-4}} = 0.30$ for Poisson's ratio was used for the fuel sheath material. While it is known that the fuel sheath is anisotropic and the exact value of Poisson's ratio would be different in the primary directions, it is assumed that the sheath and the ratio is isotropic as the system is held at a high temperature for an extended period of time [29].

5.3.1.5 Thermal Expansion

The coefficient of thermal expansion used for this model was chosen for consistency with the IST codes, ELESTRES (ELEment Simulation and sTRESses) and ELOCA (Element Loss of Coolant Analysis). The sheath was defined to have a coefficient of thermal expansion of $6.721 \mu\text{m}/\text{m}^{-1}\cdot\text{K}^{-1}$ [48, 49]. This correlation does not account for material anisotropy because Zircaloy-4 tends towards isotropy at the high temperatures (above 1073 K) of interest in this simulation [50].

5.3.1.6 Creep

Creep describes the proclivity of a material to deform permanently overtime due to microstructural change as a result of thermal and mechanical stresses. Of particular interest to this model is diffusional creep because it contributes to the bowing and sagging of fuel elements by accounting for sheath deformation caused by grain boundary sliding. The creep rate is given by the following equation [14] [28]:

$$\dot{\epsilon} = F \left(\frac{\sigma_a}{d} \right)^m e^{-\frac{Q}{T}} \quad (5.11)$$

where $\dot{\epsilon}$ is the strain rate (s^{-1}), σ_a is the applied stress (Pa), d is the grain size: 3 μm for the α -phase and 100 μm for the β -phase, T is the temperature (K), and F , m , and Q are diffusional constants as shown in Table 2.

Table 2: Diffusional Creep Constants.

CONSTANT	α - PHASE	β - PHASE
F	$\frac{6.34 \times 10^6}{G^2}$	0.3
m	2.0	1.9
Q	9431	6039
G is the bulk modulus.		

For this creep model, the $\alpha \rightarrow \beta$ transition occurs at 1080 K. Both α -phase and β -phase creep occur in the simulation for the temperature gradient obtained from the bundle heat-up experiment.

5.3.2 Quartz Properties

Although the pressure tube will be modeled as a non-deforming boundary condition, the material properties of the fused quartz tube used in the experiment were included in ANSYS for completeness. Given that data pertaining to the material properties of the fused quartz tube was not detailed in the experimental report, the material properties for a generic fused quartz tube with excellent optical transmission were used [51]. The relevant material properties are presented in Table 3.

Table 3: Material Properties of Fused Quartz.

PROPERTY	VALUE
Density	2210 kg·m ⁻³
Modulus of Elasticity	74 GPa
Poisson's Ratio	0.17
Linear Coefficient of Thermal Expansion*	0.54 μm·m ⁻¹ ·K

*Valid between temperature range of 273 K to 1273 K.

6 Preliminary Models

Prior to simulating the deformation behaviour of the fuel bundle, it was essential to verify the mechanical, thermal, and creep response of the system. Since the complex geometry of the fuel bundle does not lend itself to an easy analytical solution, it was necessary to illustrate confidence in the modeling technique used for a fuel sheath through comparisons with analytical results before extending the technique to a fuel bundle. A number of preliminary models were developed to verify that the mechanical deformation, non-uniform thermal gradients, and creep deformation were being modeled correctly.

6.1 Flexural Rigidity

As part of the model verification process, the mechanical response of the fuel element was investigated. To characterize the response of the model to mechanical loads, the flexural rigidity of the structure was analyzed. The flexural rigidity of a structure is defined as a measure of its resistance to bending. Investigating the flexural rigidity of the fuel element will help characterize sheath rigidity and provide insight into the loading required to cause contact between the fuel elements and the pressure tube and between fuel elements.

The model under consideration for the flexural rigidity analysis was a 3-D shell-solid assembly composed of two components: the fuel sheath and the brazed appendages. The fuel sheath was modeled as a surface with an outer diameter of 13.10 mm. The thickness was not explicitly modeled; instead, planar elements with defined thickness of 0.38 mm [52] were used. The length was specified to be 484.2 mm as the element model does not include the end-caps. It is not expected that the exclusion of the end-caps will alter the

accuracy of the simulation because the end-caps alone do not offer resistance to thermal deformation [53]. The 3 spacer pads (7.876 mm long) and bearing pads (30 mm long) were added to the surface of the sheath. The exact dimensions are shown in Figure 13.

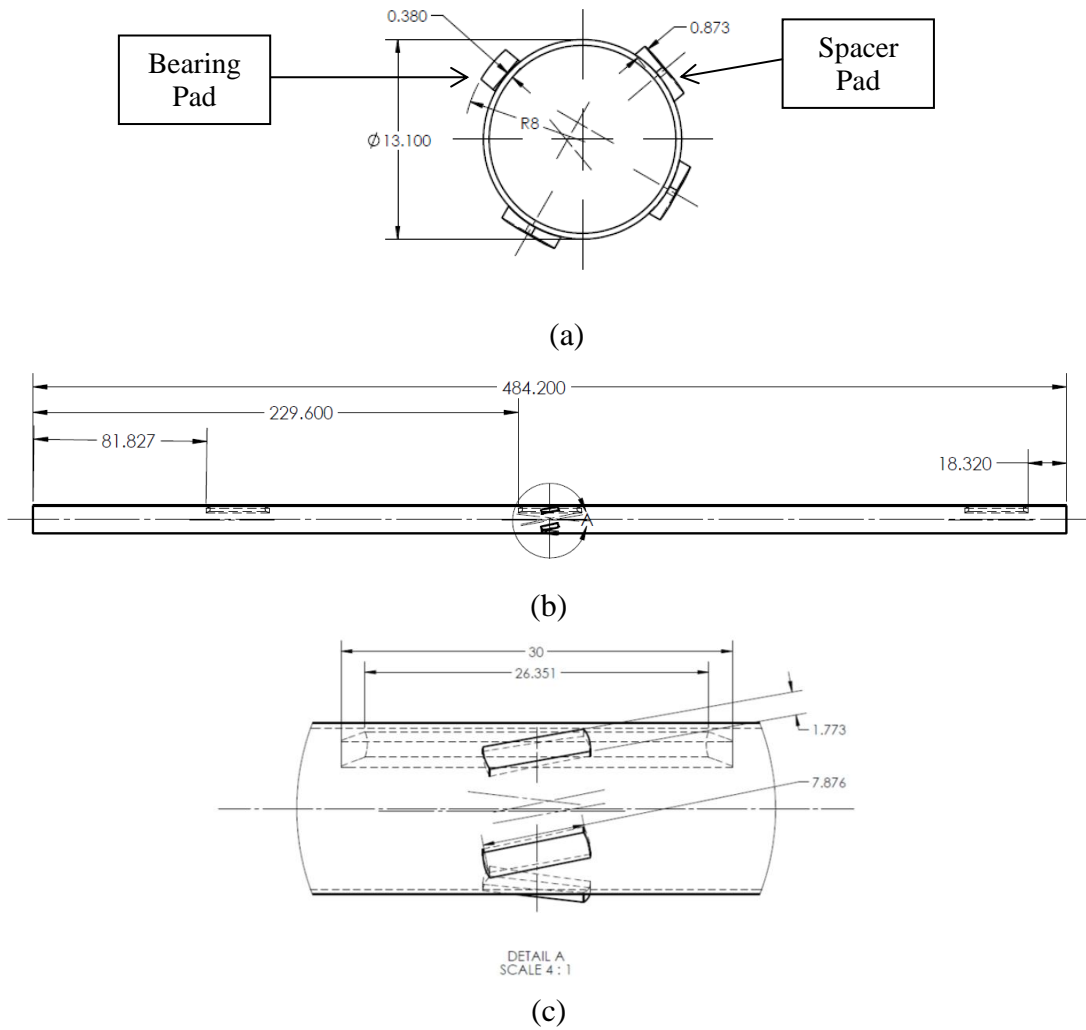


Figure 13: Dimensioned drawings of (a) the sheath cross-section, (b) the fuel sheath, and (c) the brazed appendages. All measurements are given in mm.

The structure was constrained as a simply supported beam, with the upstream end fixed in all degrees of translation and the downstream end free to move axially but constrained laterally and vertically. A point load was applied at the center of the structure

in order to observe the mid-plane deflection. This structural investigation was conducted to determine the flexural rigidity by using the relationship between deflection of the structure and the applied force at the mid-plane. The relationship can be characterized by the following equation: [54]

$$\delta = \frac{-PL^3}{48EI} \quad (6.1)$$

where δ is the vertical mid-plane deflection, P is the applied load at the mid-plane, L is the length between the supports of the structure, and EI refers to the flexural rigidity. The moment of inertia, I, for the hollow tube is calculated using:

$$I = \frac{\pi}{4}(r_o^4 - r_i^4) \quad (6.2)$$

where I is the moment of inertia in mm^4 , r_o and r_i are the outer and inner radius respectively in mm.

The effects of gravity and material creep present in the fuel element deformation model were removed to ensure that the simulation matched the conditions of the analytical calculations. A vertical load of 200 N was applied at the mid-plane of the sheath. The load corresponds to a pressure of approximately 130 MPa. It was selected based on the previous flexural rigidity studies conducted by Gamble [43] and Krasnaj [16]. The fuel sheath was heated to 1163.2 K to be consistent with the temperatures used in the deformation model. The boundary and loading conditions for the simulation are illustrated in Figure 14.

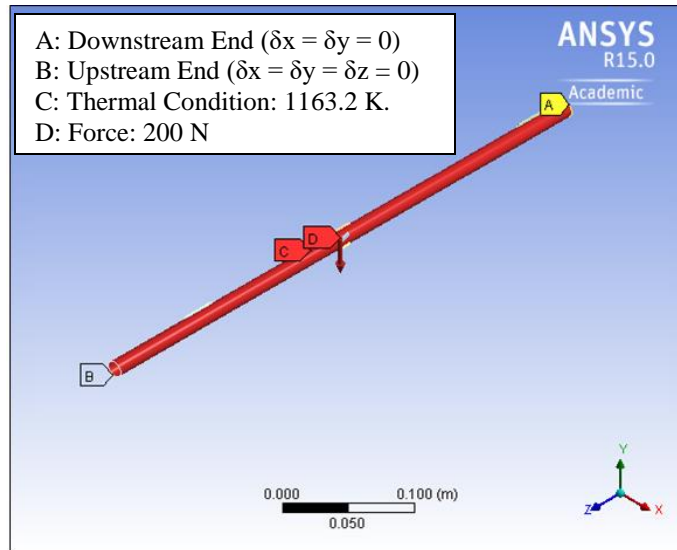


Figure 14: Boundary and loading conditions of the flexural rigidity model.

Since the effects of material creep were not being considered, the linear analysis was conducted in one load step. The vertical deflection results from the linear analysis are represented in Figure 15.

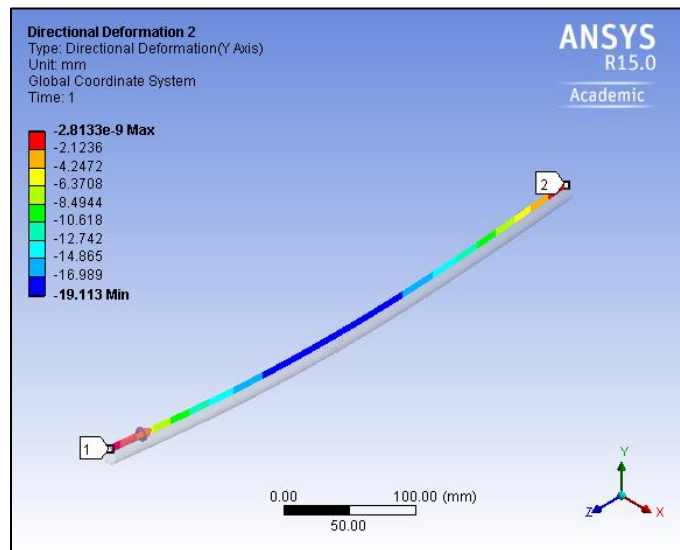


Figure 15: Vertical deformation of the flexural rigidity model [mm].

The figure indicates that the sheath deflected downwards by 19.113 mm at the mid-plane under the applied load of 200 N. The general profile appears to be correct since the

load is applied at the mid-plane where the maximum deflection occurs. The mid-plane deflection was benchmarked against analytical calculations to illustrate confidence in the simulation results. The deflection results are shown in Table 4.

Table 4: Validation of Sheath Rigidity Results.

	MID-PLANE VERTICAL DEFLECTION [MM]	FLEXURAL RIGIDITY [N M²]
ANSYS	19.11	24.76
ANALYTICAL	18.97	24.95

As evident from the table above, the deflection results obtained from ANSYS are in excellent agreement with the analytical calculations. The mid-plane deformation results are within 0.74% of the analytical values. This result is encouraging in determining sheath rigidity because the calculations for flexural rigidity rely on the deformation values from the simulation. The flexural rigidity was determined by substituting the value of mid-plane deflection obtained from the simulation into equation 6.1. Given that the applied load and the length of the fuel sheath under the applied thermal loading were known, the sheath rigidity was calculated.

The comparison of sheath rigidity results shows good agreement between the simulation and the analytical calculations. It is interesting to note that the flexural rigidity value calculated by the simulation is slightly lower than the corresponding analytical solution. This contradicts the expectation that the ANSYS results would be slightly greater than the analytical calculations due to the additional structural strength provided by the brazed appendages in the simulation. The discrepancy between the two values can be

attributed to the fact that ANSYS results provide an approximation of the exact solution because the FEM uses a finite number of degrees of freedom to solve the problem. It is likely that the slight difference of 0.76% between the simulation and the analytical values is due to the discretization error.

The deformation behaviour of the element is of particular interest at higher temperatures and it is important that the model simulates the mechanical response of the element correctly. The results from this analysis can be used to determine the regions where maximum displacement occurs and whether the displacement is large enough that the spacer pads of the fuel pins come into contact with each other. Analyzing the flexural rigidity helps characterize the deformation behaviour of the fuel element due to applied mechanical loads. The concurrence between the sheath rigidity values obtained from the simulation and analytical calculations demonstrates that the mechanical response of the structure is correctly modeled.

6.2 Thermal Bowing

Non-uniform temperature distributions can be seen across the length and across the cross-section of the fuel element during off-normal or accident conditions. These non-uniform distributions can cause thermal bowing. The temperature gradients result in bowing of the fuel elements due to changes in temperature-dependent mechanical properties and uneven thermal expansion. Thermal bowing behaviour of the elements is a primary concern because it negatively impacts the effectiveness of the coolant by reducing sub-channel geometry and coolant flow. Therefore, it is necessary to understand and verify

the response of the fuel element to bending moments caused by non-uniform temperature distribution.

An analysis was conducted to investigate thermal bowing behaviour of the fuel element. The assembly used in this analysis was identical to the one described in Section 6.1. As in the flexural rigidity study, the fuel element was represented as a simply supported beam. Under these boundary conditions, the deflection of the empty fuel element due to thermally generated moments can be characterized by the following equation [54]:

$$\delta = \frac{-\alpha L^2}{16b} (\Delta T_i) \quad (6.3)$$

where δ is the vertical mid-plane deflection, α is the linear coefficient of thermal expansion, L is the length between the supports of the structure, b is the outer sheath radius, and ΔT_i refers to the difference between the minimum and maximum temperature applied from the top to the bottom of the structure, i.e. $\Delta T_i = T_{max} - T_{min}$.

The thermal load applied was a linear temperature gradient across the diameter of the fuel element with differences of 50 to 200 K from the top of the element to the bottom. The temperature range was selected to simulate the diametric temperature gradients observed in the in-laboratory experiment [17]. The gradients were applied such that the bottom of the element was at the maximum temperature and the top of the element was at the minimum temperature. The bottom of the element, $y = -6.55$ mm, was kept at 1163.2 K to correspond to the maximum temperature recorded during the experiment. The temperature of the top of the element, $y = 6.55$ mm, was varied in order to achieve gradients of 50 K, 65 K, 100 K, 150 K and 200 K. An example of a linear temperature gradient is illustrated in Figure 16. Inputting this temperature gradient ensured that a downward

deformation profile would be obtained. This is because the element bows in the direction of the hotter side to compensate for the increase in axial strain as the temperature gradient across the diameter of the fuel element increases.

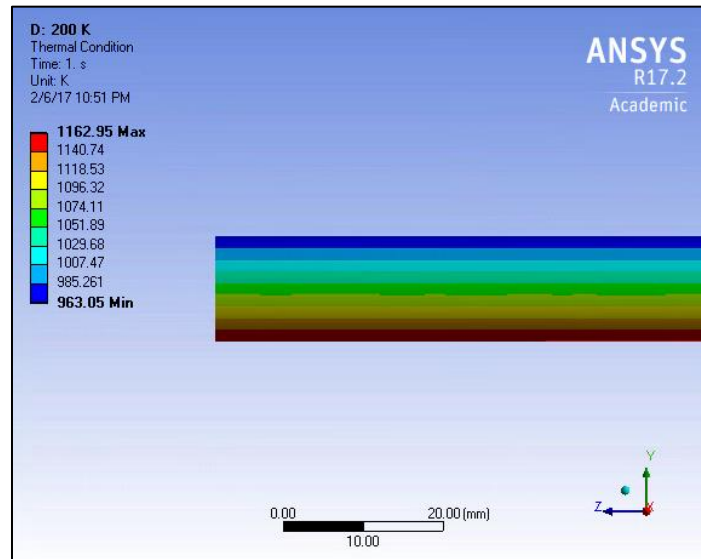


Figure 16: Temperature gradient of 200 K across the diameter of the sheath.

The effects of gravity and material creep were excluded to ensure that the simulation followed the conditions assumed for the analytical calculations. A linear analysis was conducted for thermal gradients ranging from 50 K to 200 K. The vertical deflection profiles of the element under varying thermal gradients from the numerical simulation are illustrated in Figure 17.

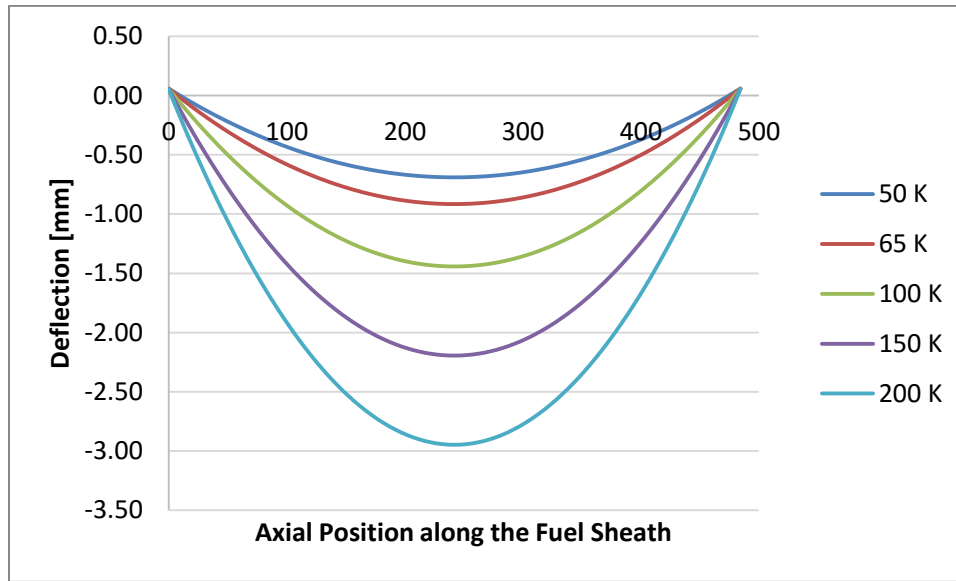


Figure 17: Deflection of the fuel element due to thermal gradients ranging from 50 K to 200 K.

An increase in the thermal gradient across the diameter results in increased deflection as evident in Figure 17. This is consistent with expected results because the difference between the minimum and maximum temperature across a structure, ΔT_i , is proportional with the deflection, δ , of the structure as per equation 6.3. The general deflection profile appears to be correct since the maximum deflection is seen at the mid-plane. Maximum deflection at the mid-plane was anticipated given that the element is modeled as a simply supported structure. The mid-plane deflection results were benchmarked against analytical solutions to illustrate confidence in the simulation results. The comparison results are shown in Table 5.

Table 5: Comparison of Deflection Results due to Thermal Bowing.

TEMPERATURE GRADIENT [K]	MAXIMUM THERMAL BOW		
	ANSYS [MM]	ANALYTICAL [MM]	DIFFERENCE (%)
50	-0.7642	-0.7521	1.61
65	-0.9890	-0.9777	1.16
100	-1.5140	-1.5042	0.65
150	-2.2641	-2.2563	0.35
200	-3.0149	-3.0084	0.22

As evident from Table 5, the deflection results obtained from ANSYS show good agreement with the analytical solutions. There exists an inverse correlation between the temperature gradient and the percent error. As the difference between the minimum and maximum temperature applied to the element increases, the discrepancy between the results from the model and the analytical calculations decreases. The discrepancy decreases because the maximum thermal bow increases, resulting in a lower percentage deviation even though the absolute difference between the ANSYS solutions and analytical calculations remain approximately constant.

It should be noted that the maximum thermal bow calculated by the simulation is slightly higher than the corresponding analytical calculation for all temperature gradients. This discrepancy can be explained by idealization errors in the simulation. The shell

elements used to represent the fuel element do not display a realistic temperature gradient through their thickness because only one element can be defined through the thickness of the sheath. In this case, the temperature–dependent material model would use an averaged value to calculate the thermal bow through the thickness of the sheath instead of the exact value, resulting in higher deflection values. While the idealization of element type is advantageous in reducing computational time to achieve convergence, it also results in solutions that differ slightly from the corresponding 3-D model. Moreover, the geometry of the element was simplified in the analytical calculations to exclude brazed appendages. Hence, it is likely that slight differences between the simulation and the analytical values are due to the idealization of the complex geometry

The bowing behaviour of the element is of particular interest at higher temperatures. Therefore, it is important that the model correctly simulates the thermal bowing response of the element. The agreement between the results acquired from the simulation and the analytical calculations for the maximum thermal bow demonstrates that the thermal response of the structure is implemented correctly with respect to the theoretical model. Characterizing and verifying the bowing behaviour of the fuel element due to the applied temperature gradients improves the understanding of the dominant deformation mechanisms that contribute to the structure’s thermal-mechanical response under off-normal or transient conditions.

6.3 Creep Deformation

It is necessary to verify that the creep behaviour predicted by ANSYS is in line with analytical results. In order to illustrate confidence in the creep strain results obtained from

ANSYS, a simple uniaxial test case was considered to benchmark the creep model [55] [56].

A hollow cylinder representing the fuel element in the bundle was used for the study. The cylinder was meshed using SOLID186 elements that support material creep and plasticity. Solid elements were used instead of shell elements to ensure that the tensile load could be applied to the cross section of the sheath, rather than the edge. The temperature of the structure was increased to 1080 K and the structure was held isothermally in the subsequent load steps. The upstream face of the cylinder was fixed in all degrees of translation and a uniform static tensile load of 20 N was applied to the downstream face and remained throughout the 400s of the analysis. This tensile load was a fictive load applied to investigate that the creep model was being implemented correctly in the simulations. The force generated an equivalent stress of 1.317 MPa. The material model was altered to exclude thermal expansion and thermal strain values. Additionally, gravitational force was not applied. This was done to be consistent with the assumptions made for the hand calculations. The model with the applied boundary conditions is shown in Figure 18.

The creep law from Section 5.3.1.6 was applied along with the elastic properties of the material. The initial stress state with 20 N applied was solved in load step one with creep effects turned off for time-step of 1e-8s. Once the initial stress state is solved, the creep effects were turned on and the analysis was conducted for 400 s in load step two. The strain results from the model are shown in Figure 19.

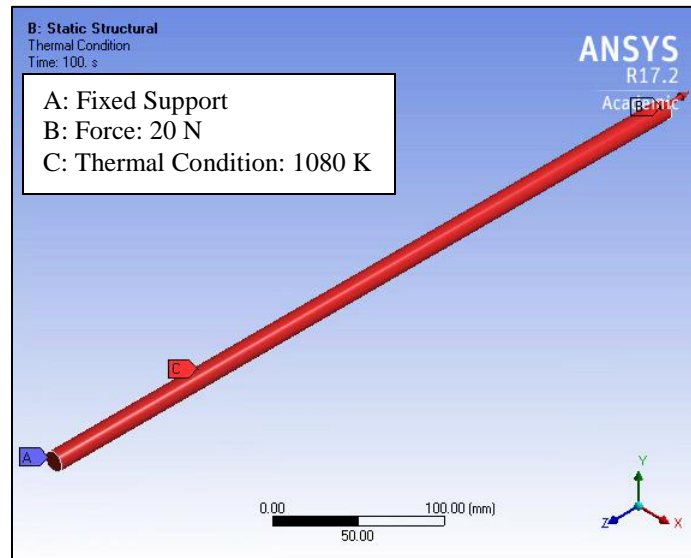


Figure 18: Boundary conditions of the creep verification model.

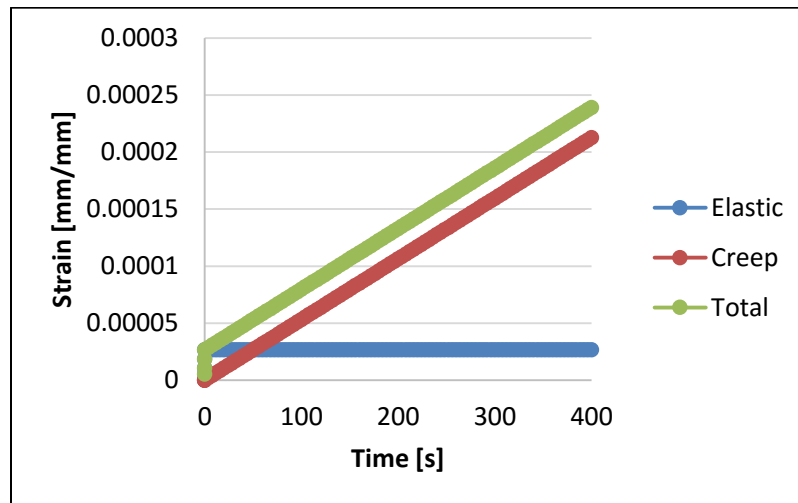


Figure 19: Strain as a function of time.

The equivalent stress of 1.317 MPa applied to this structure generates an elastic strain of 2.923×10^{-5} mm/mm, which is congruent with hand calculations (see Appendix B). This initial stress state is established in 1×10^{-8} s and the stress and elastic strain values remain constant for the remainder of the simulation. The total strain illustrated is the sum of elastic and creep strain since thermal strain was excluded to maintain consistency with the

assumptions for the analytical results. The relationship between creep strain and time is linear. This linear relationship is because the creep rate becomes constant overtime, equaling $\dot{\epsilon} = 5.315e-7 \text{ s}^{-1}$. The creep rate from equation 5.17 becomes constant because the applied stress values and the temperature remain constant through load step two.

The creep calculation was compared against analytical calculations and a sensitivity study for the optimal creep strain ratio was conducted. The creep strain ratio is a measure used by the ANSYS solver to ensure the creep response is appropriately calculated because creep is a path-dependent phenomenon. The ratio compares the equivalent creep strain increment, $\Delta\dot{\epsilon}_{cr}$, with the modified elastic strain, ϵ^{et} , as shown in equation 6.4

$$C_s = \frac{\Delta\dot{\epsilon}_{cr}}{\epsilon^{et}} \quad (6.4)$$

The ratio ensures that the increment of creep strain added at each step remains within reasonable limits. The values for the creep strain ratio considered in this study were 0.1 and 1. The results from the sensitivity study and the comparison to analytical calculations are summarized in Figure 20.

The calculations for the analytical results are shown in equations B-4 to B-6 in Appendix B. The results indicated that the creep strain values matched to within 0.0016% of the analytical solution at creep ratio of 1. Decreasing the creep ratio to 0.1 brings the creep strain values to within 0.0006% of the analytical solution. The consensus between the analytical results and the simulation results verifies that the creep model is being correctly implemented. It also provides a measure of confidence in the creep strain results obtained from the simulation.

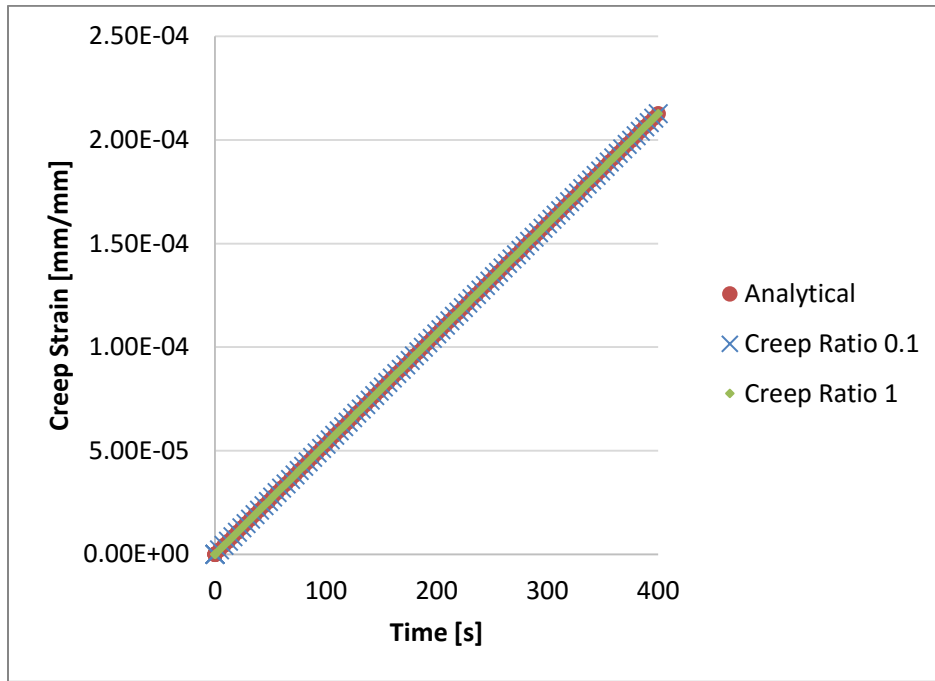


Figure 20: Comparison of simulation and analytical creep strain.

While the results become more accurate when the creep limit ratio is lowered, constraining this iteration parameter requires an excessive amount of solution time. The increase in accuracy gained by reducing the value of the creep ratio is not worth the additional time required to achieve convergence. As the ultimate intent of this thesis is to expand the fuel element deformation model to a bundle deformation model, it becomes imperative to strike a balance between the accuracy of the solution and the time needed to obtain convergence. For this reason, it is recommended that the creep ratio be restricted to 1 for the bundle model because it provides a converged solution close to the analytical solution in a shorter amount of time.

6.4 Conclusion

In conclusion, multiple simulations were conducted to characterize the high-temperature deformation behaviour of an empty fuel element and to determine the accuracy and credibility of the modeling technique used. These studies seek to verify that the simulation matches the specifications and assumptions with respect to the conceptual model. The results for flexural rigidity, thermal bowing and creep deformation were in excellent agreement with analytical results. The simulation model was then extended to a fuel element model that amalgamates the phenomena studied in the preliminary models.

7 Fuel Element Deformation Model

To lay the groundwork for the development of an empty bundle deformation model, the general deformation behaviour of a single fuel element was first simulated. Since a fuel bundle comprises of multiple fuel elements, it was deemed necessary to characterize the behaviour of an individual fuel element at high temperatures of 1163.2 K before simulating the behaviour of 37 fuel sheaths in the configuration of a fuel bundle. The primary objectives of characterizing the high temperature behaviour of an empty fuel element were to investigate the bowing and sagging behaviour under off-normal conditions and to verify that the nonlinear material model was implemented correctly.

7.1 Model Description

The assembly analyzed in this report is illustrated in Figure 21 . It is composed of a thin cylindrical fuel sheath with the spacer and bearing pads fused. The alignment of the brazed appendages corresponds to that of brazed appendages in the outer fuel sheaths of a CANDU bundle. Since the fuel elements are held in the configuration of a bundle by endplates, it is important for the element model to be constrained in a manner consistent with the fuel bundle model in Section 8. Therefore, the upstream end of the sheath will be fixed in all directions while the downstream end will be free to expand axially. This constraint ensures that the fuel element can expand as a result of the thermal loading applied and rigid body motion does not occur. The objective of the analysis is to determine the deformation behaviour of the fuel element at temperatures relating to off normal conditions.

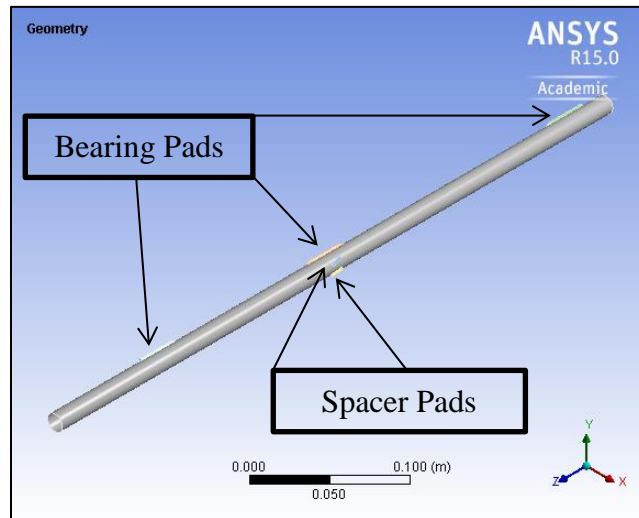


Figure 21: Physical structure used in the fuel element deformation model.

7.1.1 Physical Geometry

The assembly under consideration in this analysis is identical to the assembly detailed in Section 6.1.

7.1.2 Material Properties

The sheath and appendages are made from Zircaloy-4. The material property models used for the alloy are described in Section 5.3.1.

7.1.3 Element Type and Mesh

Reviewing the state of the art, it is evident that different element types such as beams and solids have been used in modeling the fuel sheath [12] [16] [40]. Solid elements have the advantage of displaying a more realistic result gradient through its thickness when at least two to three elements are defined through the thickness of the structure. This is not pragmatic for a fuel bundle model because using multiple solid elements through the thickness of the sheath would result in a very computationally intensive model. Since the

primary interest of this thesis is to simulate the deformation behaviour of the fuel elements, shell elements were considered to represent the fuel element instead of solid elements. Selecting shell elements to represent the element would be acceptable as the length of the fuel element is roughly 1270 times greater than its thickness (i.e. 484 mm in length compared to 0.38 mm in thickness). The advantage of selecting shell elements would be the reduced computational time as they allow for the modeling of thin features with only one element through the thickness. In order to decide whether shell elements would be suitable for modeling the deformation of the fuel element, a preliminary study was conducted to compare the deformation results of a fuel sheath represented by solid elements with one represented by shell elements. The appendages were represented by solid elements for both models.

The study used the physical geometry and material properties detailed in Sections 6.1 and 7.1.2 respectively. For the solid fuel element model, a mesh composed of higher order quadrilateral elements (SOLD186) was specified. Despite this, some tetrahedral elements were used where the brazed appendages shared nodes with the fuel sheath. The motivation for specifying quadrilateral elements was to obtain a mesh that would be consistent with the mesh in the shell model, which used higher order quadrilateral elements (SHELL281). Making comparisons with similar meshes takes the mesh quality out of consideration. The size of the quadrilateral and quadratic elements in the solid and shell models was set to 1 mm. A higher order sweep mesh producing uniformly shaped quadrilateral elements was used for the bearing pads and spacer pads. The meshes for the two models are illustrated in Figure 22.

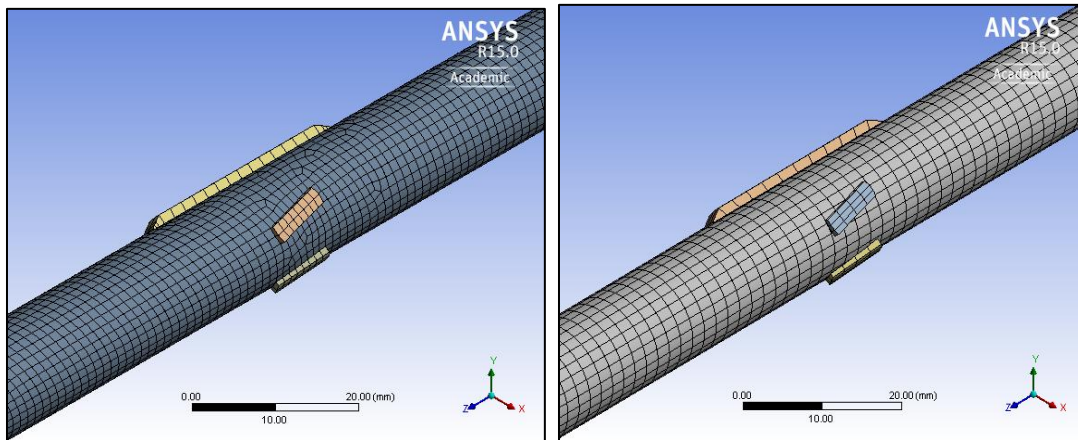


Figure 22: Finite element mesh of the solid (left) and shell-solid models (right).

These models were constrained as a simply supported structure by defining a displacement of zero in all directions at the upstream end and a displacement of zero in the X- and Y-direction at the downstream end. A Dirichlet boundary condition of 1163.2 K was applied over the entire structure. The resulting total deformation profiles from both the solid and shell-solid model are shown in Figure 23.

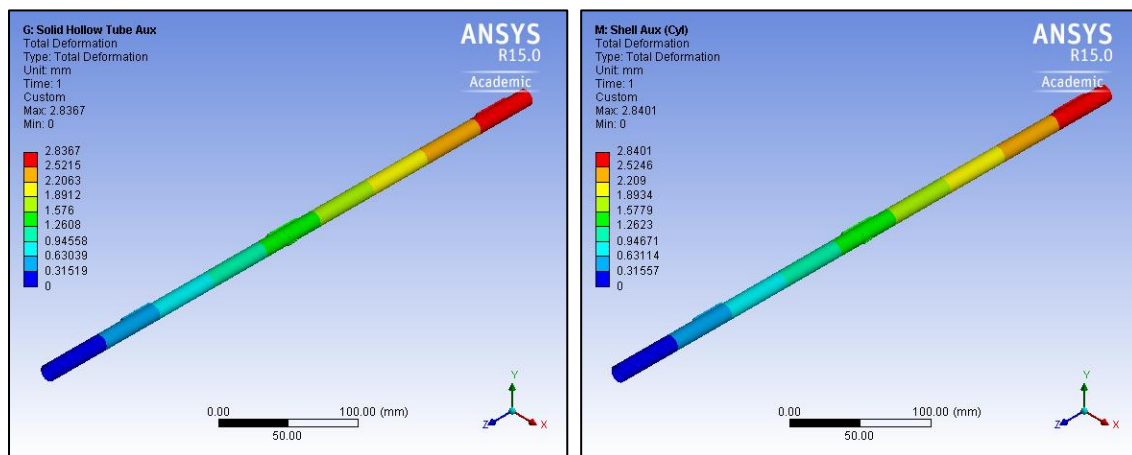


Figure 23: Total deformation of the fuel element using the solid model and the shell-solid model.

The total deformation results indicated that the fuel elements heated to 1163.2 K deformed to the same degree for both the solid and shell-solid models. Comparing the two deformation profiles, it becomes evident that the models are consistent with one another. In order to illustrate confidence in the results, the axial deformation at the free end, thermal strain and radial expansion of the fuel sheaths were calculated using equations B-7 to B-9 in Appendix B and compared between the two models as shown in Table 6.

Table 6: Comparison of the Results of the Solid and Shell Models to the Analytical Solution.

	SOLID MODEL	SHELL MODEL	ANALYTICAL
AXIAL DEFORMATION [MM]	2.827	2.828	2.825
DIFFERENCE [%]	0.071	0.106	
THERMAL STRAIN [10^{-3} MM/MM]	5.834	5.833	5.833
DIFFERENCE [%]	0.009	0.005	
RADIAL EXPANSION [10^{-2} MM]	3.835	3.830	3.823
DIFFERENCE [%]	0.315	0.185	

Comparison of the axial deformation, radial deformation and thermal strain for both models show good agreement with the analytical results. Significant variation between the results was not expected because the thermal load was uniform and other complicating factors like creep were not included in the model. The discrepancy between the simulations

and the analytical calculations was greatest for radial expansion. This was expected given that the appendages were not included in hand calculations. The result verifies the hypothesis that the shell sheath with solid auxiliaries would provide the same deformation result as a solid element sheath with auxiliaries. The deformation data is congruent with values obtained from hand calculations, indicating that the material data input into ANSYS was correctly applied for the given thermal loading in both models.

Since the deformation profiles between the two models were identical, the comparison study illustrated that 3-D shell elements could be used instead of solid elements to model the fuel element. This preliminary study sets the stage for the bundle model as shell elements are less computationally intensive than solid elements. Reduced computational time would be valuable in this work due to the sheer volume of fuel elements that need to be simulated.

Using the above study as a starting point, higher order quadrilateral shell elements were used to represent the fuel sheath in the Fuel Element model. The thickness of the shell surface was specified to be 0.38 mm, which is consistent with the thickness of a fuel sheath used in the bundle heat-up experiment. A higher order sweep mesh producing uniformly-shaped tetrahedral elements was used for the solid auxiliaries. The element sizing was further refined to 0.5 mm to increase the mesh density for the fuel element model. The resulting mesh contained 55,667 nodes and 19,279 elements and is shown in Figure 24.

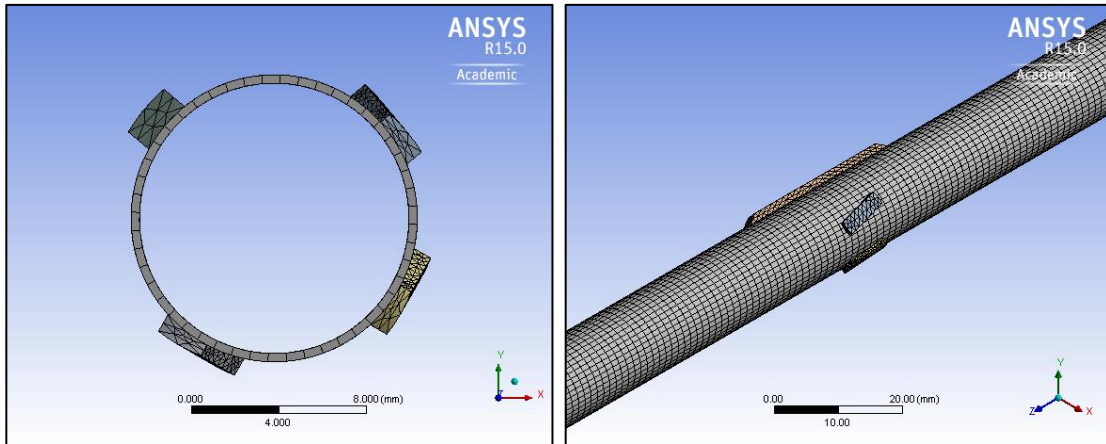


Figure 24: Composite mesh composed of higher order elements for the fuel element deformation model.

7.1.4 Loading and Boundary Conditions

The shell cylindrical sheath and the solid bearing and spacer pads form the 3-D shell-solid assembly used in this model. Although nodal compatibility is not needed between the shell element mesh and the solid element mesh, it is necessary to provide a transition from the shell element region to the solid element region. The connection between the solid pads and the shell sheath was achieved through bonded contact rather than node compatibility. For this analysis, the contact surface was defined to be the outer surface of the shell sheath and the target surfaces were defined to be the inner faces of the corresponding solid brazed appendages. This is in accordance with the shell-solid assembly modeling approaches specified for ANSYS Workbench [23, 46]. The contact pairs are illustrated in Figure 25.

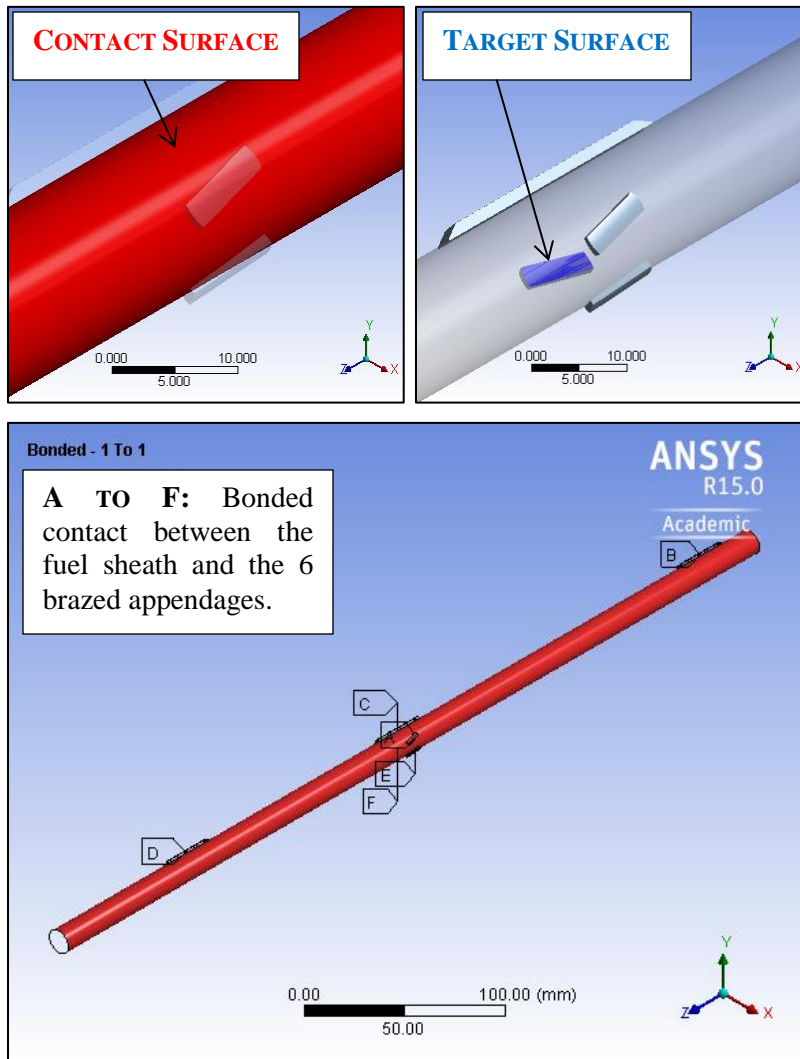


Figure 25: Contact pairs of the 3-D shell-solid assembly.

As mentioned above, the element can be represented as a simply supported structure. This is to maintain consistency with the bundle from the experiment, which was allowed to expand axially under a thermal load in the quartz tube. Nodes at the upstream end (positive Z-direction) of the fuel element were constrained in all directions by stipulating a displacement of zero at the nodes on the bottom of the element. At the downstream end, displacement in the X- and Y-direction was detailed to be zero. For the purposes of model

development, a uniform thermal load of 1163.2 K was applied to the shell sheath and the solid appendages. This temperature corresponds to the maximum temperature observed in the experiment. Gravity in the negative Y-direction was specified in order to be consistent with the in-laboratory experiment. A graphical representation of the boundary conditions is illustrated in Figure 26.

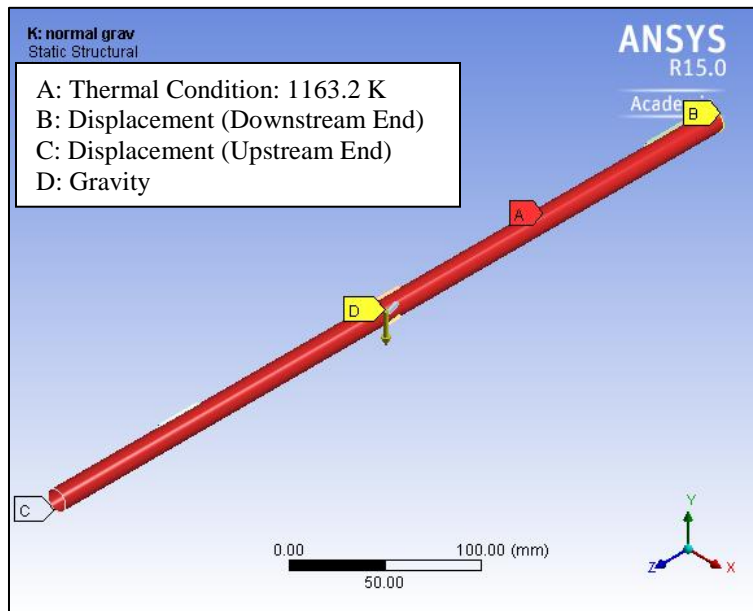


Figure 26: Loading and boundary conditions of the assembly.

In order to include the effects of material creep, it was necessary to split the loading into two load steps:

1. Load Step One: The described displacement constraints were applied at the respective ends of the element. In addition to this, gravitational force and the temperature of the element was increased from 303.15 K to 1163.2 K load. The creep strain calculations were turned off during the first load step of the analysis in order to establish initial conditions. A very small end time value of $1e-8$ s was set for this load step to allow

the initial stress state to be solved. This meant that the first load step effectively represented a static structural analysis with no creep effects included.

2. Load Step Two: The creep strain calculations were turned on during the second load step while the existing loading and boundary conditions stayed constant. This ensured that rigid body motion did not occur as the model was sufficiently constrained at all times. The end time for load step two was defined to be 400 s, coinciding with the time the bundle was in the high-temperature plateau in the experiment.

7.1.5 Solution

The static structural analysis was conducted with the assumption that large deflections would not occur under the loading conditions specified. In a static analysis, time does not represent physical time; rather it shows that 100% of the first load step is applied at the end of 1e-8 s. The second load step, which starts at the end of load step one, has an end time of 400 s. This means that the creep strain rate is integrated over this time range, with each sub-step acting as an increment of time, Δt .

Since material creep is incorporated, it is necessary to perform a nonlinear analysis. The settings were adjusted such that auto time stepping was turned on and the model was run with 50 initial sub-steps to a maximum of 250 sub-steps. This ensures that at least 50 results sets were extracted to see how the deformation of the fuel element varies with each sub-step. The stress results were expressed using the Equivalent Von-Mises contour plots.

7.2 Results

Using the parameters stated above, a nonlinear contact analysis was conducted. The applied loading conditions caused the fuel element to expand axially and diametrically. A slight vertical deflection was also seen at the center of the element due to the gravitational force applied. The results indicated that a uniform thermal load of 1163.2 K incurred a maximum axial deformation of 2.80 mm in the Z-axis. A graphical representation of the axial deformation is shown in Figure 27.

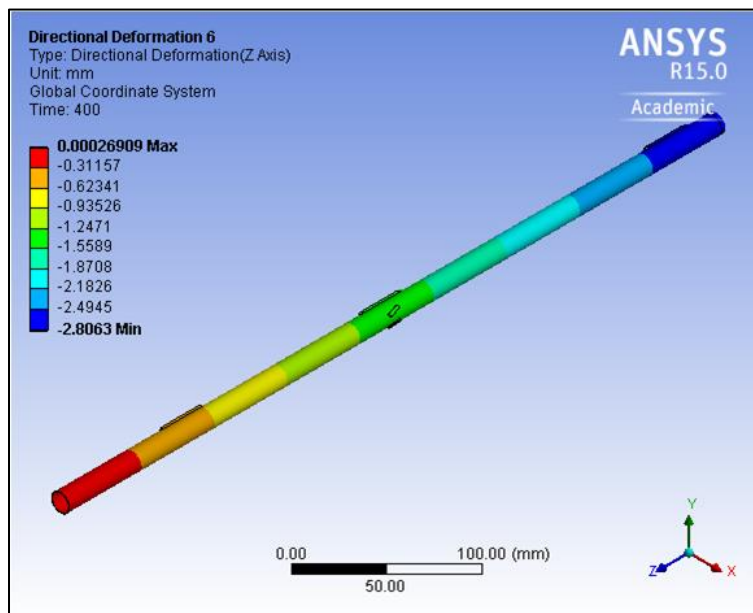


Figure 27: Axial deformation of the fuel element in [mm].

In order to determine the radial deformation, the coordinate system was changed from Cartesian coordinates to cylindrical coordinates, where X is the radial direction, Y is the tangential direction and Z is the axial direction. The cylindrical coordinate system is shown in Figure 28.

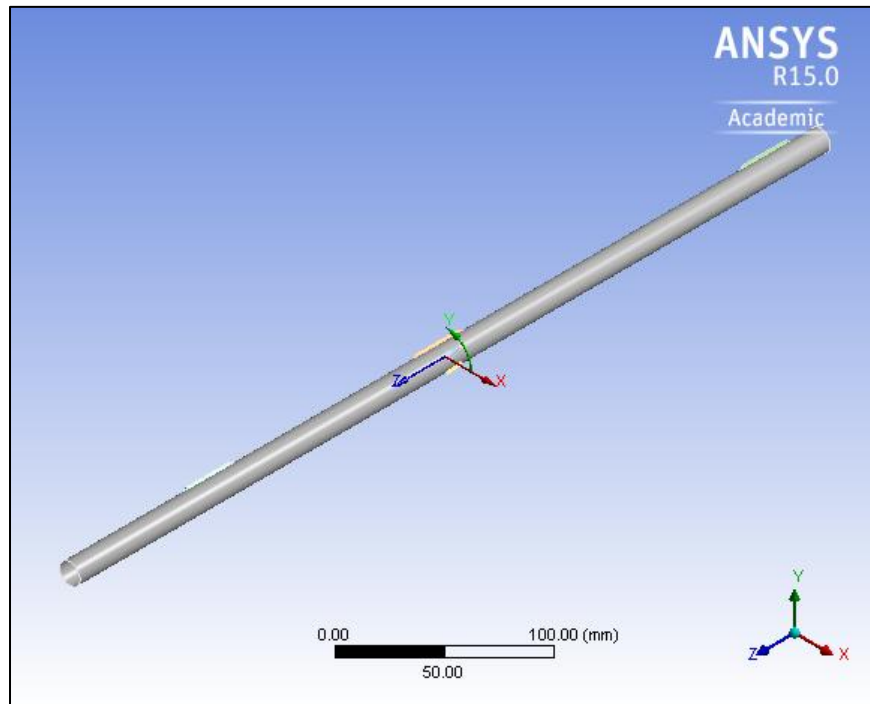


Figure 28: Cylindrical coordinate system.

The results were extracted at the mid-span of the fuel element, away from the locations where boundary conditions were applied. As illustrated in Figure 29, an average diametric deformation of $7.573e-2$ mm occurred due to the loading conditions applied. The inclusion of the bearing and spacer pads at the mid-plane may result in the non-symmetric radial deformation. Due to this, the diametric deformation was calculated by summing the deformation in the lateral and vertical direction for the X-axis in cylindrical coordinates.

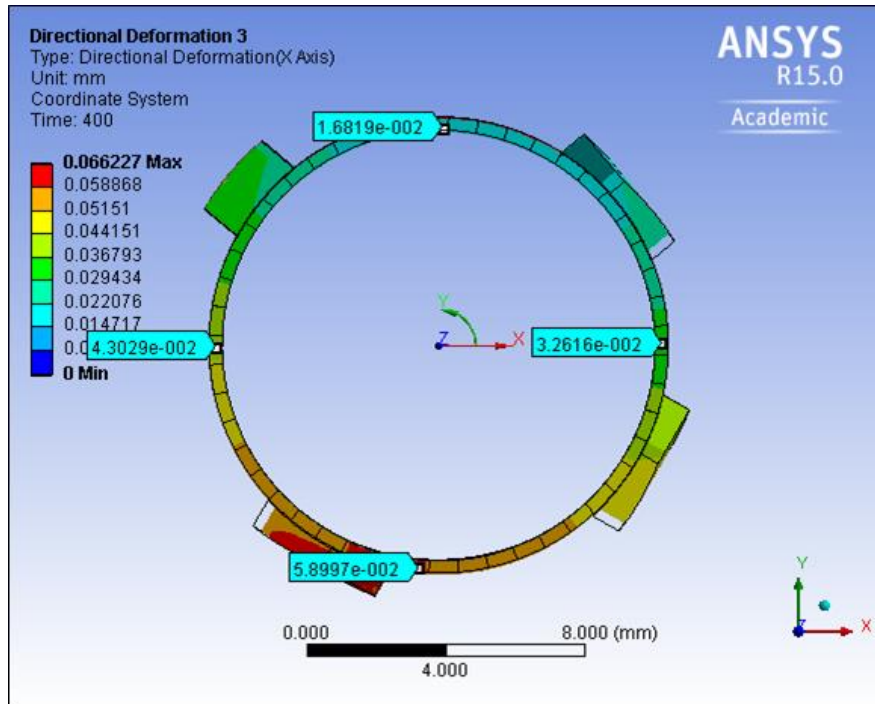


Figure 29: Diametric deformation of the fuel element.

The vertical deflection was obtained from ANSYS by specifying a central path along the length of the top of the fuel sheath. As demonstrated by Figure 30, the vertical deflection is greatest at the center of the fuel element, which is concurrent with the expected deformation profile. The deformation at the center occurs due to the sagging of the fuel element under its weight at high temperatures. The values illustrated in this figure need to be normalized such that the deformation at the ends is equal to zero as per the boundary conditions. A graph was created to represent the normalized deflection profile and is shown in Figure 31.

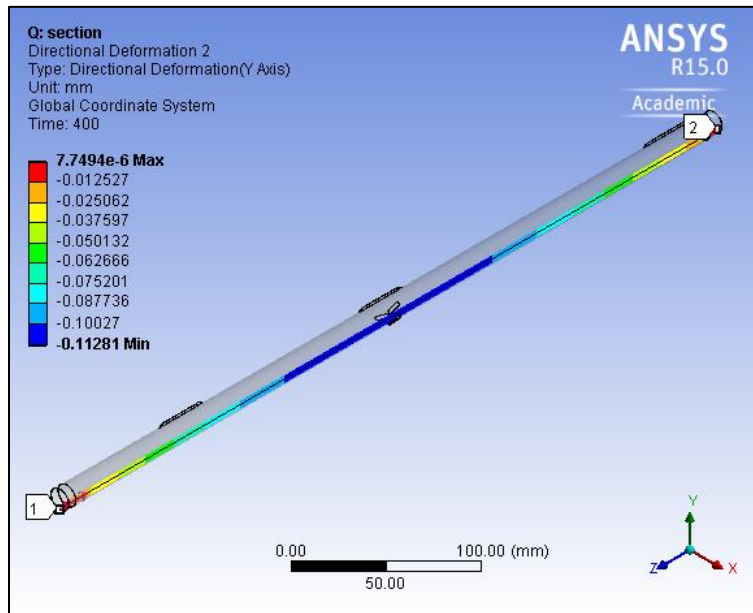


Figure 30: Vertical displacement across the length of the fuel element [mm].

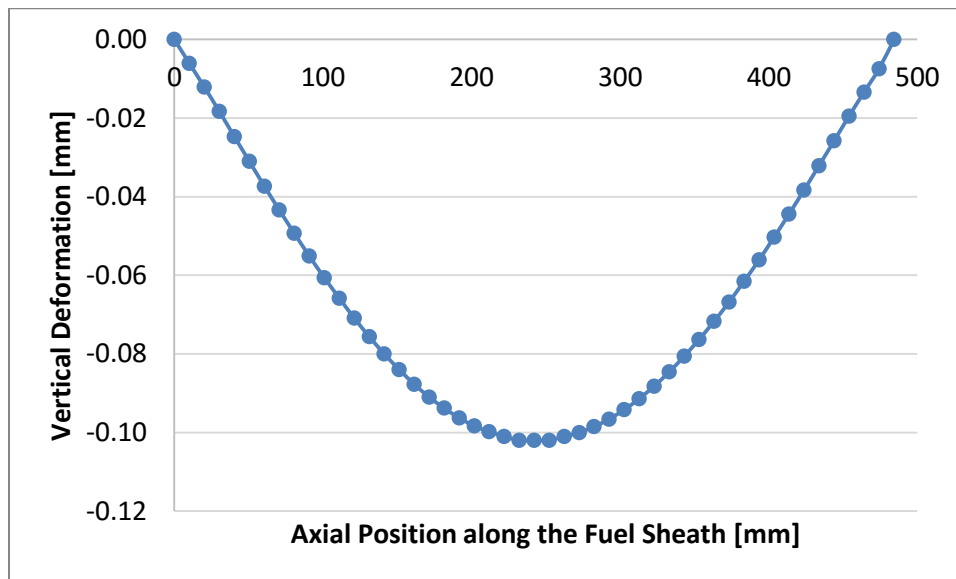


Figure 31: Normalized vertical deflection of the fuel element due to bending [mm].

The maximum vertical deflection of the fuel element was 0.113 mm at the center of the fuel element. The overall deformed shape of the model is consistent with the results anticipated for a simply supported beam undergoing gravitational loading.

The stress distribution profile of the assembly resulting from the application of the gravitational force, thermal load, and material creep is illustrated in Figure 32.

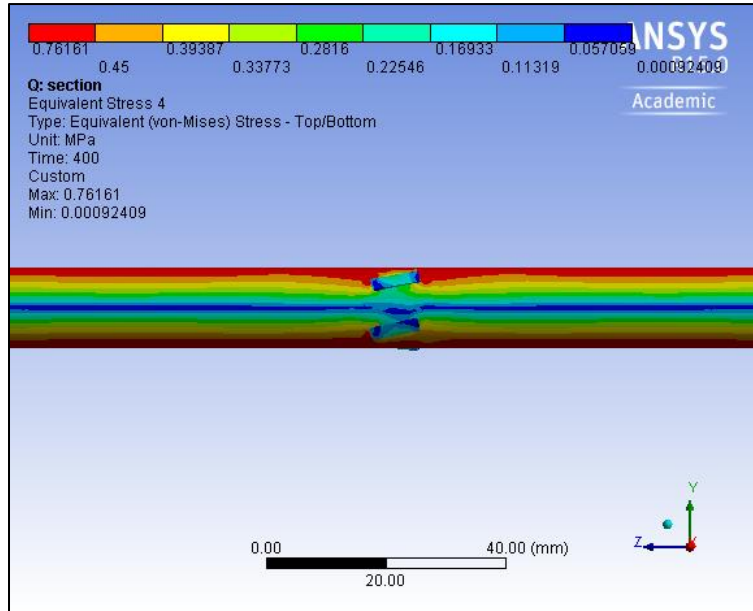


Figure 32: Equivalent Von-Mises stress [MPa] across the fuel element due to bending.

The bending stress profile across the fuel element is identical to the expected profile for a simply supported structure undergoing a uniformly distributed load. In this case, the uniform load is the self-weight of the element. The maximum stresses are seen along the top and the bottom of the element. The top of the element is in compression and the bottom of the element is in tension because the element bends due to gravity. The minimum stresses were observed at the center of the fuel element, corresponding to the neutral axis shown in blue on the figure above. A maximum stress of 0.618 MPa was observed at the mid-plane, comparable to the analytical value of 0.650 MPa as calculated using equations B-11 to B-14. The overall stress distribution along the fuel element appears to be correctly modeled.

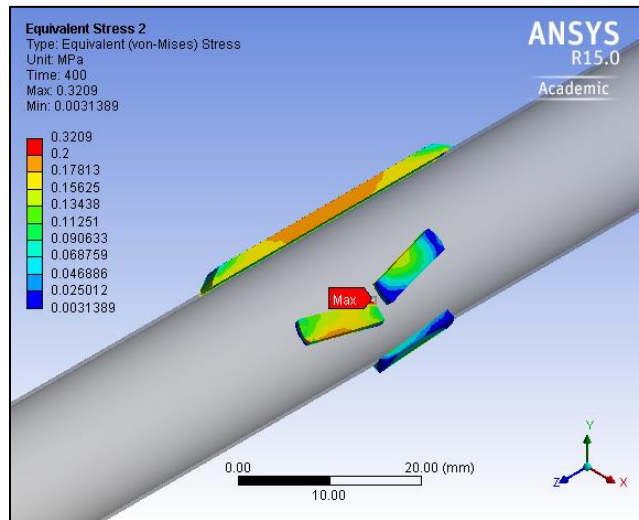


Figure 33: Equivalent Von-Mises stress [MPa] at the bearing pads.

The stress results at the bearing pads were also of interest and are shown in Figure 33. A Von-Mises stress of 0.321 MPa was seen at the spacer pad on the bottom of the element. Locally high stresses at the spacer pad on the bottom of the fuel element are reasonable. The current boundary conditions limit the deformation of the element by constraining nodes on the bottom edge of the upstream end in all directions and the downstream end in the X- and Y- directions. These constraints cause the weight of the element to effectively ‘rest’ on the bottom spacer pad and increase the sagging behaviour at this location. Furthermore, the applied thermal load causes thermal stresses at the interface of the spacer pad and the sheath, amplifying the extent of Equivalent von-Mises stress seen at the region.

Under off-normal conditions, the simulation demonstrates that the fuel element deforms axially, vertically, and diametrically. The deformation seen in the fuel element is a combination of thermal expansion, element sag, and creep deformation. A more coherent analysis concerning the accuracy and confidence of this model is discussed in Section 7.3.

7.3 Discussion

By assessing the deformation results, it is evident that thermal expansion is the dominant deformation mechanism under the loading conditions specified. The thermal load outpaces the gravitational and creep loads, as evinced through the axial elongation results. Although thermal bowing was not observed in the simulation due to the uniform temperature applied, the element expands in the radial and axial directions due to the increase in temperature to 1163.2 K from room temperature.

In the vertical direction, the magnitude of deflection is relatively small, which is consistent with the application of the gravitational and creep loads. The minor mid-plane deflection is related to the weight of the fuel element, approximately 0.0516 kg. The sagging behaviour of the fuel element was not prominent because the structure is relatively light and the only mechanical load acting on the element is gravity. While addition of the thermal load itself did not contribute to vertical deformation directly because the temperature was uniform, high-temperature creep deformation contributed to vertical deformation. While creep is an irreversible plastic strain, plastic deformation due to mechanical loading was not observed in the simulation because the material was not stressed beyond its yield strength.

7.3.1 Creep Deformation

The mechanical load applied in this simulation was gravity. Since this applied load does not change over the two load steps, the stress remains constant over time because it is defined as load distributed over an area. The stress results away from the spacer pads

and the boundary conditions were considered and are plotted in Figure 34. These results were taken at the bottom of the fuel element.

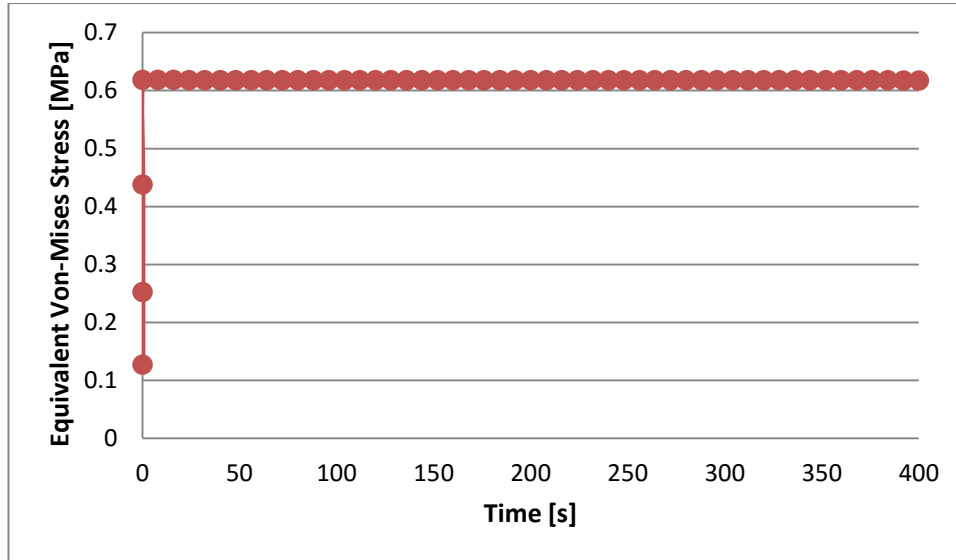


Figure 34: Equivalent Von-Mises stress [MPa] at the bottom of the fuel element as a function of time.

Once the initial stress state is established, the elastic strain will remain constant as long as the stress is constant. However, creep strain will accumulate over time in this simulation because the fuel element is free to deform. An increase in creep strain results in an increase in total strain, as it is the summation of the elastic, plastic and creep strain components. Although plastic deformation is separated from creep deformation in this work, creep is encompassed by plastic deformation, whereby deformation occurs above the yield stress of the material.

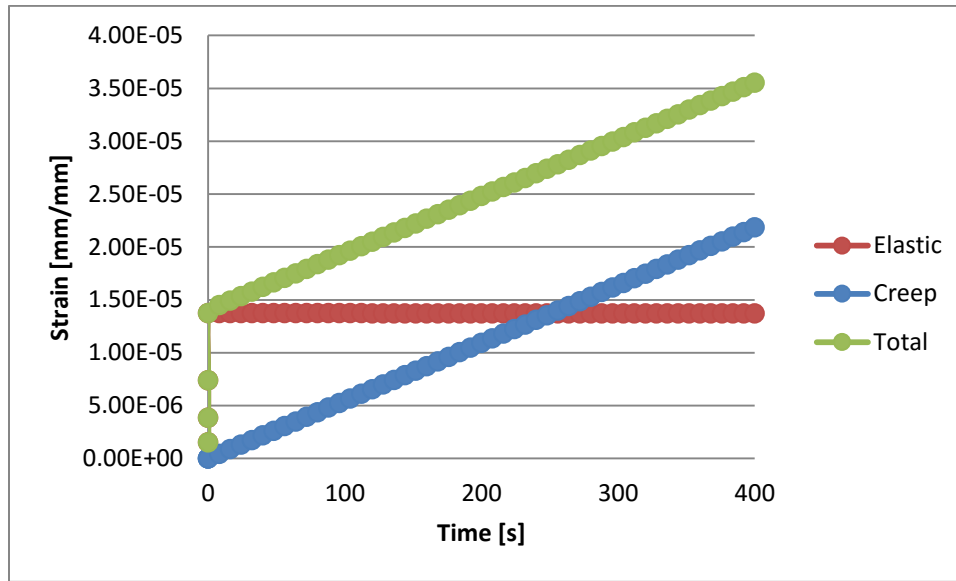


Figure 35: Strain as a function of time.

The strain behaviour for the simulation is shown in Figure 35; it represents a pure creep response because the creep and total strain accumulate over time with no increase in the stress. The creep strain behaviour is identical to the creep deformation preliminary model studied in Section 6.3.

This initial stress state is established in $1e-8$ s and the stress and elastic strain values remain constant for the remainder of the simulation. The total strain illustrated is the summation of elastic and creep strain since thermal strain was excluded for the purposes of this simulation. The relationship between creep strain and time is linear. This linear relationship is because the creep rate becomes constant overtime, equaling $\dot{\epsilon} = 4.30e-7 \text{ s}^{-1}$. The creep rate from equation 5.17 becomes constant because the applied stress values and the temperature remain constant through load step two.

7.3.2 Model Validation

The results of the nonlinear analysis suggest that the general deformation behaviour of the fuel element appears to be correctly modeled. The maximum vertical deflection was seen at the mid-plane. This was in agreement with the expected results of a simply supported structure with an applied gravitational force and a uniform thermal load. Furthermore, the magnitude of the diametric and axial expansion seen in the model appeared to be correct. However, it was necessary to compare the values obtained from the experiment against hand calculations.

To validate the model, the deformation results obtained from the ANSYS model were compared with analytical calculations. The results are summarized and compared in Table 7.

Table 7: Comparison of the Deformation Results of the Fuel Element Model with the Analytical Solution.

	ANSYS	ANALYTICAL	DIFFERENCE (%)
AXIAL DEFORMATION [MM]	2.809	2.799	0.357
DIAMETRIC EXPANSION [10^{-2} MM]	7.573	7.571	0.022

The axial deformation results from ANSYS were taken at the downstream end while the diametric expansion was obtained at the mid-plane. Sample analytical calculations are detailed in Appendix B, equations B-6 and B-7. The results obtained from the simulation show excellent agreement with the analytical results. Despite the fact that effects of material creep were included in the model, significant variance in the deformation values

was not seen between the analytical and simulation results. The lack of variance may be attributed to thermal expansion being the dominant mechanism that contributes towards axial and diametric deformation because the thermal load is greater in magnitude than the gravitational and creep loads. Comparing the calculated value with the value obtained from the fuel element model, it is evident that the values are sufficiently close to each other to conclude that the deformation values obtained from the simulation are realistic.

The results at the end of the two load steps were compared to provide insight into the contributions of the gravitational force, uniform thermal load and creep to the deformation behaviour of the fuel element. The comparison is summarized in Table 8.

Table 8: Comparison of deformation results between the two load steps.

	LOAD STEP ONE	LOAD STEP TWO	DIFFERENCE ACROSS THE LOAD STEPS (%)
VERTICAL DEFORMATION [10⁻¹ MM]	0.565	1.128	49.91
DIAMETRIC EXPANSION [10⁻² MM]	7.570	7.573	0.040
AXIAL DEFORMATION [MM]	2.805	2.809	0.142

The table indicates that creep deformation has minimal impact on diametric expansion. The observation suggests that the dominant mechanism contributing to diametric deformation is thermal expansion. Of the three applied loads, it is justifiable for thermal expansion to be the dominant mechanism over mechanical and creep loads. The stress induced due to the gravitational force of 0.5058 N distributed over the structure precludes a significant contribution to diametric deformation; the mechanical load is more

likely to contribute towards vertical deformation instead. Similarly, the creep load should not cause diametric creep for a light structure under the low stress of gravity for a short interval of 400 s. This is evinced through the comparison of the values at the two load steps for diametric deformation.

Neither gravity nor creep contributes significantly towards elongation in the axial direction. Gravity in the negative Y-direction would have no impact on axial deformation of a fuel element. Creep does not have a significant impact on axial elongation as illustrated by the lack of change in the results between the two load steps; however, the lack of axial creep seen in the simulation is likely due to the applied load being in the vertical direction only. As with diametric deformation, thermal expansion is the dominant mechanism for axial elongation.

The results indicate that vertical deformation of the fuel element occurs due to a combination of thermal expansion, sagging, and creep. In the first load step, the deformation is caused by thermal expansion and gravity. The result from the first load step is similar with the analytical result of 0.054 mm, detailed in B-15. Since the effects of thermal expansion and gravity are independent of time, the increase in vertical deformation beyond the first load step is solely due to high temperature creep. The deformation behaviour is consistent with the expected deformation of a simply supported structure subject to gravitational, thermal, and creep loads.

The successful benchmark of the deformation results of the fuel element indicates that the material data is being applied correctly to compute the deformation behaviour of the model. The validation serves to provide confidence in the ability of the model to predict

the deformation of the fuel element when the effects of thermal loading, gravity, and creep are modeled simultaneously.

7.4 Conclusion

In summary, a static structural analysis was conducted to characterize the high-temperature deformation behaviour of an empty fuel element. The deformation results obtained from the model were validated against analytical solutions to show confidence in the ability of the model to capture the simultaneous effects of thermal-mechanical loading and creep. The results illustrated that thermal expansion was the primary mechanism of deformation for the fuel element. The successful benchmark of the thermal-mechanical response of the fuel element allows for this model to be expanded to the fuel bundle model. It provides confidence in the combined behaviour of the fuel elements when they are assembled together in the configuration of a bundle where multiple contacts need to be considered.

8 Fuel Bundle Deformation Model

In the lead up to the development of the fuel bundle deformation model, the deformation behaviour of a single fuel sheath has been correctly modeled. For off-normal and accident conditions, the element model will now be extended to a bundle and compared to the empty bundle heat-up experiment described in Section 7. The objective of this model is to predict the geometrical deformation of the fuel elements as part of the fuel bundle and to model the contact between fuel elements correctly before adding the complication of fuel pellet-to-fuel sheath interaction.

8.1 Model Description

The assembly analyzed in this report is illustrated in Figure 36. A partial assembly was used in place of the full bundle as difficulties were observed while modeling 37 elements due to limited computational abilities. Twelve fuel elements, detailed in Section 6.1, were assembled together in the configuration of a third of a bundle. The elements were held in place by an end-plate on either end. This structure was then placed inside of a pressure tube. As with the element deformation model, the geometric configuration of the brazed appendages and the fuel sheaths corresponds to their alignment in a CANDU bundle. Given that the deformation results from this model are to be validated against the values obtained from the experiment, it is imperative for the bundle model to be constrained in a similar manner. In the experiment, the bundle was sitting on the bottom of the quartz tube and heated until the sheath temperature was above 1073 K. The high-temperature plateau lasted for 400 s of the experiment, between 2600 s and 3000 s of the total time of 4000 s. The bundle was allowed to expand axially and radially. In the

simulation, the upstream end-plate was fixed in all degrees of translation while the downstream end-plate was free to expand axially. Contact was defined between the bearing pads of the outer elements and the inner surface of the pressure tube to hold the bundle in place. These constraints ensured that the bundle could expand due to the loads applied and rigid body motion does not occur. The objective of the analysis is to observe the deformation behaviour of the fuel bundle at temperatures relating to transient conditions.

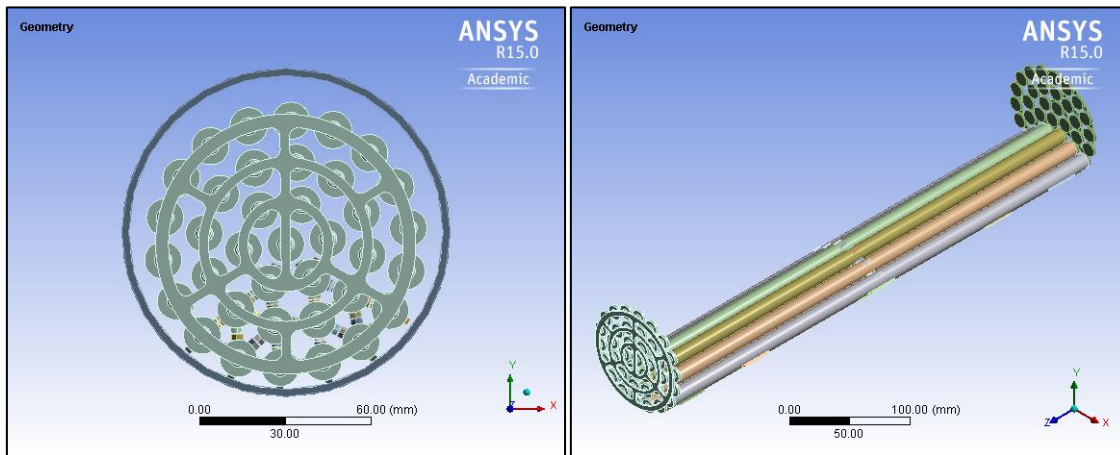


Figure 36: Image of the physical structure used in the fuel bundle deformation model.

Note: The pressure tube was hidden in the image on the right to show the bundle assembly.

8.1.1 Physical Geometry

In this simulation, the model under consideration was a 3-D shell-solid assembly composed of three components: 12 fuel elements with the brazed appendages, the end-plates with the welded end-caps, and the pressure tube. The geometry of the fuel elements used to compose the bundle correlated with the geometry used in the fuel element deformation model in Chapter 7. The end-plates and end-caps were added to the model to hold the elements in the configuration of a bundle. The bundle was 495 mm long and approximately 100 mm in diameter. The weight of the partial bundle is 0.872 kg. The

quartz pressure tube had a thickness of 2.5 mm and an inner diameter of 110 mm, corresponding with the inner diameter of a 5.6% crept pressure tube at end-of-life [17]. The pressure tube was defined to be slightly longer than the bundle with a gap of 5 mm at each of the upstream and downstream ends. These dimensions are consistent with those used in the experiment. The exact dimensions are shown in Figure 37.

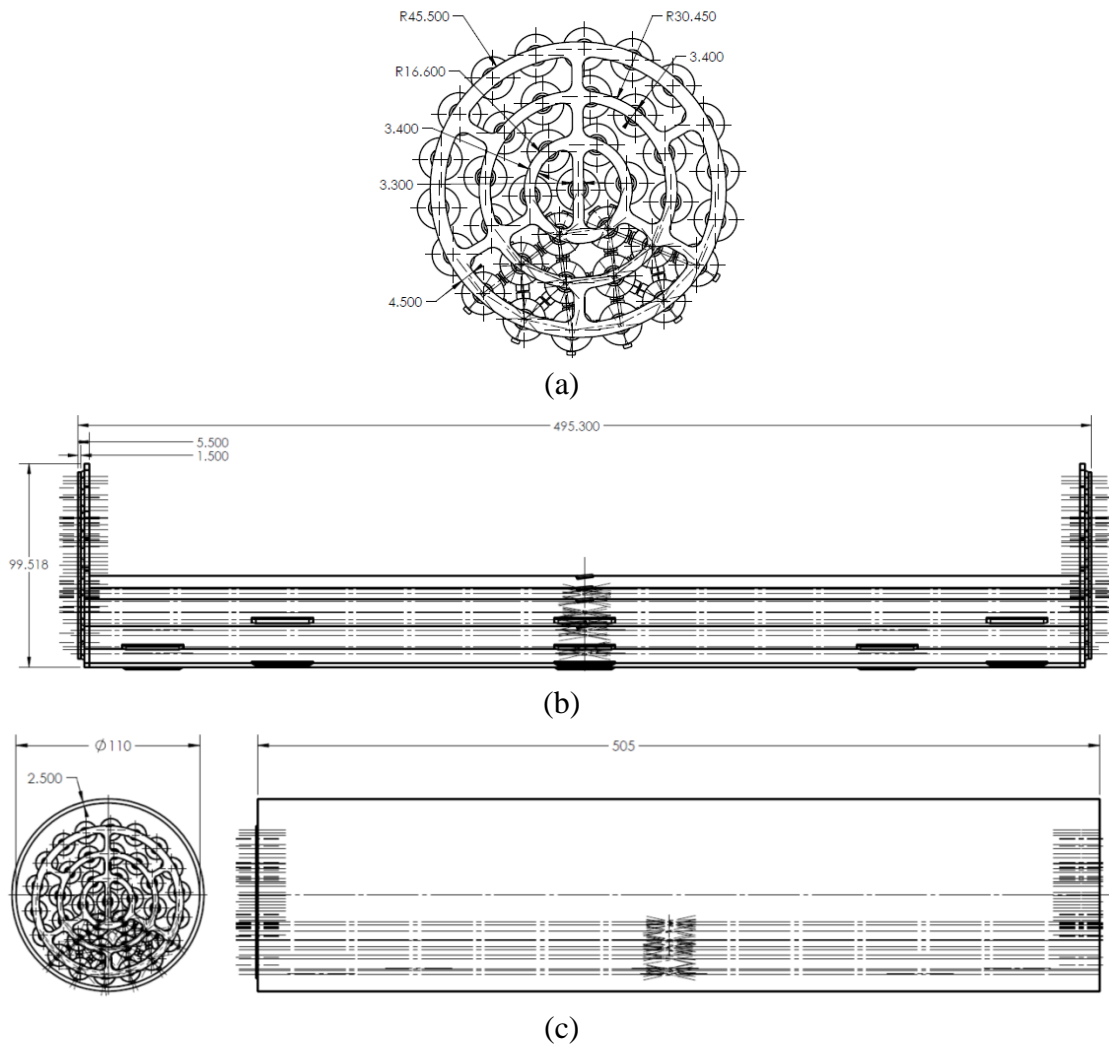


Figure 37: Dimensional drawings of (a) the end-plate, (b) the fuel bundle, and (c) the pressure tube. All measurements are given in mm.

8.1.2 Material Properties

In this assembly, the bundle is made from Zircaloy-4 and the pressure tube is made from fused quartz. The material property models used for Zircaloy-4 and fused quartz are described in Section 5.3.1 and 5.3.2 respectively. The quartz tube is assumed to maintain its shape and hence, acts as a supporting shell for the bundle.

8.1.3 Element Type and Mesh

The mesh in the preliminary analysis in Section 7.1.2 was used as reference point in constructing the mesh for the bundle model. The multiple cylindrical sheaths in the bundle were represented by higher order quadrilateral shell elements (SHELL281) with a thickness of 0.38 mm. The size of the mesh elements was defined to be 3 mm. While this decision served to reduce the mesh density, the mesh sizing of the sheath was increased from the fuel element deformation model to produce a mesh that would be sufficient in capturing the deformation behaviour of the fuel elements in the empty bundle without requiring a significant amount of time for computation. Similar to the element deformation model, a higher order sweep mesh, which resulted in uniformly-shaped hexahedral elements, was used for the bearing pads and spacer pads.

Given that the geometry of the end-plate could not be swept as it was and slicing it would prove unnecessarily complicated, higher order tetrahedral elements were used to represent the end-plates and the end-caps. Setting the global element size of the tetrahedral mesh to 3 mm yielded a mesh that had equilateral triangular shaped elements around the fillet edges of the end-plate. The resulting mesh contained 350,329 nodes and 117,607 elements. The mesh of the end-plate and the partial bundle is shown in Figure 38.

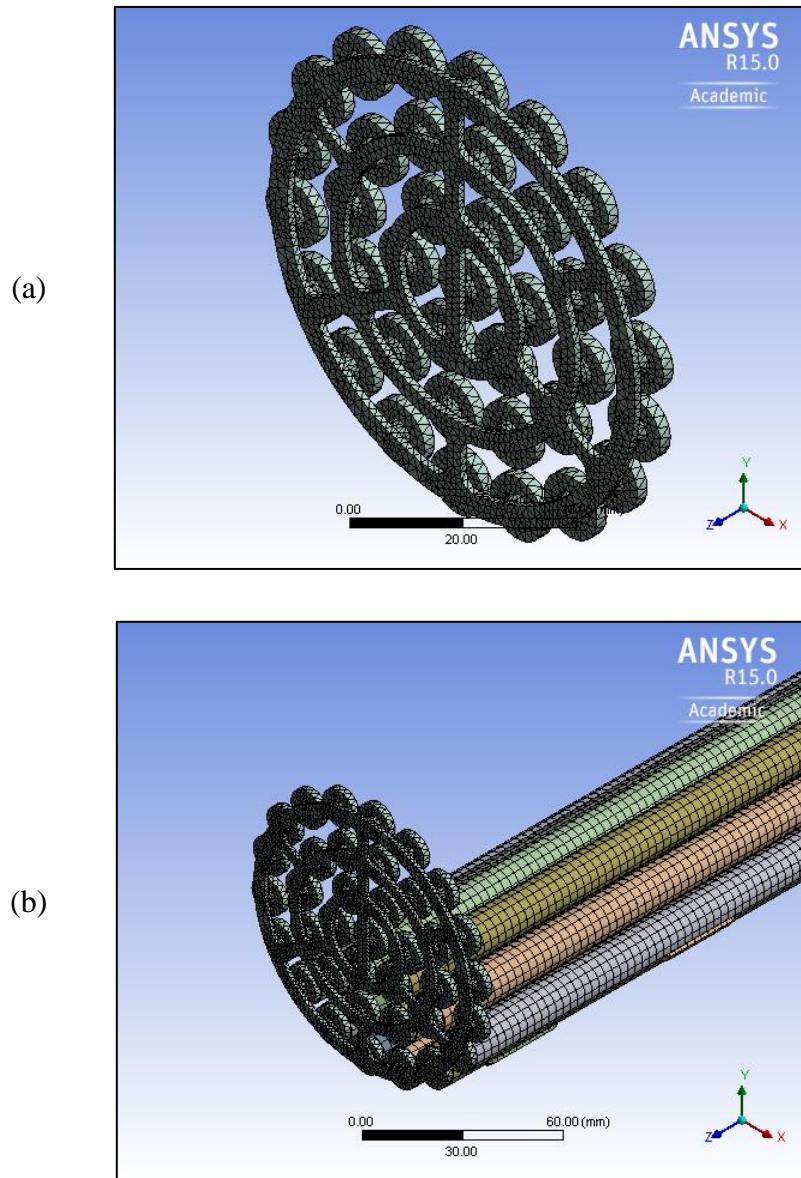


Figure 38: Mesh of the (a) end-plate and the end-caps; and (b) partial empty fuel bundle of 12 elements.

The shape of the shell and solid elements illustrates good element quality as seen in the figures above. Since the end-plates and fuel elements are defined separately, it was not necessary to account for the alignment between the solid element mesh of the end-plates and the shell element mesh of the fuel elements. However, it was imperative to define the

transition between the two regions as the elements and the end-plates connect to form a bundle. This transition region was achieved by defining bonded contact between the edges of the elements and the end-caps on the end-plates. The contact edge was defined to be the edge of the element and the target edge was defined to be the edge of the corresponding end-cap. The contact pair was defined in this manner because the contact edge and the target edge must be built on the shell element and solid element side respectively in a shell-solid assembly [23] [46]. A contact pair is shown in Figure 39.

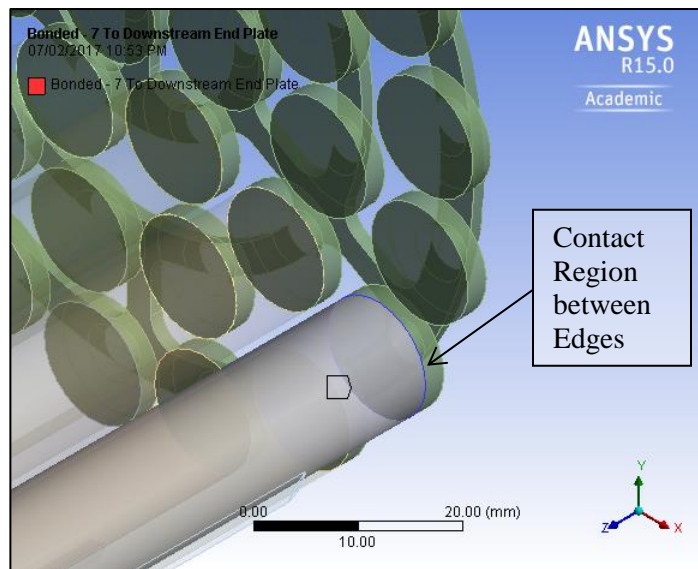


Figure 39: Bonded Contact between the edges of the element and end-cap.

It should be noted that bonded contact was also specified between the solid auxiliaries and the sheath as described in Section 7.1.4.

The fused quartz tube was represented by higher order solid elements. The element size of the quartz tube mesh was defined to be 10 mm. The mesh is shown in Figure 40.

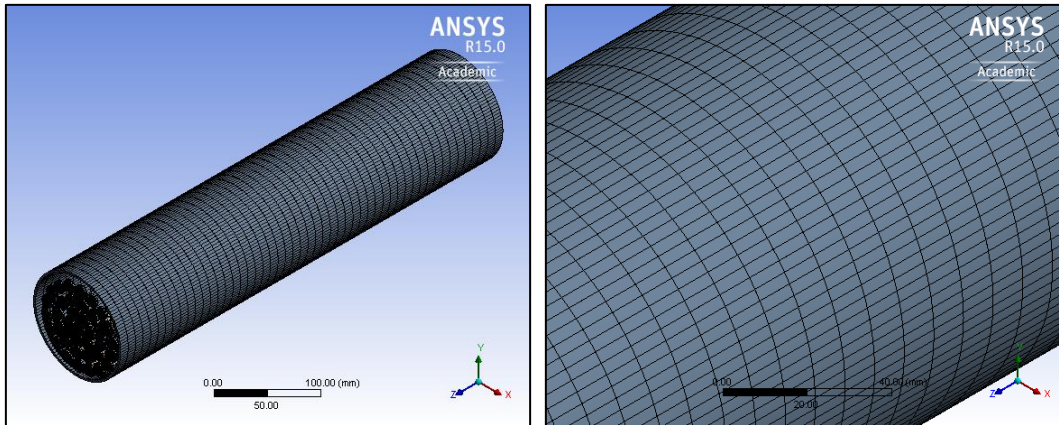


Figure 40: Higher order quadrilateral mesh of the quartz tube

Since the quartz tube will be represented as a non-deforming component in the simulation, the relatively coarse mesh of the tube was acceptable.

8.1.4 Loading and Boundary Conditions

8.1.4.1 Contact Modeling

As the aim of the model is to simulate the fuel bundle heat-up experiment, structural assumptions were made about how the experimental system was arranged physically. In the experiment, the bundle assembly was resting on the bearing pads of elements 9 and 10 in the pressure tube. The numbering convention for the elements is shown in Figure 41.

It was also expected that the bearing pads of element 11 could come into contact with the pressure tube at high temperatures. These structural assumptions were implemented in ANSYS using the available contact definitions. Since the partial bundle assembly and the pressure tube are represented as two separate parts in the simulation, it was necessary to specify contact between the bearing pads of the bundle and the pressure tube.

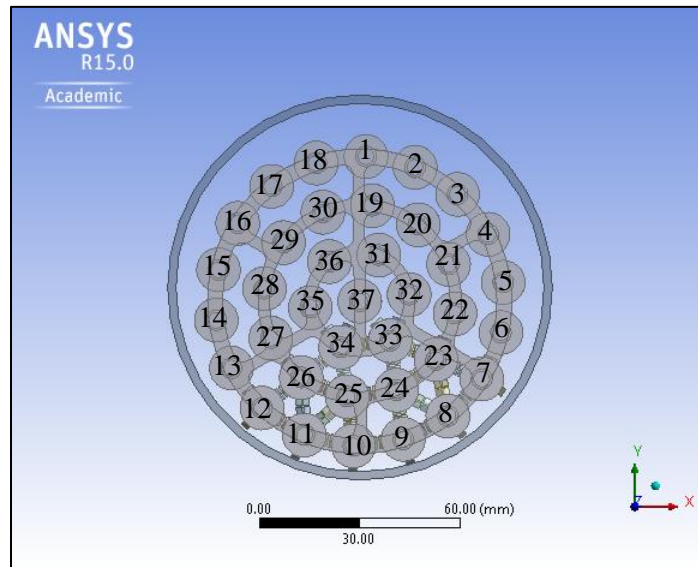


Figure 41: Numbering convention of the fuel bundle.

The contact surface was defined to be the outer surface of the bearing pads and the target surface was defined to be the inner surface of the quartz tube. A ‘no separation’ contact mechanism was used to specify the contact between the bearing pads of elements 9 and 10, and the pressure tube. This contact definition meant that the bearing pads of the two bottom outer elements and the pressure tube remain in contact throughout all loading steps while allowing for relative sliding. Should the loading be removed, the outer faces of the bearing pads will still be in contact with the pressure tube. This boundary condition ensures that the model is consistent with the experiment.

The behaviour between the bearing pads of element 11 and the pressure tube is slightly different as these two surfaces are not in contact initially. There is a gap of approximately 0.1191 mm (see Appendix C), which is expected to close due to the applied thermal loading for a full fuel bundle. To simulate this behaviour, the contact definition was selected to be frictionless because this contact type allows for the two structures to come in to and out of

contact with one another as the loading changes. While the assumption that the contact status changes with the loading is valid, the structural assumption that this behaviour is frictionless is not; the behaviour should be frictional [57]. However, there is very limited data on the frictional coefficient between Zircaloy-4 and fused quartz. Due to this limitation, the decision to use frictionless contact was made and it was assumed that shear forces between the two structures did not impact the amount of displacement along the axial direction.

At temperatures related to transient and off-normal conditions, the fuel elements may apply mechanical loads to each other directly through contact between spacer pads and indirectly through weld contact at the endplates. As these applied loads affect the deformation of the bundle, contact was specified between the spacer pads of the adjacent fuel elements as their interaction affects the geometry of the sub-channel. While the contact between empty fuel elements was not observed in the experiment, it is included in the simulation for the purposes of being comprehensive in case the simulation results diverge from the experiment. Moreover, defining contact between adjacent fuel elements establishes a foundation for the addition of fuel pellets at a later date.

At the spacer pads between neighboring elements, there is a gap of approximately 0.452 mm. This gap is expected to open and close due to the applied thermal-mechanical loads. Therefore, the contact definition for adjacent elements was selected to be frictional. Frictional contact allows structures to come in to and out of contact with one another due to changes in applied loading. The contact between the spacer pads of neighboring fuel

elements was modelled using a total of 20 contact pairs. A contact pair is illustrated in Figure 42 .

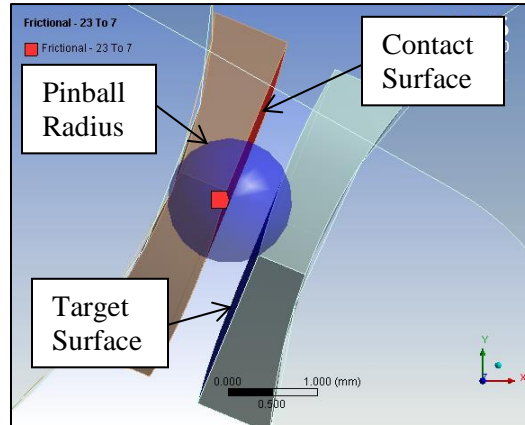


Figure 42: Contact between the spacer pads of adjacent elements. The contact surfaces (red) were represented by CONTA174 elements while target surfaces (blue) were represented by TARGE170 elements.

The coefficient of friction between the spacer pads of adjacent elements was set to 0.1 which was consistent with the value used in literature [53, 58]. The Augmented Lagrange formulation was selected to be the contact algorithm. It produces the most accurate results of all available methods and can handle large sliding across the contact surfaces. A maximum penetration tolerance of 0.1 mm was specified. This was defined because a small amount of penetration is needed for the contact force to be generated as mentioned earlier in Section 5.1.2. The pinball radius was set to be 0.7 mm in order to cover the gap between the two surfaces. Defining a large pinball radius ensures that the bearing pads of the adjacent fuel elements can be recognized such that initial contact may be detected as a result of the loading conditions applied. An interface treatment had to be applied so that initial gap would be recognized by ANSYS. Using an offset of 0 mm, the ‘Add Offset, No Ramping’ interface treatment was applied to establish the gap between

adjacent elements. It was added to achieve convergence. This technique ensured that initial contact would be established if the spacer pads were to come in to contact due to the applied loading.

A prototype model was developed to test the modeling technique used to simulate frictional element-to-element contact between spacer pads of neighboring fuel elements. The assembly was simplified to a section of two adjacent fuel elements, aligned as they would be in a 37-element CANDU fuel bundle. The assembly is shown in Figure 43.

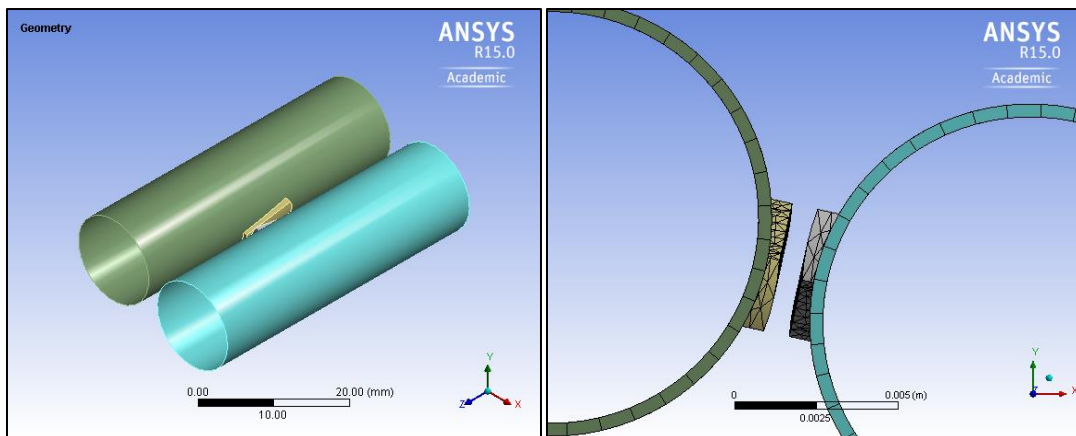


Figure 43: Entire assembly and cross-section of the geometry of two adjacent fuel elements.

The model was constrained as a simply supported structure and included the effects of gravity and material creep. As per design, the initial gap of 0.635 mm between the fuel elements is kept open to allow adjacent elements to initiate contact at the spacer pads. Using the settings specified above, frictional contact was specified between the spacer pads of the adjacent fuel elements. To test the effectiveness of the contact definition, a force of 9000 N was applied to the surface of the left fuel element in order to bring its spacer pad

into contact with spacer pad of the right fuel element. An interface treatment with an offset of 0 mm and no ramping effects was applied to this model as well.

The results of this analysis indicate that the two fuel elements come into contact with one another at the spacer pads when force, sufficient to close the gap, is applied. As illustrated in Figure 44, the fuel element on the right generates a force reaction in response to the applied force as indicated by the arrow. This is encouraging as it shows that the load is being transferred across the contact region and provides justification for the modeling technique used.

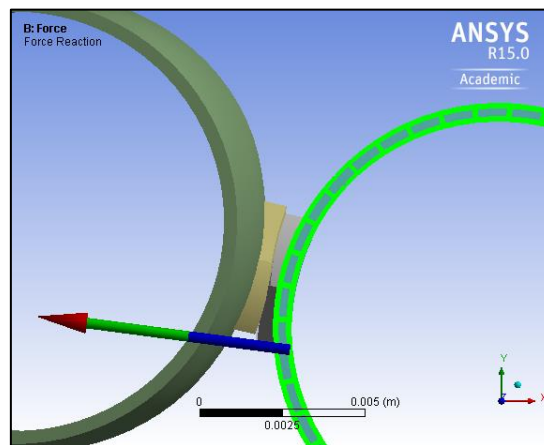


Figure 44: Reaction of the element on the right in response to applied load.

8.1.4.2 Temperature Distribution

Data from the sheath thermocouples, as well as from the surrounding gas thermocouples interspersed through the bundle, was used to create the temperature distribution required by the ANSYS model. An uncoupled static structural analysis was conducted instead of a fully coupled thermal-mechanical simulation because the sheath temperatures from the experiment were mapped such that a thermal load could be created.

Though the data spanned the entirety of the experiment, data of interest for this simulation corresponded to sheath temperatures of at least 1073 K. The high-temperature plateau range spanned 400 s in the experiment. The data from the thermocouples, which were instrumented throughout the bundle, was averaged over this range to obtain the input thermal load for the simulation. The temperature gradient from the test assembly during the high-temperature plateau at time 2789 s is shown in Figure 45.

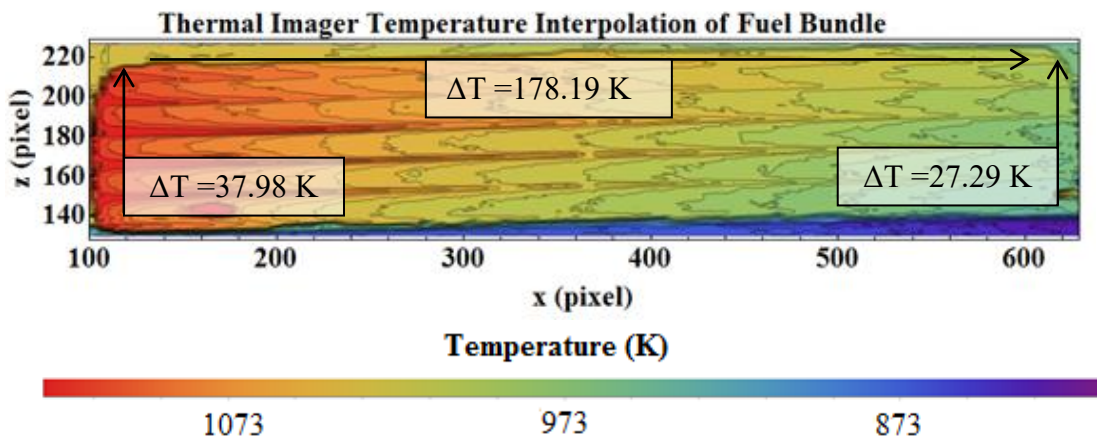


Figure 45: Variable temperature load from the experiment. Reproduced from [17].

Note: The upstream end of the bundle is on the left and the downstream end is on the right. The arrows point from the hotter end to the colder end.

At the upstream end, the sheath temperature difference in the vertical direction was approximately 37.98 K. In this region, the bottom of the bundle exhibited a maximum temperature of 1135.6 K. The axial temperature difference was 178.19 K between the upstream and downstream ends of element 7. This is consistent with the temperature differences of up to 195 K measured by the thermocouples inside the bundle during the experiment [17]. The downstream end exhibited a vertical temperature difference of 27.29

K. The surrounding temperature of the environment was specified to be 1028 K in accordance with the experiment. The temperature distribution is illustrated in Figure 46.

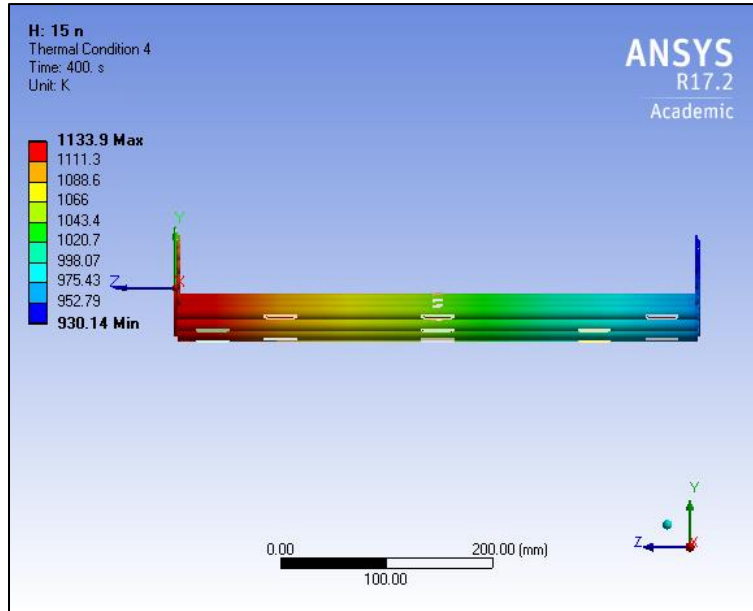


Figure 46: Temperature distribution of the partial bundle in ANSYS in [K].

The temperature gradients detailed above and the averaged data from the thermocouples was input into ANSYS to recreate the axial and top-to-bottom temperature distribution seen in the experiment. Using the temperature gradients from the experiment to calculate the mechanical response of the fuel bundle ensured that the bundle deformation model could be validated against the experimental deformation data.

8.1.4.3 Boundary Conditions

In an effort to maintain consistency with the experiment, the partial bundle was constrained as a simply supported structure. At the upstream end of the bundle, nodes on the bottom edge of the endplate were constrained from rotations and translations in all directions by specifying fixed support. This constraint allows the end-plate to rotate

inwards under the application of a mechanical load. Instead of stipulating displacement constraints at the downstream end, the structure was constrained through the contact between the bearing pads of elements 9 and 10 and the pressure tube. The ‘no separation’ contact definition allows for movement in the axial direction while preventing the bundle from rotating and moving in global X and Y direction.

The temperature distribution detailed in Section 8.1.4.2 was applied to the structure. Gravitational force in the negative Y-direction was applied in accordance with the experiment. The effects of material creep were also included as described in Section 5.3.1.6. All faces of the pressure tube were fixed to ensure that the quartz tube was modeled as a non-deforming structure. A graphical representation of the boundary conditions is illustrated in Figure 47.

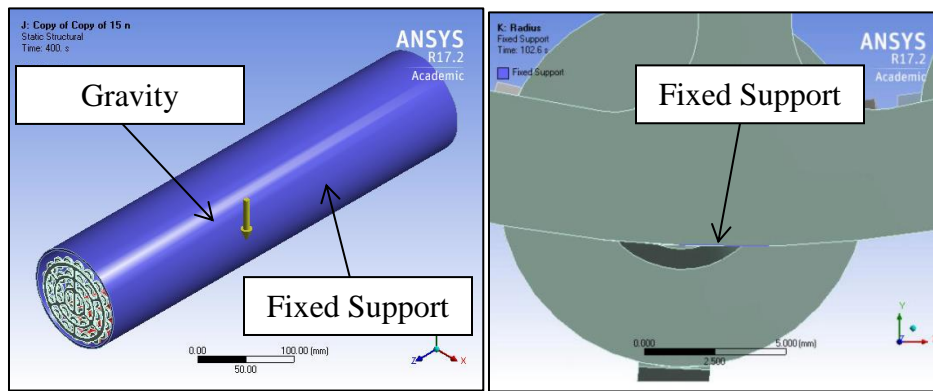


Figure 47: Loading and boundary conditions of the assembly.

Similar to the fuel element deformation model, it was necessary to split the loading into two load steps to model the effects of material creep:

1. Load Step One: The boundary conditions were applied for the upstream end-plate and the pressure tube. The effects of gravity were turned on. Moreover, the detailed

temperature distribution was applied to the structure. An end time value of $1e-8$ s was set for this load step to establish the initial stress state.

2. Load Step Two: While the other loading and boundary conditions remained constant, the effects of material creep were turned on during the second load step. The end time for load step two was defined to be 400 s. The creep strain ratio was limited to 1.

8.1.5 Solution

The solution was conducted with the assumption that relatively large deflections would not occur under the conditions specified. The analysis was non-linear due to contact at the spacer pads and the inclusion of material creep. The settings were adjusted such that auto time stepping was turned on during the second load step and the model was conducted with 100 initial sub-steps. A minimum of 100 sub-steps to a maximum of 1000 sub-steps were specified.

8.2 Results

A nonlinear contact analysis was conducted using the parameters and settings detailed above. The results indicated that the applied thermal distribution resulted in a maximum axial deformation of 2.495 mm. A graphical representation of this result is shown in Figure 48.

Under the applied temperature conditions, the finite element model of the partial bundle displays fuel element elongation. The elongation of 2.495 mm observed in the partial bundle model is less than the 2.800 mm seen in the single fuel element deformation model.

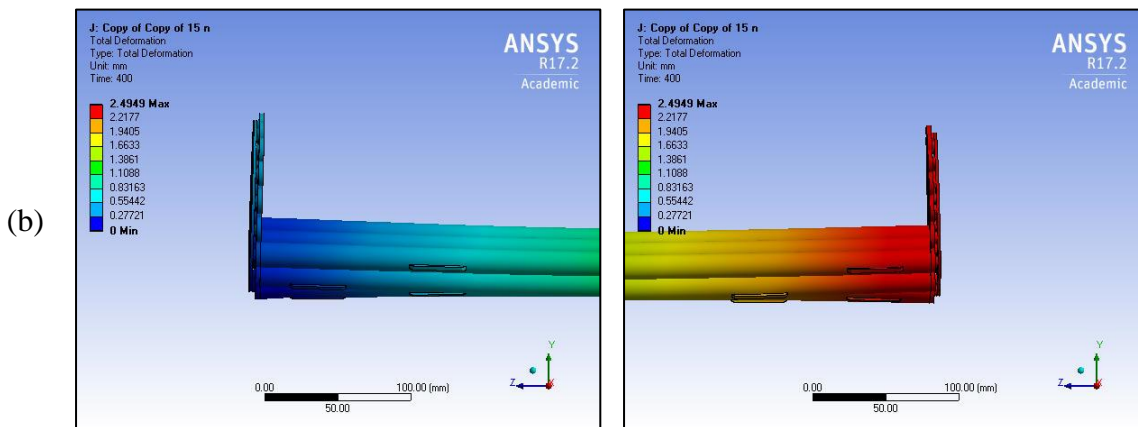
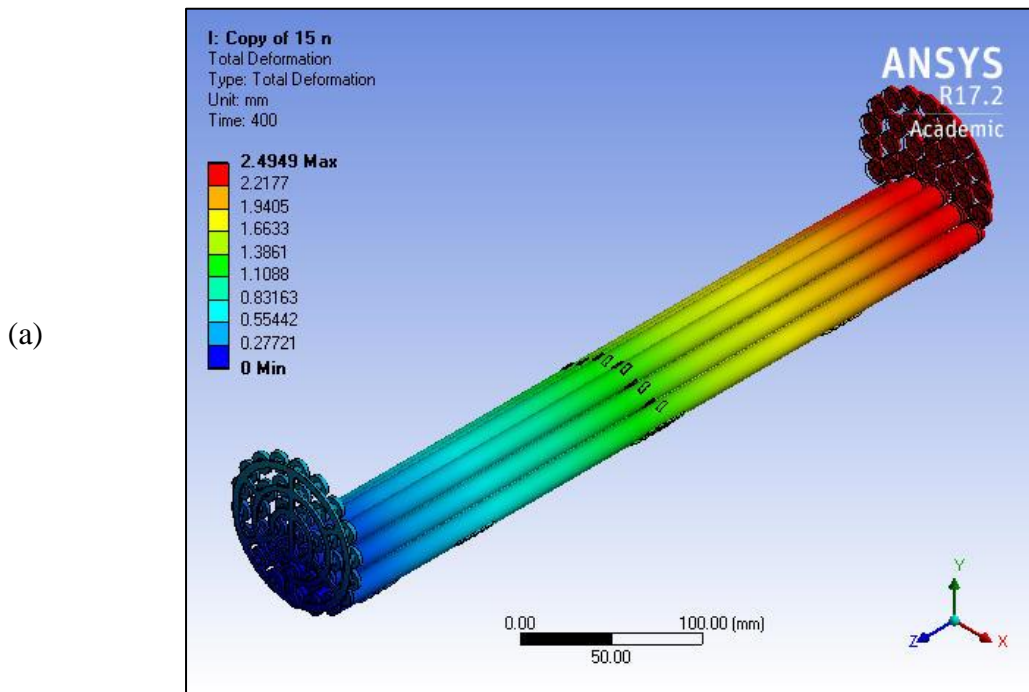


Figure 48: Images illustrating the (a) axial deformation of the partial bundle, and (b) deformation behaviour of the upstream (left) and downstream (right) end-plates.

Note: The images shown in 49 (b) were magnified by a factor of 21 to accentuate end-plate deformation behaviour. The non-deforming pressure tube was hidden in order to show the deformation of the partial bundle.

The axial elongation is of a lower magnitude for the partial bundle model for three reasons: the peak temperature applied to the bundle is 1135.6 K compared to the 1163.2 K applied to the single element, the thermal gradient applied causes differential thermal expansion of the bundle, and deformation in the axial direction is limited by the stiffness of the end-plates. The differential thermal expansion due to the temperature gradients along the length and the diameter of the bundle cause some elements to elongate more than others; however, since the elements are held together by the end-plates, the lengthening of the elements is limited by the element with the lowest temperature gradient. In response to the differential expansion, the top of the end-plates deflects inwards in the axial direction by 0.085 mm and 0.089 mm for the upstream and downstream end-plates respectively. The small axial droop is consistent with expected results wherein the end-plate axial deformation restricts the elongation of the fuel elements and contributes to the overall geometric deformation of the bundle [58].

While vertical translations of the structure were restrained by the contact definition between the bearing pads and the pressure tube, the applied thermal-mechanical load caused the structure to deflect vertically. The deflection is caused by two competing mechanisms: element sag and bundle droop [59]. Element sag occurs due to gravity and results in the fuel elements bowing downwards. This mechanism dominates the vertical deformation behaviour of all simulated elements other than elements 9 and 10. The results are illustrated in Figure 49.

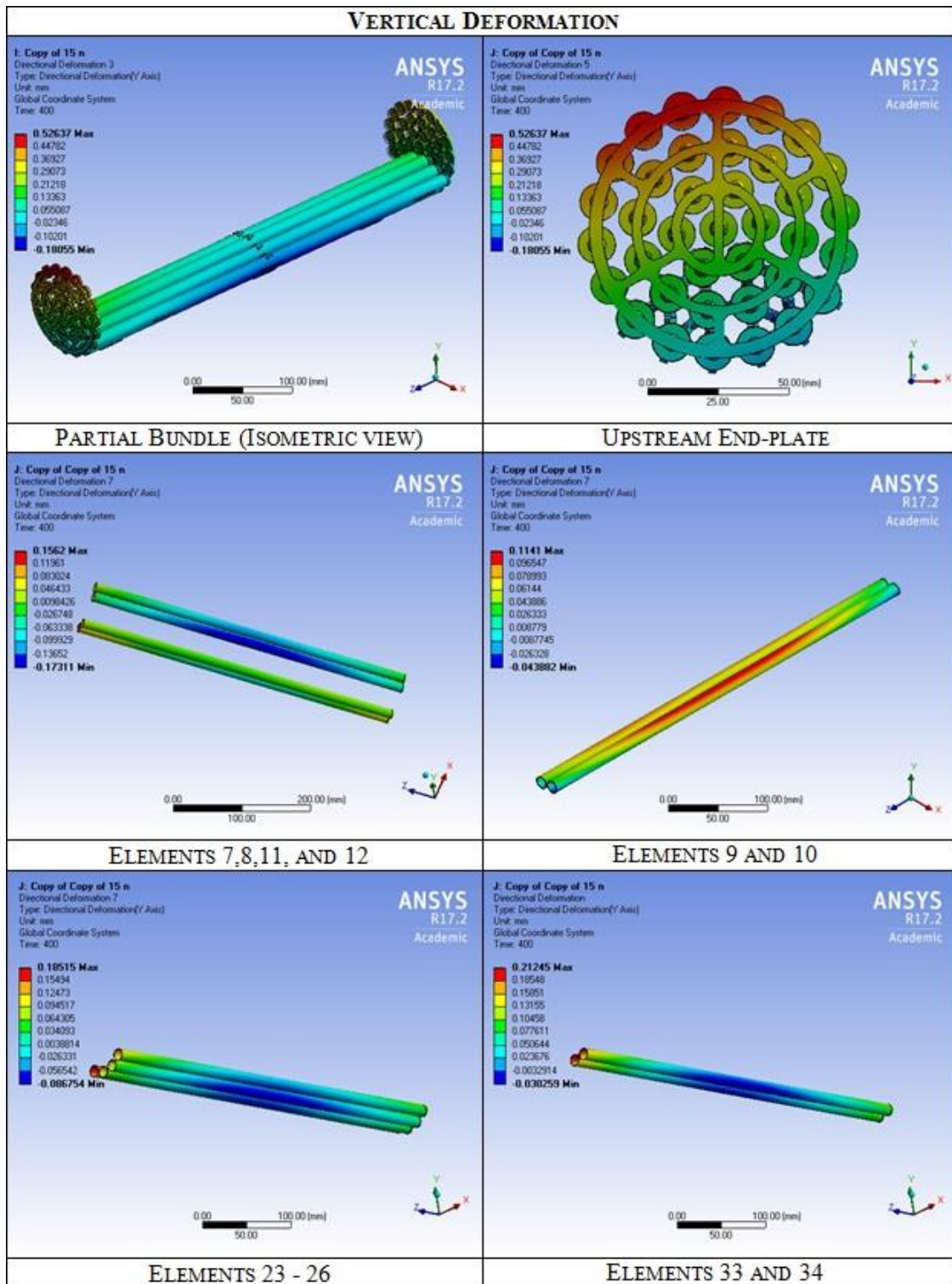


Figure 49: Vertical deformation of the partial bundle [mm].

As a general trend, the partial bundle sagged more near the upstream end, which can be attributed to the relatively higher temperatures. The maximum vertical deflection of 0.16 mm occurs at the mid-plane of element 8. The maximum vertical deflection upwards was observed at the top of the upstream end-plate. This was expected given that the lower end of the upstream end-plate was constrained while the remainder of the bundle was allowed to expand under the thermal gradient.

The sagging behaviour of the bottom elements (#9, 10) in contact with the pressure tube is countered by the droop induced in the bundle. Bundle droop occurs when the weight of the fuel elements not in contact with the pressure tube is transferred to the bottom elements via the end-plates [60]. The mechanical load of the elements is applied to the ends of the fuel elements and rests across the bearing pads, which are in contact with the pressure tube. Thus, the bottom fuel elements act as a cantilever beam and the load causes the elements to bend upwards at the mid-plane and downwards at the ends. This behaviour was evident in elements 9 and 10, which remained in contact with the pressure tube through their bearing pads over the course of the simulation. The upwards vertical deformation of the two elements is illustrated above. The ability of the model to capture bundle droop is a significant result.

The applied thermal and mechanical conditions also caused lateral deformation in the partial bundle assembly due to differential thermal expansion. The deformation profile illustrated in Figure 50 shows that the lateral deformation was asymmetrical and greater on the right-hand side. The maximum lateral deformation in the positive X-direction occurred near the upstream end while the maximum deformation in the negative X-

direction occurred near the downstream end. It can be seen that the upstream end-plate deformed outwards to a greater extent in the lateral direction than the downstream end-plate. This behaviour is a result of the applied non-uniform thermal gradient, which was hotter at the upstream end.

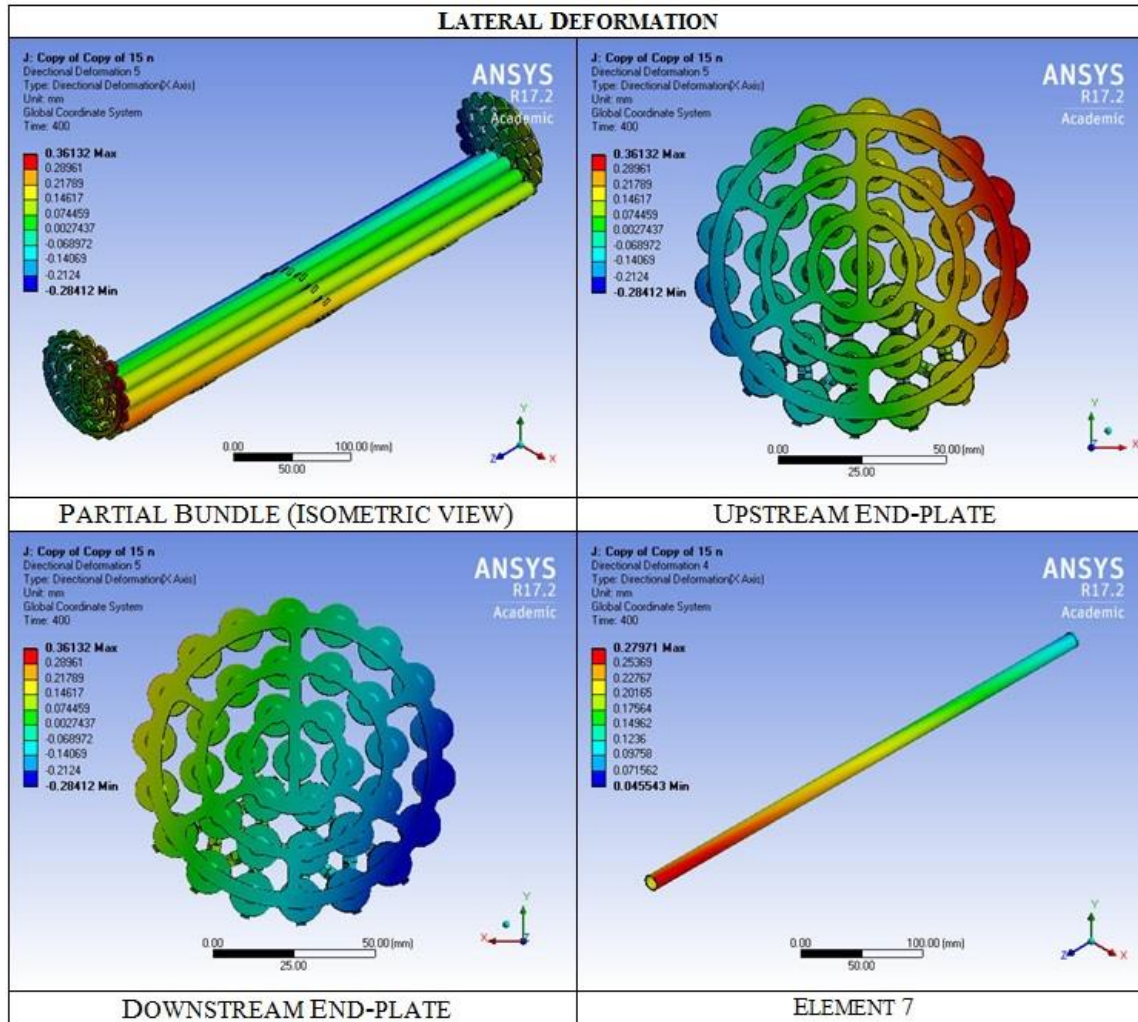


Figure 50: Lateral deformation of the partial bundle [mm].

As seen from the behaviour of element 7, the deformation in the lateral direction depended on the location along the bundle. This location dependence is correlated with the

significant temperature differences between the hotter upstream end and the relatively cooler downstream end.

The stress distribution profile of the assembly resulting from the application of the gravitational load, thermal load, and material creep is illustrated in Figure 51 .

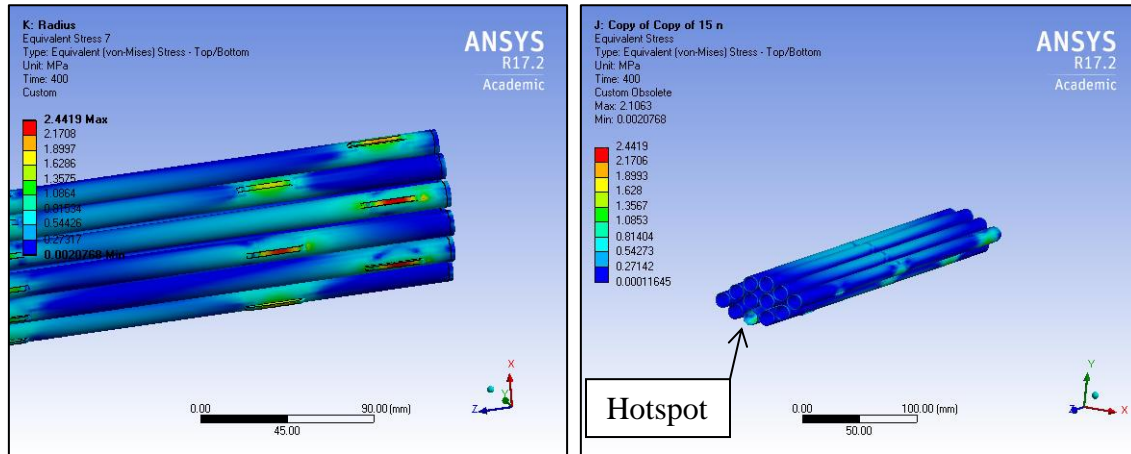


Figure 51: Equivalent Von-Mises stress [MPa] of the bearing pads (left) and the partial bundle without the end-plates (right).

The maximum Equivalent Von-Mises stress of 2.44 MPa was seen at the surfaces of the bearing pads in contact with the pressure tube. High stresses in this region are expected as the combined weight of the entire bundle is resting on the bearing pads of elements 9 and 10. In addition to the mechanical load, the applied thermal load causes thermal stresses at the interface between the bearing pads and the pressure tube. The stresses are a result of the sliding of the bearing pads against the pressure tube as the bundle elongates under a thermal load. Therefore, it is logical for the region of highest stress to be located along the bearing pads.

The stresses observed at the upstream end-plate were not realistic. This is because nodes on the end-plate were constrained in all directions, instead of being constrained

exclusively through contact between the bearing pads and the pressure tube. With the exclusion of the end-plates, stresses induced due to gravity and the thermal load could be seen on the surface of the elements, away from locations where constraints had been specified.

Under off-normal conditions, the simulation shows that the partial bundle undergoes fuel element elongation, vertical deformation, and lateral displacement. These contribute to the overall geometric deformation of the bundle. A more comprehensive analysis concerning the validity of this model is discussed in Section 8.3.

8.3 Discussion

Analyzing the deformation results demonstrated that the thermal-mechanical behaviour of the fuel elements in the configuration of a bundle was more complex than that of a single simply-supported fuel element as modeled in Chapter 7. The vertical and lateral deformations observed along the axial direction of the fuel elements were dissimilar from one another. For instance, the vertical deflection of elements 9 and 10 was in the direction opposite to the other elements. A strong dependence on the axial location was observed for both lateral and vertical deformations. This dependence is due to the axial temperature gradient that was applied to the bundle. The variance in the behaviour of the fuel elements and along their length illustrates that some of the deformation is caused by the thermal and plastic strains induced.

Unlike the results for a single fuel element, the maximum deflection in the vertical direction was not obtained at the axial mid-plane between the two end-plates. This result is realistic because the fuel elements are behaving as part of a complex model and

deforming due to the significant interaction with one another in addition to the non-uniform thermal load applied. In comparison to the upstream end, the bundle sagged less at the downstream end. This tendency is likely due to the relatively cooler temperatures at the downstream end. In terms of lateral deformation, the elements on the right hand side deformed more than the elements on the left side. The asymmetrical trend in lateral deformation illustrated that the deformation was greater on the side where the bundle was less supported as the elements are not positioned symmetrically.

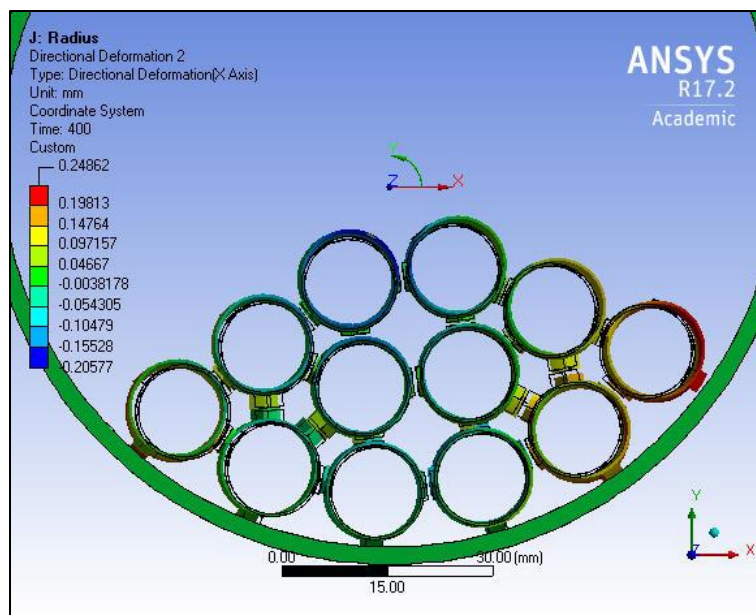


Figure 52: Radial bow of the partial assembly.

Note: The original wireframe is shown and the results are magnified by a factor of 3 to accentuate the magnitude and behaviour of the outer fuel elements. The elements did not contact the pressure tube.

The simulated deformation profile of the partial bundle is shown in Figure 52. Under the applied thermal-mechanical conditions, the elements in the inner rings bend downwards (in the Y-axis) due to element sag as expected. A small amount of bow outwards (in the X-axis) was also observed in the inner elements. The inner elements bow

outwards to a lesser extent in comparison to outer elements 7 and 12. The trend exhibited by elements 8 and 12 demonstrates that they may bow outwards and downwards to the extent that contact would be established with the pressure tube at their bearing pads. This is consistent with trends noted by Yu et al, as shown in Figure 53.

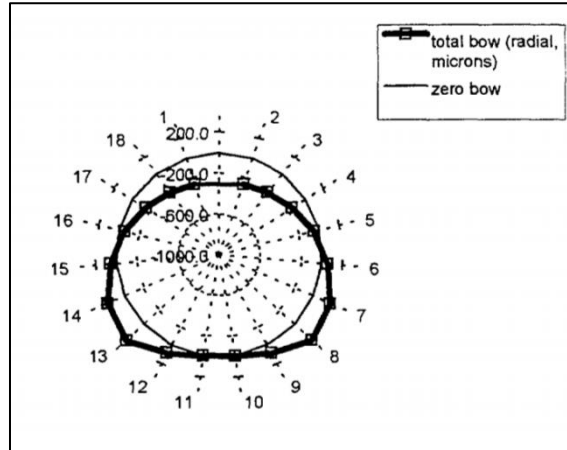


Figure 53: Predicted radial bow of outer elements. Reproduced from [59].

The bearing pads of the outer elements do not come into contact with the pressure tube in the simulation. This is consistent with the results of the empty bundle heat-up experiment. The bundle was initially in contact with the inside surface of quartz tube because it was resting on the bearing pads of fuel elements 9 and 10. Contact was not observed at the bearing pads of any other elements; this observation seems valid because the empty bundle is only deforming under gravity at a high temperature for a relatively short time interval of 400 s.

8.3.1 Creep Deformation

The stress results for the fuel elements in the bundle were considered because the stress results near the boundary conditions were unrealistic. Due to high-temperature creep,

the stress generated in the model does not remain constant as shown in Figure 54. The stress decreases with decreasing elastic strain over the time interval specified in the simulation. Stress relaxation occurs because the end-plates are preventing elongation, as stated above. Some elements would lengthen more than others because of the applied non-uniform thermal load; however, the end-plates limit the elongation to the element with the lowest temperature gradient. This limitation indicates the model is simulating creep as a ‘fixed displacement’ case, as opposed to the ‘fixed force’ case investigated in Section 6.3.

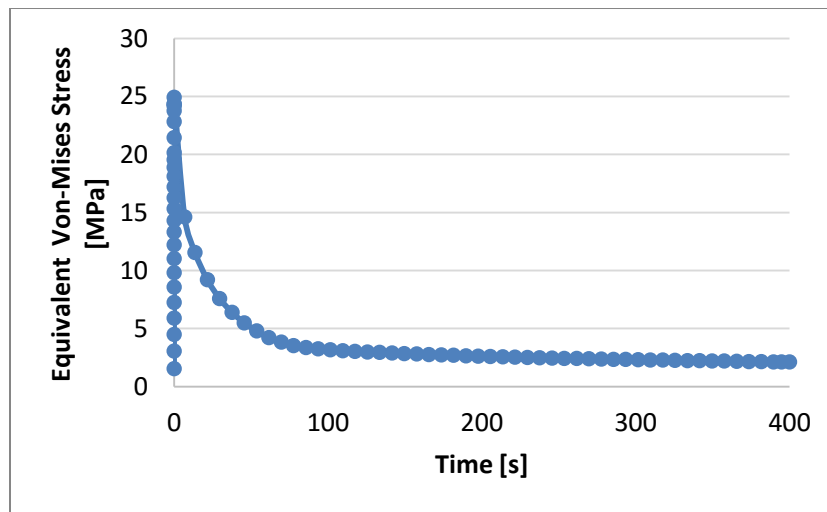


Figure 54: Equivalent Von-Mises stress at the downstream end of the fuel element as a function of time.

To verify that the simulation was mimicking a stress relaxation response, the strain behaviour over time was considered in Figure 55. As elastic strain is directly related to stress, a decrease in stress results in a decrease in elastic strain. The decrease in elastic strain correlates to a corresponding increase in creep strain.

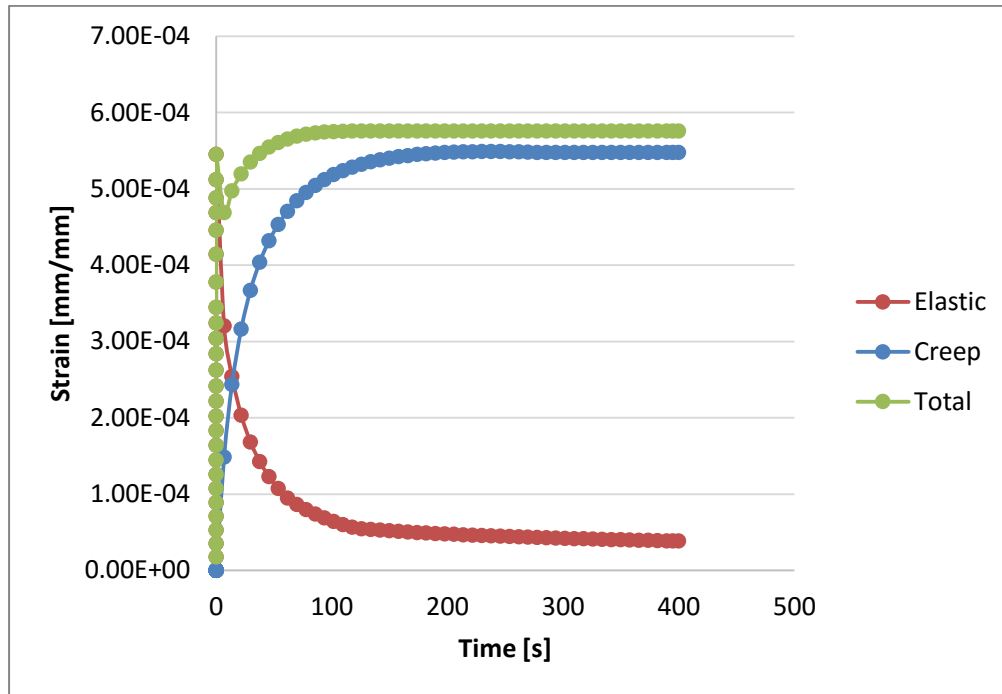


Figure 55: Strain as a function of time.

The correlation exists in ‘fixed displacement’ creep cases because the total strain must remain constant over time. However, there is an increase in total strain with accumulating creep strain because this finite element analysis is more complex than a uniaxial ‘fixed displacement’ case. The total strain behaviour illustrated in the figure above is reasonable because the elements are allowed to deform to an extent in this simulation. Therefore, the increase in total strain and decrease in stress observed in the simulation results makes sense.

In order to gain an appreciation of the creep-induced deformation of the bundle, the gaps between adjacent elements were analyzed as a function of time. The results for the lateral gap between elements 8 and 9, and the vertical gap between elements 9 and 24 are illustrated in Figure 56. The figure demonstrates that the bundle slumps downwards due to

high-temperature creep deformation of the fuel elements and the end-plates. This behaviour is consistent with expected results from literature [61].

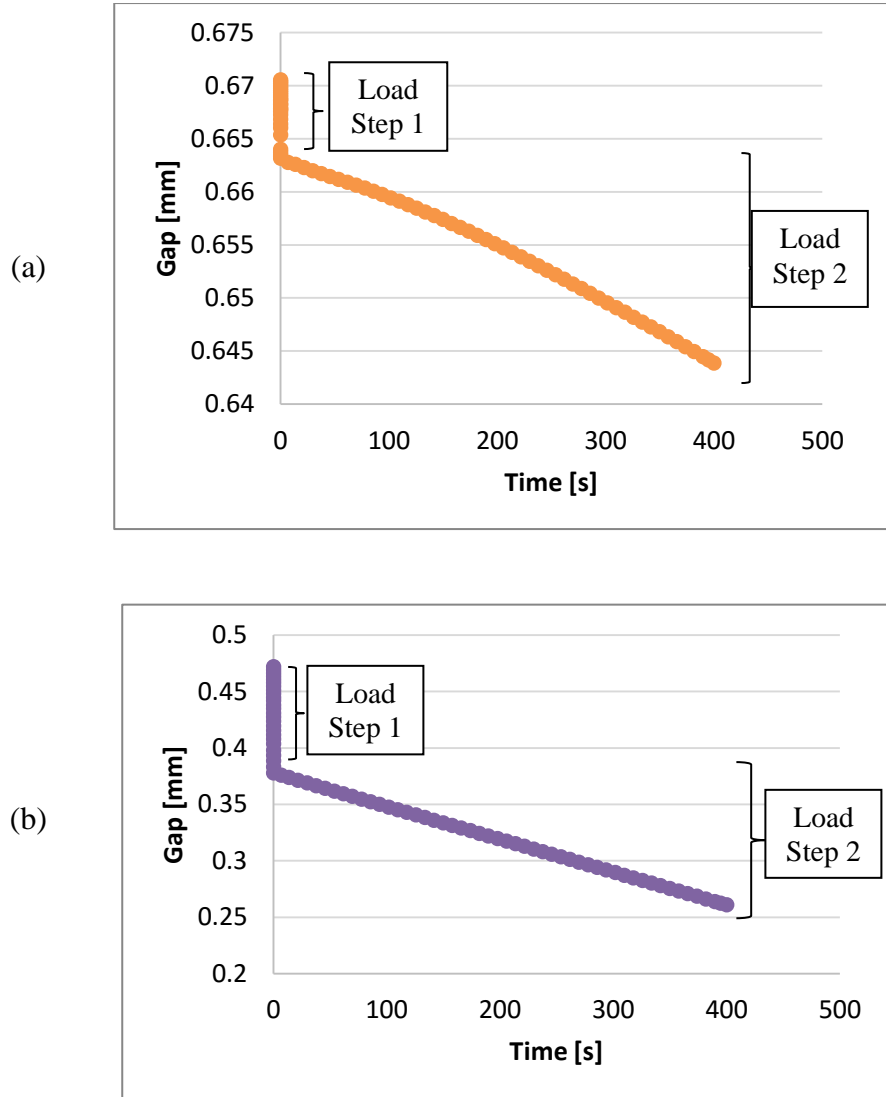


Figure 56: (a) Lateral gap between elements 8 and 9 as a function of time; and (b) Vertical gap between elements 9 and 24 as a function of time.

The graphs illustrate that the lateral and vertical gaps decreased by 0.007 mm and 0.077 mm at the conclusion of load step one. This decrease is solely due to the model deforming under gravity and the applied thermal load. The lateral and vertical gaps

between adjacent elements continue to decrease after the first load step. Between the establishment of the initial stress state and the end time for the simulation, the lateral and vertical gaps decrease by 0.019 mm and 0.117 mm respectively due to creep deformation. Comparing the decrease in the lateral and vertical gaps for the two load steps, it is evident that the impact of creep deformation is greater than the effects of thermal expansion and gravity on the closing of gaps. This makes sense given that high-temperature creep was expected to be the dominant deformation mechanism.

It should be noted that the lateral gap closes less than the vertical gap. The difference in these values can be explained by the varying mechanisms that contribute to lateral and vertical deformation. Lateral deformation occurs due to thermal expansion and creep. By contrast, vertical deformation occurs due to a combination of thermal expansion, creep, and bundle sag. Therefore, it is justifiable for the vertical gap to close more than the lateral gap.

If the trend seen for the vertical gap was to continue, it would only take 1259.34 s (~ 20 mins) for the gap between elements to be closed due to creep deformation under the specified loading conditions for a partial bundle weighing 0.872 kg. It is likely that the gap would close faster for a full bundle due to its self-weight. The slump observed in the bundle is significant because it causes changes in sub-channel geometry. The changes in sub-channel geometry may alter the coolant flow distribution and impede heat transfer from the bundle to the coolant.

8.3.2 Model Validation

To validate the model, the results from the simulation were compared with the results from the in-laboratory experiment. The radial deformation was analyzed as a function of the axial position along the outer elements and compared to the experimental results during the high-temperature plateau. Deformation in the radial direction was exclusively compared because changes in the centerline coordinates of the fuel elements from the experiment could not be directly equated with the simulation results. This is because ANSYS requires that the deformation path specified must intersect the body of the fuel element. The axial Z direction of the simulation is the X-axis in the experiment. The deformation results in the radial direction are compared for each of the six outer elements simulated. The general trend of deformation along the length of the element was captured and the results are of the same order of magnitude.

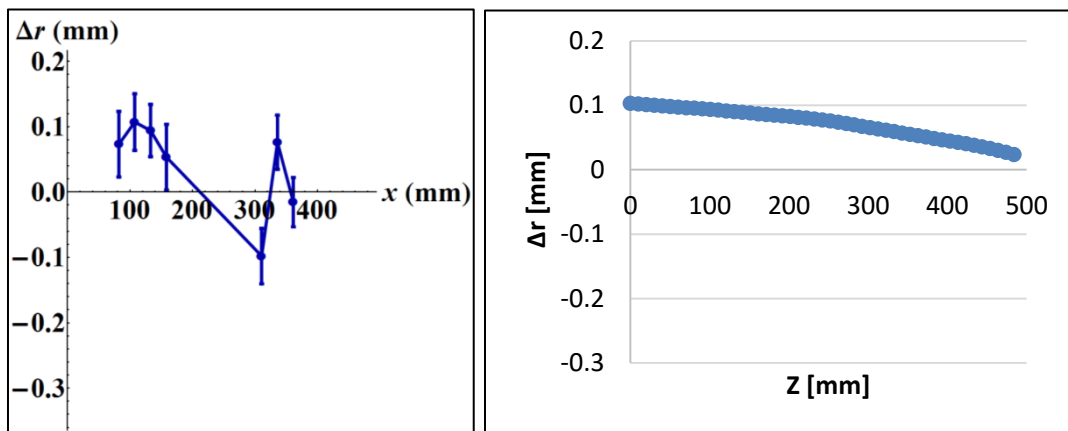


Figure 57: Radial deformation results of element 7 from the experiment (left) and simulation (right).

The radial deformation results for element 7 are compared in Figure 57. By examining the experimental results, it can be seen that the radius of the element changes by 0.1 mm near the upstream end. From this location onwards, the radial position of the

element shifts toward the center until $x = 300$ mm. There is a shift at $x = 320$ mm where the position of the radius shifts away from the center. There is a then slight upward shift in the radial position to 0.06 mm, corresponding to the region where the bearing pad is located. This is followed by a downward trend with the radial position remaining between the ranges of ± 0.04 mm near the downstream end. In comparison, the radial deformation predicted by the simulation is within the error margins of the experiment except near bearing pad locations. The simulation is unable to capture the shift in radial position in the region before the bearing pad; however, the change in radius near the bearing pad at the downstream end is within the error boundaries.

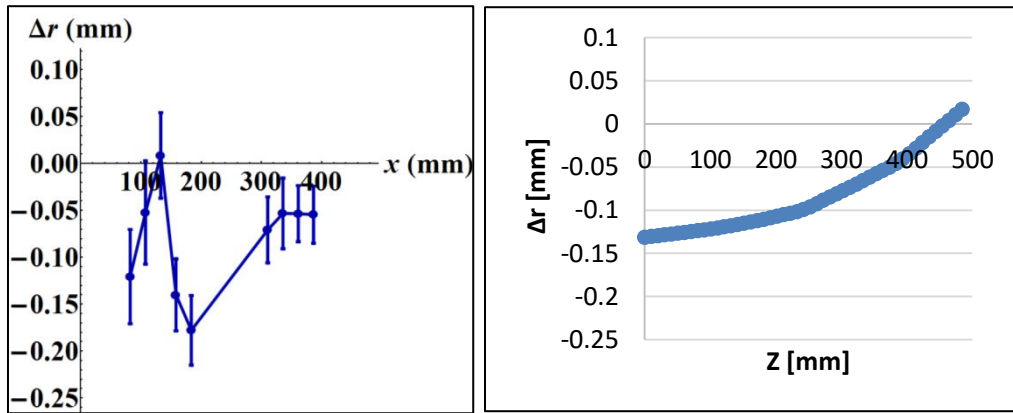


Figure 58: Radial deformation results of element 8 from the experiment (left) and simulation (right).

The deformation results for element 8 are shown in Figure 58. The radial deformation is of magnitude 0.125 mm near the upstream end. The trend observed shows that the radial position shifts toward the center. Radial deformation reduces as the location nears the region of the first bearing pad, i.e. $x = 79.4$ mm to $x = 109.4$ mm, on the element. The overall results from the simulation are in good agreement with the experimental results. The results diverge near the first bearing pad where the radius shifts towards the center at

$x = 105$ mm, followed by a shift away from the center near $x = 150$ mm. However, from $x = 150$ mm to the downstream end, the simulation results are within the margins of errors of the experimental results provided. In general, element 8 deformed towards the center and the simulation was able to capture this behaviour.

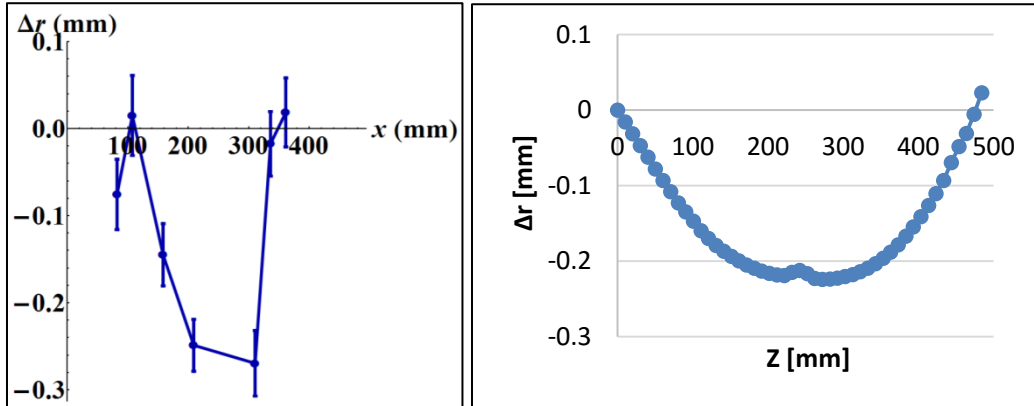


Figure 59: Radial deformation results of element 9 from the experiment (left) and simulation (right).

The deformation results for element 9 are shown in Figure 59. This fuel element is held in position by defining contact between the surfaces of its bearing pads and the pressure tube. In the experiment, minimal radial deformation was seen at $x = 100$ mm and $x = 350$ mm. However, between these points, a maximum radial deformation of 0.27 mm was observed at $x = 300$ mm. By comparison, the simulation slightly underestimates the deformation at the same location; however, the general behaviour in the radial direction exhibited by the simulation results is in good agreement with the experimental results within the region extending from $x = 120$ mm to $x = 300$ mm.

The deformation results for element 10 are shown in Figure 60. The experimental results show that the element undergoes a change of approximately 0.08 mm in the radial

direction 120 mm away from the upstream end-plate. The radial deformation increases to a local maximum of 0.19 mm at $x = 140$ mm before decreasing near the downstream end.

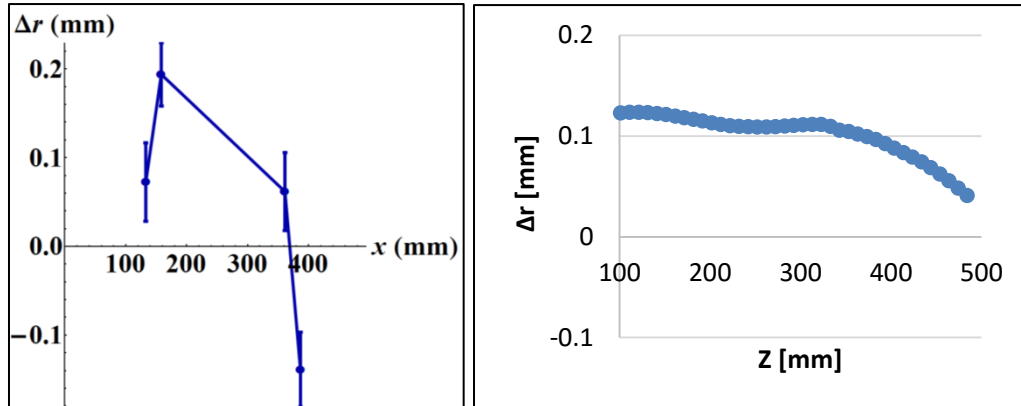


Figure 60: Radial deformation results of element 10 from the experiment (left) and simulation (right).

In comparison, the simulation shows a deformation profile that is fairly constant at 0.1 mm across the length of the element, away from the end-plates. Although the model underestimates the extent of the radial deformation at downstream end, it simulates the general behaviour of the fuel element correctly, including the shift towards the center near the downstream end.

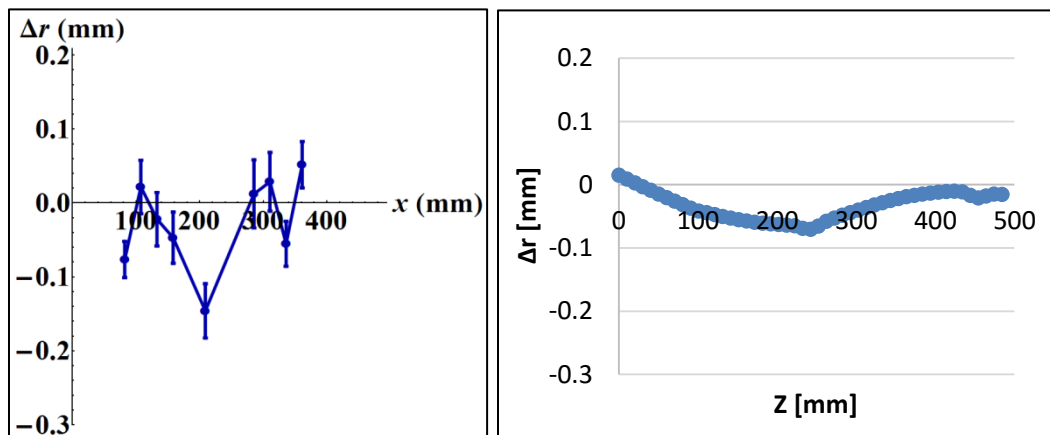


Figure 61: Radial deformation results of element 11 from the experiment (left) and simulation (right).

By visual comparison, the simulation results and the experimental results shown in Figure 61 are in good agreement. The simulation diverges from the experimental results near the ends at $x = 100$ mm and at $x = 360$ mm, which may be attributed to the constraints applied. The results at the mid-plane of the element are slightly underestimated by the model. However, the overall trend of element 11 is adequately captured in the simulation and is within the error boundaries of the experimental data.

The deformation results for element 12 are shown in Figure 62. The overall trend exhibited by the experiment is in agreement with that of the simulation. At the mid-plane, the simulation and the experimental results both demonstrate a radial deformation of approximately -0.1 mm. The simulation results follow a similar profile as the experimental near the downstream end and are within the error margins displayed with the exception of the radial deformation at near the downstream bearing pad.

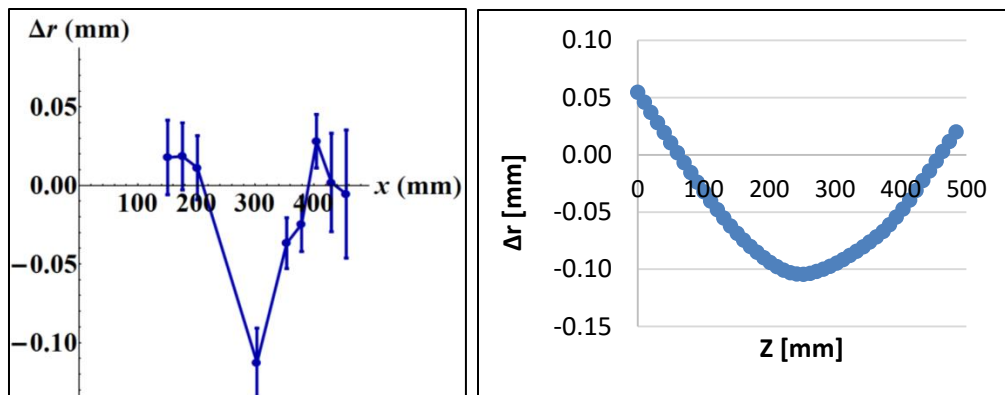


Figure 62: Radial deformation results of element 12 from the experiment (left) and simulation (right).

To help visualize the comparison between the radial deformation results from the experiment and the simulation, the radial deformation at axial positions 150 mm and 300

mm were plotted. These locations were selected because they are positioned away from bearing pads and spacer pads. The results are shown in Figure 63.

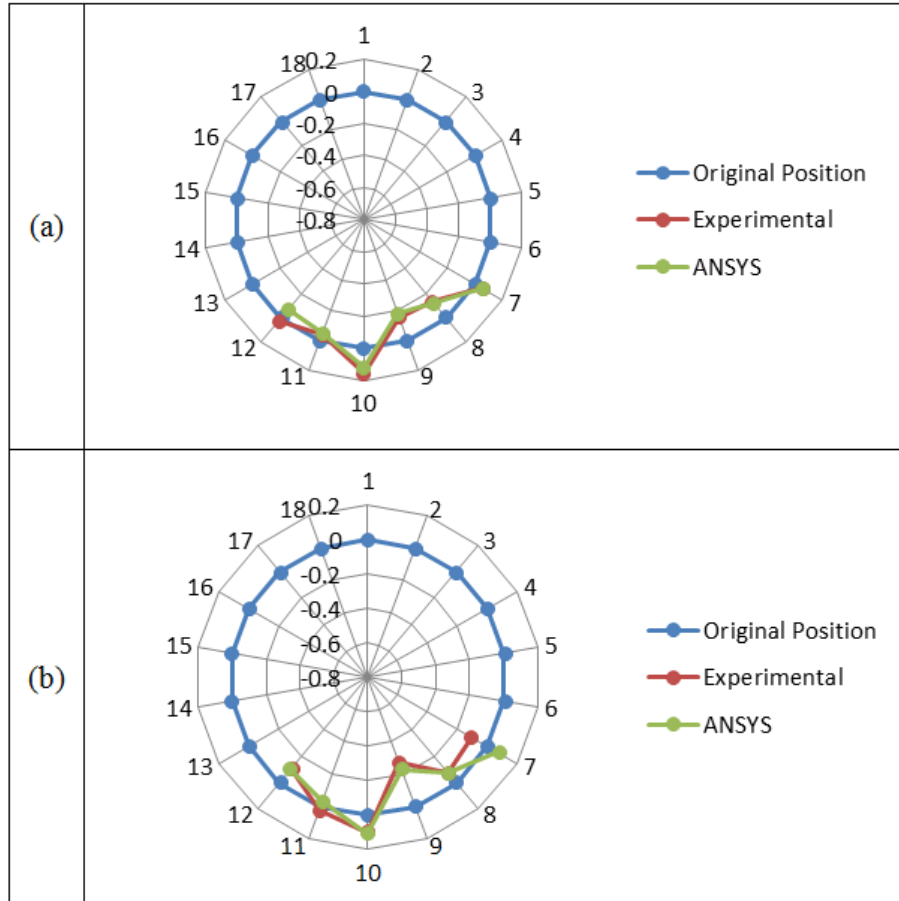


Figure 63: Radial deformation results for the outer elements at (a) 150 mm and (b) 300 mm along the length of the element.

By visual comparison of the experimental and simulation results, it is evident that there is good agreement between the two result sets. In general, the figure suggests that radial deformation tends towards the center for elements on the right but away from the center for the elements on the left. While the deformation of elements 8 and 9 diverges from the expected radial deformation of a full bundle, the fact that this behaviour is consistent in the simulation and the experiment implies that bundle droop is the dominant

mechanism at these locations. The droop behaviour is magnified in comparison to the sagging behaviour because the weight of fuel pellets, which would contribute to bundle sag, was excluded. The radial deformation of element 9 towards the center indicates that the contact between bearing pads of the outer elements and tube should have been defined to be frictional instead of no separation.

Overall, the comparison between the deformation results from the simulation and the experiment shows relatively good agreement for the outer elements simulated. While the general radial deformation is being simulated correctly for some of the elements, there is a divergence between simulation results and experimental results. This discrepancy between the simulation and experimental results for radial deformation may be due to a number of factors.

The computational inability to model all elements in the fuel bundle has a significant influence on the agreement between experimental and simulation results. Only including 12 elements reduces the force exerted on the bearing pads of elements 9 and 10 due to the weight of 12 elements instead of 37. Simulating a partial bundle isolates the localized radial deformation component of the simulated elements from the overall bundle. This isolation makes it difficult to attribute predictive success or failure to the simulation in modeling radial deformation because all 37 elements interact with one another in significant ways through defined connections of the elements at several locations along the fuel element. The different forces acting at these locations vary greatly from one element to another, as evident from the experiment results, due to differences in thermoplastic deformation, temperature differences, and material properties. Comparing the radial deformation from

the simulation with experimental results poses challenges as the magnitude and interaction of all 37 elements could not be included in the simulation.

Another factor which may contribute to the differences between the experimental and simulation results is the idealization of the geometry through element type. Using shell elements meant that a temperature gradient could not be defined through the thickness of the sheath. This would influence the radial deformation of the outer elements near the location of the bearing pads, which facilitate convective heat transfer in the experiment. The deformation results of the simulation are also impacted by the approximation of temperature gradients at the bearing pads since this data was not provided by the thermocouples.

For further comparison, the experimental results need to be examined critically since the results are only based on one experimental test. The experiment needs to be repeated because there was evidence of a systematic error in the element displacement results due to the thermo-elastic motion of the pressure tube [17]. This meant that the position of the tube shifted very slightly relative to the laser sensors recording the deformation data. While the error does not completely explain the divergence between simulation and experimental results, it demonstrates a need to amass a sufficient amount of data, which can be evaluated for reproducibility. The reproducibility criterion will help establish the external validity of laboratory experiments and provide comprehensive results that will help distinguish between the conflicting data shown in the experiment and the simulation. It will also serve to reduce the large measurement uncertainties seen in the experiment.

8.3.3 Limitations

Outlining the model limitations helps determine the range of applicability of the model and ensures that improvements can be made to increase the agreement between the results from the simulation and the experiment. A primary limitation of the model is the simplification used in the implementation of the sheath creep model. Only the dominant deformation mechanism of diffusional creep was considered in this model due to its heightened sensitivity to high temperatures. However, the microstructural creep model must also account for the changes in the structure of the Zircaloy-4 sheath due to grain growth, strain hardening and annealing [28]. These effects are not currently included in the model because the mechanisms other than diffusional creep have a small effect of microstructural creep over the short interval of 400 s.

As explained in Section 3.5, sheath oxidation has a significant impact on the creep strain rate of Zircaloy-4 because the heat released during the oxidation reaction would increase the temperature of the system. It would also influence the strength and ductility of the material [33]. The effects of sheath oxidation were not included in this model because a coupled analysis between the fluid dynamics component in ANSYS Fluent and the thermal-mechanical component in ANSYS Workbench would be required to include the effects of sheath oxidation. Since the resulting coupled model would be extremely computationally intensive given the detailed geometry of the model and oxidation was not seen on the bundle after the experiment, including the effects of sheath oxidation was deemed surplus to the requirements of this thesis.

While the correlation used for Young's modulus displays the temperature dependence of Zircaloy-4, it does not account for the effects of material anisotropy due to the cold-worked manufacturing process of Zircaloy-4. The correlation also neglects the hardening effects of fast neutron irradiation. While this omission is not of great concern in this simulation, it would be a source of error when fuel pellets are added to the model. The correlation also does not include strengthening effects relating to sheath oxidation. The approximate model of the modulus of elasticity was used because it was expected that the plastic strains induced by sheath creep would outpace the relatively small elastic strains in the simulation. This approximation can be corrected by using a Zircaloy-4 material model which includes material anisotropy, oxygen strengthening and radiation hardening.

Since the intent was to validate the model results against the experimental results, it was deemed appropriate to use the sheath temperatures from the experiment as a thermal boundary condition. This approximation meant that an uncoupled mechanical simulation would be conducted instead of a coupled thermal and mechanical simulation. This simplifies the thermal loading and may lead to divergence between experimental and simulation results. Furthermore, the thermal data had to be linearly interpolated in the regions between thermocouples to map the temperature distribution from the experiment. Although the temperature distribution input was consistent with the temperature interpolated from the thermal imager in the experiment, the approximation in temperature distribution would result in differences between the simulation and the experiment at locations in between the planes of the instrumented thermocouples.

Further limitations on the model are related with computational resources. The model was limited to 12 fuel elements because difficulties were encountered when all 37 fuel elements were added. The difficulties were related to the excessive computational requirements of the simulation. The current uncoupled simulation of the partial bundle requires 8 GB of (RAM) memory and took just over 90.3 hours to produce a result file, which was approximately 20 GB. Given these memory requirements for a third of the bundle, expanding the number of elements to include the remaining 25 elements will require high performance computing. ANSYS offers high performance computing licenses, which can be used to decrease solution time by solving the simulation through multiple cores on a cluster computer. Being able to simulate the entire bundle would serve to reduce the differences between the experimental and simulation results.

8.4 Conclusion

In summary, a non-linear simulation was conducted to describe the high-temperature deformation behaviour of a partial bundle. The partial bundle was composed of 12 fuel elements, whose individual thermal-mechanical response and modeling technique had been previously benchmarked and verified in Chapters 6 and 7. The bundle deformation model simulated the effects of thermal-mechanical loading and creep on the assembly simultaneously. The results illustrated that fuel element elongation, vertical deflection and lateral bowing caused the bundle to deform. Under the thermal-mechanical loading specified, the deformation was not significant enough to close the gaps between adjacent fuel elements. However, over a short period of 400 s, it was noted that the gaps between adjacent elements reduce significantly in the vertical and lateral direction due to creep

deformation of the individual fuel elements and the end-plates. The resulting deformation altered sub-channel geometry and would result in changes in the coolant flow through the bundle. Since the gaps did not close between adjacent elements and between the elements and the pressure tube, it can be concluded that the contact definition did not engage. The absence of the closure of the gaps is consistent with the results observed in the experiment, wherein the bundle did not deform to the extent that contact was established between the outer elements and the quartz tube. The radial deformation results obtained from the model were validated against experimental to show confidence in the ability of the model to capture the simultaneous effects of thermal-mechanical loading and creep. There was good agreement between the experimental and simulation results as the general radial deformation was simulated correctly for the outer elements.

9 Summary and Conclusions

The goal of this thesis was the development of a 3-D Finite Element model to predict the geometric deformation of a CANDU fuel bundle in response to given thermal and mechanical loads occurring under conditions similar to those of dry-out and LB-LOCA. To this end, a partial bundle assembly was developed to model the thermal-mechanical deformation behaviour at these conditions. The bundle deformation model simulated the following phenomena:

- Axial elongation of the fuel elements as part of a bundle;
- Sagging of the fuel elements under their self-weight;
- Bundle slumping due to high-temperature creep deformation; and
- Fuel element bowing due to the applied non-uniform temperature gradient.

The interactions in the bundle between the fuel elements directly at the spacer pads and indirectly through contact at the end-plates were considered to model the described phenomena. The model also accounted for element and end-plate deformation due to thermal expansion, elastic strain, plastic strain, contact forces, and diffusional creep. The temperature distribution of the bundle was mapped from an in-laboratory experiment. This allowed for an uncoupled mechanical analysis to be conducted, reducing the computational time required to achieve convergence. It also provided experimental results against which the model was validated. The bundle deformation model placed special emphasis on improving the accuracy of contact modeling within the bundle by increasing the detail in bundle geometry and excluding fuel-related phenomena. The reason to undertake this

endeavour was to establish a foundation for the addition of fuel pellets as part of further development of this model.

To demonstrate proof of concept for the bundle model, the deformation behaviour of a single fuel element was correctly modeled and showed excellent agreement with the analytical results. Since the thermal-mechanical loading conditions applied for the deformation model mimicked those of the experiment conducted by CNL, the radial deformation results for the outer elements were compared. Although the general radial deformation profile was simulated correctly, the experimental and simulation results diverged at some locations along the length of the fuel elements. The differences were especially prominent near the bearing pads of some of the elements. The experimental and simulation results may differ due to the limitations of the deformation model, which are detailed in Section 8.3.3.

In conclusion, this study demonstrates the feasibility of a 3-D bundle deformation model that includes contact between adjacent elements, non-uniform thermal gradients and creep deformation at off-normal operating conditions. This deformation model is the first step in the lead up to the development of a more comprehensive deformation model, which would include fuel pellets and fuel-related phenomena. The ability of this model to simulate the varying phenomena associated with temperature conditions related to off-normal conditions prove it to be a useful tool in assessing changes in sub-channel geometry and the integrity of the fuel bundle.

10 References

- [1] W. J. Garland, "The Essential CANDU, A Textbook on the CANDU Nuclear Power Plant Technology," University Network of Excellence in Nuclear Engineering, Canada, 2015.
- [2] A. R. Foster and R. L. Wright, Basic Nuclear Engineering, Boston: Allyn and Bacon, 1983.
- [3] D. R. Olander, "Fundamental Aspects of Nuclear Reactor Fuel Elements," U.S Department of Energy, 1976, p. 131.
- [4] S. Glasstone and A. Sesonske, Nuclear Reactor Engineering: Reactor Design Basics, Springer, 2013.
- [5] A. I. Miller, J. Luxat, E. G. Price, R. B. Duffey and P. J. Fehrenbach, Nuclear Engineering Handbook, Boca Raton, Florida: Taylor and Francis Group, LLC, 2009, pp. 141-196.
- [6] M. Tayal and M. Gacesa, "Fuel," in *The Essential CANDU, A Textbook on the CANDU Nuclear Power Plant Technology*, Hamilton, University Network of Excellence in Nuclear Engineering, 2014.
- [7] M. H. A. Piro, F. Wassermann, S. Grundmann, B. W. Leitch and C. Tropea, "Progress in On-going Experimental and Computational Fluid Dynamic Investigations within a CANDU Fuel Channel," *Nuclear Engineering and Design*, vol. 299, pp. 184-200, 2016.
- [8] J. A. L. Robertson, The Basics of Nuclear Energy, Chalk River: Atomic Energy of Canada Ltd., 1982.
- [9] J. Veeder and M. H. Schankula, "Bowing of Pelletized Fuel Elements: Theory and In-Reactor Experiments," *Nuclear Engineering and Design*, vol. 29, pp. 167-179, 1974.
- [10] W. Hartmann and J. Y. Jung, "Safety Analysis Methodology for Aged CANDU-6 Nuclear Reactors," *Nuclear Engineering and Technology*, vol. 45, no. 5, pp. 581-588, 2013.
- [11] E. Kohn, R. Hu, G. I. Hadaller and R. A. Fortman, "Understanding CANDU Fuel Bowing in Dryout: An Industry Approach," 1997. [Online]. Available: http://www.iaea.org/inis/collection/NCLCollectionStore/_Public/31/006/31006128.pdf. [Accessed 9 March 2016].
- [12] J. S. Bell and B. J. Lewis, "CANDU fuel bundle deformation modelling with COMSOL," *Journal of Nuclear Engineering and Design*, vol. 250, pp. 134-141, 2012.
- [13] S. G. Xu, Z. Xu and M. Tayal, "BOW Code Development-Modeling of In-Reactor Bundle Deformation," in *Proceedings of Ninth International Conference on CANDU Fuel*, Belleville, Canada, 2005.

- [14] L. C. Walters and A. F. Williams, "Fuel Bundle Deformation Model," in *8th International Conference on CANDU Fuel*, Honey Harbour, ON, 2003.
- [15] M. R. McCluskey, A Three Dimensional Finite Element Analysis of a CANDU Fuel Element, Kingston: RMC Thesis, 2012.
- [16] C. Krasnaj, A Solid Element Approach to Analyzing CANDU Fuel Element Behaviour Under Post-Dryout Heat Transfer Conditions, Kingston: RMC Thesis, 2015.
- [17] C. Thiriet, R. Dickson and K. Colins, "Fuel Bundle Behaviour Test in the Fuel Bundle Behaviour Apparatus," Canadian Nuclear Labs, Chalk River, 2015.
- [18] J. R. Thome, "Engineering Data Book 3," Wolverine Tube, Inc., 2007.
- [19] "Trip Parameter Acceptance Criteria for the Safety Analysis of CANDU Nuclear Power Plants," Canadian Nuclear Safety Commission, May 2006.
- [20] F. P. Beer, E. R. Johnston and J. T. DeWolf, *Mechanics of Materials*, New York: McGraw Hill, 2002.
- [21] D. Wolk, "Advanced Finite Element Methods," Kingston, 2015.
- [22] H. W. Haslach and R. W. Armstrong, "Plasticity," in *Deformable Bodies and Their Material Behaviour*, Hoboken, New Jersey, Wiley, 2004, pp. 316-382.
- [23] H.-H. Lee, *Finite Element Simulations with ANSYS Workbench 15*, Mission, KS: SDC Publications, 2014.
- [24] ANSYS Inc., *ANSYS Mechanical Structural Nonlinearities*, Canonsburg, PA: ANSYS Inc, 2012.
- [25] H. Kraus, *Creep Analysis*, New York: Wiley, 1980.
- [26] H. E. Sills, "ELOCA Fuel Element Behaviour During High-Temperature Transients," AECL Report AECL-6357, Chalk River, ON, 1979.
- [27] B. J. Lewis, F. C. Iglesias, R. S. Dickson and A. Williams, "Overview of High Temperature Fuel Behaviour with Relevance to CANDU Fuel," *Journal of Nuclear Matter*, pp. 67-86, 2009.
- [28] H. E. Sills and R. A. Holt, "NIRVANA: A High-Temperature Creep Model for Zircaloy Fuel Sheathing," AECL Report AECL-6412, Chalk River, ON, 1979.
- [29] SCDAP/RELAP5 Development Team, Volume IV: MATPRO--A Library of Material Properties for Light-Water-Reactor Accident Analysis, Idaho Falls, ID: Idaho National Engineering and Environmental Laboratory, Oct, 1997.
- [30] E. Gutierrez, "Creep," Rensselaer Polytechnic Institute, Hartford, 2005.
- [31] F. C. Iglesias, D. B. Duncan, S. Sagat and H. E. Sills, "Verification of the Model for Zircaloy Oxidation During High Temperature Transients," *Journal of Nuclear Materials*, vol. 130, pp. 36-44, 1985.
- [32] S. Leistikow and G. Schanz, "Oxidation Kinetics and Related Phenomena of Zircaloy-4 Fuel Cladding Exposed to High Temperatures Steam And Hydrogen-Steam Mixtures under PWR Accident Conditions," *Nuclear Engineering and Design*, vol. 103, pp. 65-84, 1983.

- [33] K. Pettersson, "Nuclear Fuel Behaviour in Loss-of-Coolant Accident (LOCA) Conditions," Nuclear Energy Agency, France, 2009.
- [34] D. G. Hurst and E. Critoph, "Fuel Channel Behaviour," in *Canada Enters the Nuclear Age: A Technical History of Atomic Energy of Canada Limited*, Montreal, McGill-Queen's University Press, 2014, pp. 310-314.
- [35] J. Pachner, P. Kumar and J. C. Almagro, "Assessment and Management of Ageing of Major Nuclear Power Plant Components Important to Safety: CANDU Pressure Tubes," IAEA, Vienna, 1998.
- [36] M. Tayal, "Modelling CANDU Fuel under Normal Operating Conditions: ELESTRES Code Description," AECL Report - AECL-9331, Chalk River, ON, 1987.
- [37] H. E. Sills, "ELOCA: Fuel Element Behavior During High-Temperature Transients," AECL Report - AECL-6357, Chalk River, ON, 1979.
- [38] A. Prudil, B. J. Lewis, P. K. Chan and J. J. Baschuk, "Development and testing of the FAST fuel performance code: Normal operating conditions (Part 1)," *Nuclear Engineering and Design*, vol. 282, pp. 158-168, 2015.
- [39] M. Tayal, "Modelling the Bending/Bowing of Composite Beams such as Nuclear Fuel: The BOW Code," *Nuclear Engineering and Design*, vol. 116, pp. 149-159, 1989.
- [40] A. F. Williams and S. Yatabe, "An ANSYS based 3-Dimensional Model of a CANDU fuel," 2014.
- [41] H. C. Suk, K. S. Sim, J. H. Park and G. S. Park, "Thermally-induced Bowing of CANDU Fuel Elements," in *Canadian Nuclear Society's 4th International Conference on CANDU Fuel*, Pembroke, ON, 1995.
- [42] D. Gaston, C. Permann, D. Anders, J. Peterson and J. Miller, "MOOSE Training Workshop," January 2013. [Online]. Available: <http://www.mooseframework.org/static/media/uploads/docs/main.pdf>. [Accessed November 2016].
- [43] K. Gamble, Modeling Three-Dimensional Deformation Mechanisms in CANDU Reactor Fuel Elements, Kingston: RMC Thesis, 2014.
- [44] S. Moaveni, Finite Element Analysis, 2003: Pearson Education, New Jersey.
- [45] ANSYS Inc., ANSYS Mechanical APDL Thermal Analysis Guide, Canonsburg, PA: Release 14.0, November 2011.
- [46] ANSYS, Inc., ANSYS Contact Technology Guide, Canonsburg, PA: ANSYS, Inc., 2013.
- [47] N. Mozzani, Q. Auzoux, D. LeBoulch, E. Andrieu and C. Blanc, "Mechanical Behavior of Recrystallized Zircaloy-4 Under Monotonic Loading at Room Temperature: Tests and Simplified Anisotropic Modeling.," *Journal of Nuclear Materials*, vol. 447, no. 1, pp. 94-106, 2014.

- [48] G. G. Chassie, "ELESTRES-IST 1.2: User's Manual," Atomic Energy of Canada Limited, Mississauga, ON, 2006.
- [49] D. J. Caswell, A. F. Williams and W. R. Richmond, "ELOCA 2.2: User's Manual," Atomic Energy of Canada, Mississauga, ON, 2005.
- [50] S. Oldberg, A. K. Miller and G. E. Lucas, "Advances in Understanding and Predicting Inelastic Deformation in Zircaloy," in *Fourth International Conference on Reactive and Refractory Metals and Alloys*, Stratford-upon-Avon, England, 1979.
- [51] Saint-Gobain Quartz PLC, "MATWEB - Material Property Data," 2016. [Online]. Available: <http://www.matweb.com/search/DataSheet.aspx?MatGUID=f87baab60b524266adda0c7e5b3a6caa>.
- [52] R. D. Page, "Canadian Power Reactor Fuel," Atomic Energy of Canada Limited, Sheridan Park, Ontario, 1976.
- [53] A. Belov, R. W. L. Fong, B. W. Leitch, T. Nitheanandan and A. Williams, "Characterizing High-Temperature Deformation of Internally Heated Nuclear Fuel Element Simulators," *CNL Nuclear Review*, vol. 5, pp. 67-84, 2016.
- [54] W. Nash, *Schaum's Outline of Strength of Materials*, Amherst, USA: McGraw-Hill, 1998.
- [55] K. Naumenko and H. Altenbach, *Modeling of Creep for Structural Analysis*, Heidelberg, Germany: Springer-Verlag, 2007.
- [56] A. A. Becker, T. H. Hyde, W. Sun and P. Andersson, "Benchmarks for Finite Element Analysis of Creep Continuum Damage Mechanics," *Computational Materials Science*, vol. 25, no. 1-2, pp. 34-41, September 2002.
- [57] P. J. Blau, "Fundamentals of Sliding Friction," in *Friction Science and Technology*, Boca Raton, USA, CRC Press, 2008, pp. 119-182.
- [58] L. C. Walters and A. F. Williams, "CANDU Fuel Bundle Deformation Model," in *International ANSYS Conference*, Pittsburgh, PA, 2004.
- [59] S. D. Yu, M. Tayal and Z. Xu, "Creep Bowing in CANDU Fuel: Modelling and Applications," in *International Conference on CANDU Fuel*, Toronto, Canada, 1997.
- [60] P. K. Chan, P. Alavi, G. G. Chassie, J. H. Lau, P. L. Purdy, D. Rattan, R. Sejnoha and M. Tayal, "An Update on the Design Verification of the CANFLEX Fuel Bundle," Canadian Nuclear Society, Canada, 1999.
- [61] S. Xu, Z. Xu, H. Fan and T. Nitheanandan, "Modelling of Fuel Bundle Deformation at High Temperatures: Requirements, Models and Steps for Consideration," in *Proceedings of Eleventh International Conference on CANDU Fuel*, Niagara Falls, Canada, 2010.
- [62] D. R. Olander, *Fundamental Aspects of Nuclear Reactor Fuel Elements*, U.S Department of Energy, 1976, p. 131.

Appendices

Appendix A – Experimental Results

In the experiment, individual fuel elements were assumed to have circular geometry, with the center corresponding to the coordinates, $[y_0, z_0]$. Deflections in the lateral and vertical direction were calculated by accounting for the changes in the fuel element centerline coordinates from the reference values for the centerline coordinates at approximately 603 K where no deformation was expected to occur. The radial position was given by the parameter, r and was calculated in a similar manner to the vertical and lateral deflections.

For the results, it should be noted that a negative value corresponds to a shift in the opposite direction. The system also uses a left-hand coordinate system with y corresponding to the lateral direction and z corresponding to the vertical axis.

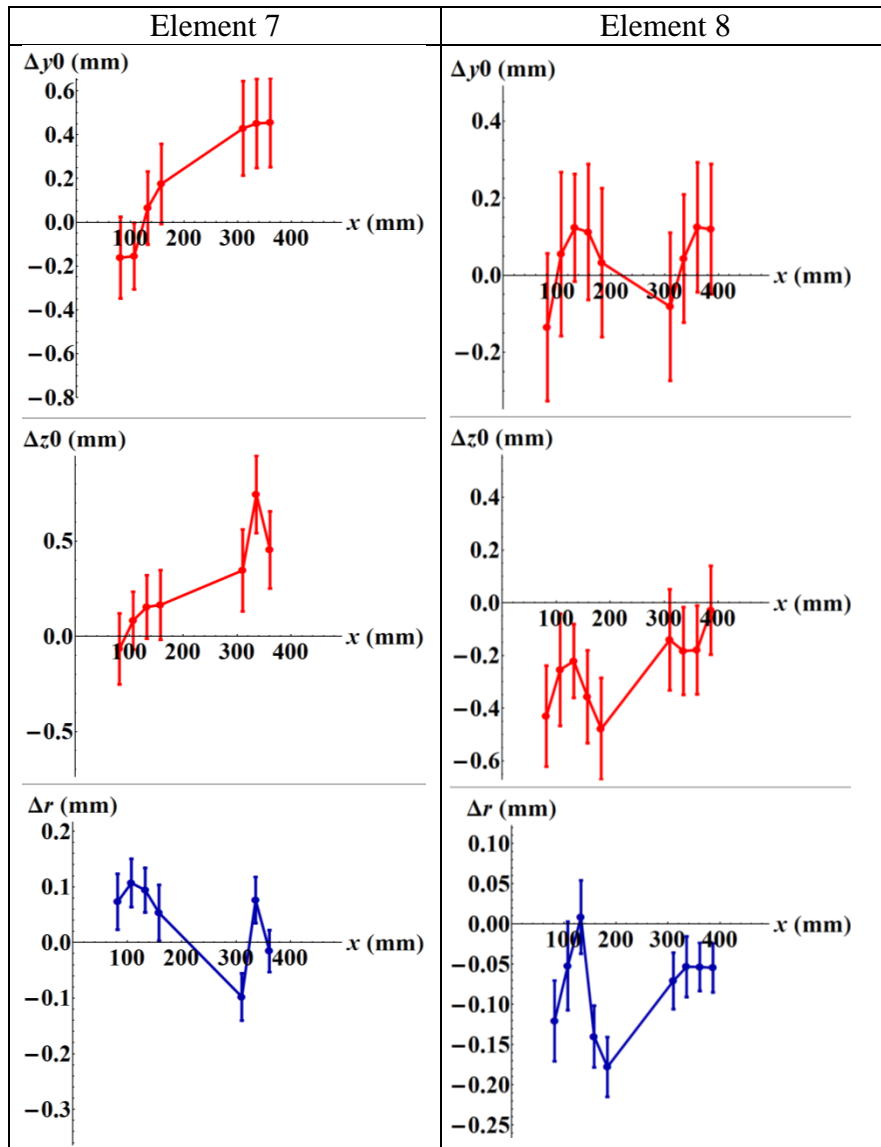


Figure 64: Lateral and vertical deflections and radial deformation as a function of the axial position of elements 7 and 8 during high-temperature phase.

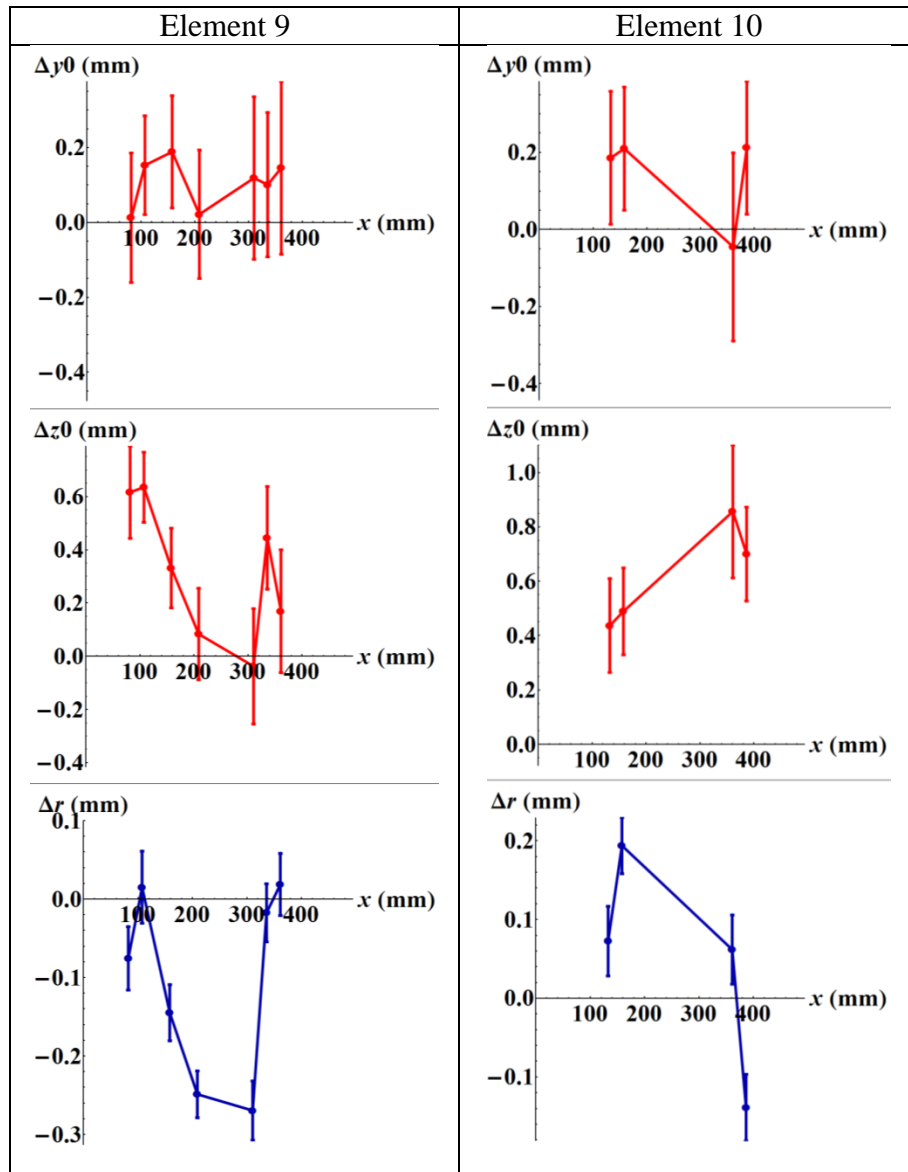


Figure 65: Lateral and vertical deflections and radial deformation as a function of the axial position of elements 9 and 10 during high-temperature phase.

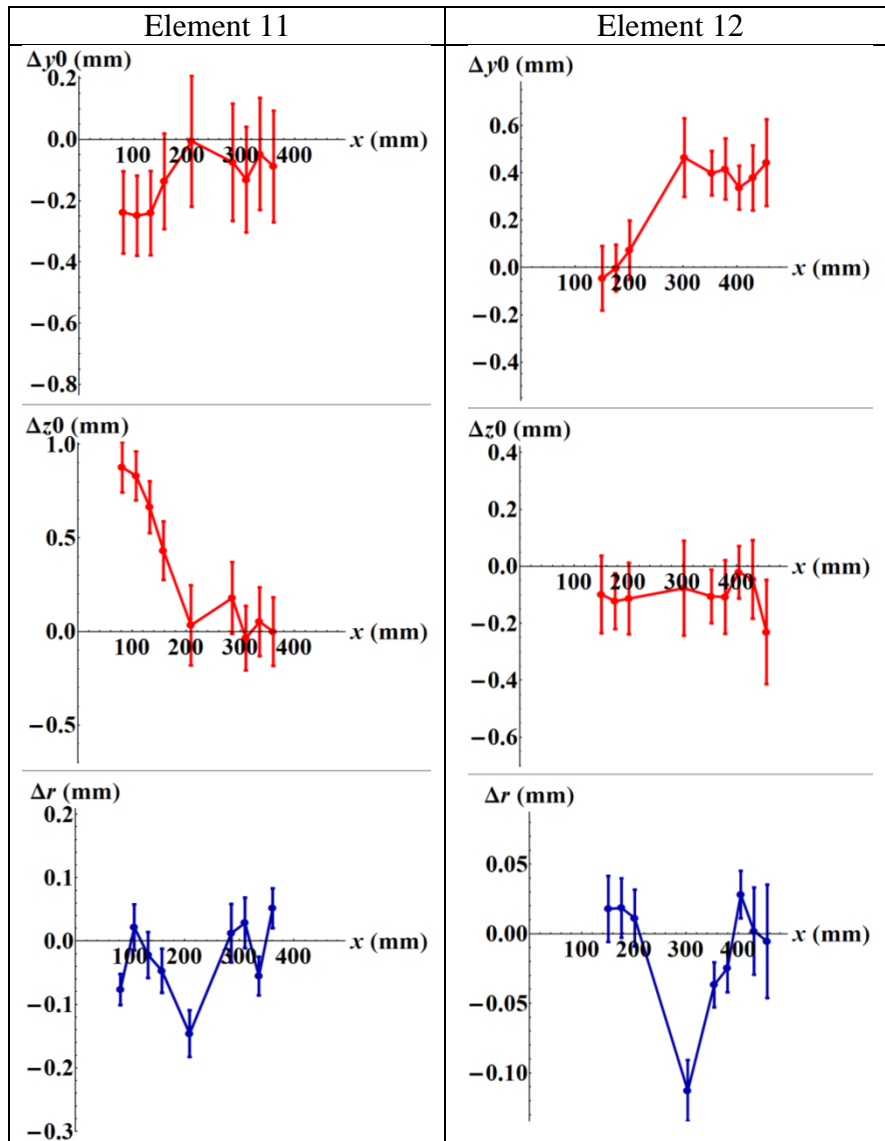


Figure 66: Lateral and vertical deflections and radial deformation as a function of the axial position of elements 11 and 12 during high-temperature phase.

Appendix B – Sample Calculations

Flexural Rigidity

$EI = \frac{-PL^3}{48\delta}$ $EI = \frac{-200 N(484.2mm)^3}{48(19.113mm)}$ $EI = 24.76 N \cdot mm^2$	(B-1)
---	-------

Thermal Bowing

$\delta = \frac{-\alpha L^2}{16b} (\Delta T_i)$ $\delta = \frac{-(6.721 \times 10^{-6} mm \cdot mm^{-1} \cdot K^{-1})(484.2 mm)^2}{16(6.55 mm)} (100 K)$ $\delta = -1.5042 mm$	(B-2)
--	-------

Creep Deformation

Stress Verification

$\sigma = \frac{F}{A}$ $\sigma = \frac{F}{\pi(r_o - r_i)}$ $\sigma = \frac{20 N}{\pi(6.55^2 - 6.17^2) mm^2}$ $\sigma = 1.317 MPa$	(B-3)
---	-------

Strain

$\varepsilon = \frac{\sigma}{E} = \frac{1.317 MPa}{45055}$ $\varepsilon = 2.92 \times 10^{-5} \frac{mm}{mm}$	(B-4)
--	-------

Creep Strain Rate

$\dot{\epsilon}_{cr} = F \left(\frac{\sigma_a}{d} \right)^m e^{-\frac{Q}{T}}$ $\dot{\epsilon}_{cr} = C_1 (\sigma_a)^{C_2} e^{-\frac{C_3}{T}}$ $\dot{\epsilon}_{cr} = 1.90 \times 10^{-15} (1317071.7 \text{ Pa})^2 \exp\left(\frac{-9431}{1080}\right)$ $\dot{\epsilon}_{cr} = 5.3154 \times 10^{-7} \text{ s}^{-1}$	(B-5)
---	-------

Creep Strain at 400 s

$\dot{\epsilon}_{cr} = \frac{\epsilon_{cr}}{\Delta t}$ $\epsilon_{cr}(400 \text{ s}) = \dot{\epsilon}_{cr} \Delta t$ $\epsilon_{cr}(400 \text{ s}) = (5.3154 \times 10^{-7} \text{ s}^{-1})(400 \text{ s})$ $\epsilon_{cr}(400 \text{ s}) = 2.12616 \times 10^{-4} \frac{\text{mm}}{\text{mm}}$	(B-6)
---	-------

Axial Deformation

$dl = l_o \alpha dt$ $dl = (484.2 \text{ mm}) \left(6.721 \times 10^{-6} \frac{\text{mm}}{\text{mm} \cdot \text{K}} \right) (1163.2 - 303.15) \text{ K}$ $dl = 2.799 \text{ mm}$	(B-7)
---	-------

Diametric Deformation

$d_1 = d_o (\alpha dt + 1)$ $d_1 = 13.1 \text{ mm} \left(\left(6.721 \times 10^{-6} \frac{\text{mm}}{\text{mm} \cdot \text{K}} \right) (1163.2 - 303.15) \text{ K} + 1 \right)$ $d_1 = 13.1757 \text{ mm}$ $\Delta d_1 = 13.1757 - 13.1 \text{ mm}$ $\Delta d_1 = 0.0757 \text{ mm}$	(B-8)
--	-------

Thermal Strain

$dl = l_o \alpha dt$ $\frac{dl}{l_o} = \varepsilon_{th} = \alpha dt$ $\varepsilon_{th} = \left(6.721 \times 10^{-6} \frac{mm}{mm \cdot K} \right) (1163.2 - 295.15) K$ $\varepsilon_{th} = 5.833 \times 10^{-3} mm \cdot mm^{-1}$	(B-9)
--	-------

Thermal Stress

$\sigma_{th} = E \varepsilon_{th}$ $\sigma_{th} = (45000 MPa) \left(5.779 \times 10^{-3} \frac{mm}{mm} \right)$ $\sigma_{th} = 260 MPa$	(B-10)
--	--------

Bending Stress

Gravitational Force on an Empty Fuel Element

$F = mg$ $F = (0.05156 kg) \left(9.81 \frac{m}{s^2} \right)$ $F = 0.5058 N$	(B-11)
--	--------

Uniformly distributed self-load over thermally elongated element

$w = \frac{F}{l}$ $w = \frac{0.5058 N}{487 mm}$ $w = 1.038 \times 10^{-3} \frac{N}{mm}$	(B-12)
---	--------

Section Modulus

$Z = \frac{0.78(R_o^4 - R_i^4)}{R_o}$ $Z = \frac{0.78(6.589^4 - 6.208^4) \text{ mm}^4}{6.589 \text{ mm}}$ $Z = 47.17 \text{ mm}^3$	(B-13)
--	--------

Maximum Bending Stress

$\sigma = \frac{wL^2}{8Z}$ $\sigma = \frac{\left(1.038 \times 10^{-3} \frac{N}{mm}\right) (487\text{mm})^2}{8(47.171 \text{ mm}^3)}$ $\sigma = 0.65 \text{ MPa}$	(B-14)
--	--------

Displacement due to bending

$\delta = -\frac{5wL^4}{384EI}$ $\delta = -\frac{5 \left(1.038 \times 10^{-3} \frac{N}{mm}\right) (487\text{mm})^4}{384 \left(45055 \frac{N}{mm^2}\right) (312.91 \text{ mm}^4)}$ $\delta = -0.054 \text{ mm}$	(B-15)
--	--------

Appendix C – Initial Contact Information

Name	Contact Side	Type	Status	Geometric Gap [mm]	Resulting Pinball [mm]
No Separation - Multiple To Solid	Contact	No Separation	Closed	0	0.29949
Bonded - 25 To Downstream End Plate	Contact	Bonded	Closed	0.4519	1.8149
Bonded - 25 To Upstream End Plate	Contact	Bonded	Closed	0.45186	1.8156
Frictionless - Multiple To Solid	Contact	Frictionless	Closed	0.11908	1.1968
Bonded - 24 To Upstream End Plate	Contact	Bonded	Closed	0.45187	1.8155
Bonded - 9 To Downstream End Plate	Contact	Bonded	Closed	0.46138	1.8154
Bonded - 24 To Downstream End Plate	Contact	Bonded	Closed	0.45188	1.8313
Bonded - 11 To Downstream End Plate	Contact	Bonded	Closed	0.46812	1.8059
Bonded - 12 To Upstream End Plate	Contact	Bonded	Closed	0.45186	1.8155
Bonded - 10 To Upstream End Plate	Contact	Bonded	Closed	0.45182	1.8149
Bonded - 11 To Upstream End Plate	Contact	Bonded	Closed	0.45187	1.8157
Bonded - 12 To Downstream End Plate	Contact	Bonded	Closed	0.45188	1.8171
Bonded - 10 To Downstream End Plate	Contact	Bonded	Closed	0.4519	1.8132
Bonded - 7 To Downstream End Plate	Contact	Bonded	Closed	0.4634	1.8155
Bonded - 9 To Upstream End Plate	Contact	Bonded	Closed	0.45189	1.7988
Bonded - 8 To Downstream End Plate	Contact	Bonded	Closed	0.45191	1.8155
Bonded - 9 To 9	Target	Bonded	Closed	1.86E-04	1.1187
Bonded - 10 To 10	Target	Bonded	Closed	1.79E-04	1.1157

Bonded - 7 To 7	Target	Bonded	Closed	2.03E-04	1.1129
Bonded - 7 To 7	Target	Bonded	Closed	2.09E-04	1.1172
Bonded - 9 To 9	Target	Bonded	Closed	2.21E-04	1.1126
Bonded - 7 To 7	Target	Bonded	Closed	2.13E-04	1.1182
Bonded - 11 To 11	Target	Bonded	Closed	2.55E-04	1.1226
Bonded - 11 To 11	Target	Bonded	Closed	2.12E-04	1.1125
Bonded - 12 To 12	Target	Bonded	Closed	1.99E-04	1.1125
Bonded - 9 To 9	Target	Bonded	Closed	2.20E-04	1.1215
Bonded - 11 To 11	Target	Bonded	Closed	2.40E-04	1.1185
Bonded - 10 To 10	Target	Bonded	Closed	2.54E-04	1.1166
Bonded - 12 To 12	Target	Bonded	Closed	1.75E-04	1.1176
Bonded - 12 To 12	Target	Bonded	Closed	2.09E-04	1.1178
Bonded - 10 To 10	Target	Bonded	Closed	1.83E-04	1.1129
Bonded - 25 To 25	Contact	Bonded	Closed	2.31E-03	1.6
Bonded - 24 To 24	Contact	Bonded	Closed	1.90E-03	1.6
Bonded - 11 To 11	Target	Bonded	Closed	1.80E-03	0.66451
Bonded - 12 To 12	Target	Bonded	Closed	1.63E-03	0.6617
Bonded - 8 To 8	Target	Bonded	Closed	1.65E-03	0.66157
Bonded - 11 To 11	Contact	Bonded	Closed	4.07E-04	1.6
Bonded - 7 To 7	Target	Bonded	Closed	1.28E-03	0.66121
Bonded - 8 To 8	Target	Bonded	Closed	2.56E-04	1.1179
Bonded - 8 To 8	Target	Bonded	Closed	2.59E-04	1.1171
Bonded - 8 To 8	Target	Bonded	Closed	2.78E-04	1.1127
Bonded - 8 To 8	Target	Bonded	Closed	1.73E-03	0.66127
Bonded - 8 To 8	Contact	Bonded	Closed	5.68E-04	1.6
Bonded - 8 To 8	Contact	Bonded	Closed	3.89E-04	1.6
Bonded - 7 To 7	Target	Bonded	Closed	1.45E-03	0.66139
Bonded - 7 To 7	Target	Bonded	Closed	1.81E-03	0.66101
Bonded - 10 To 10	Target	Bonded	Closed	1.54E-03	0.66393
Bonded - 10 To 10	Target	Bonded	Closed	1.61E-03	0.66094
Bonded - 10 To 10	Target	Bonded	Closed	1.82E-03	0.66577
Bonded - 11 To 11	Contact	Bonded	Closed	3.88E-04	1.6
Bonded - 9 To 9	Target	Bonded	Closed	1.61E-03	0.66179
Bonded - 11 To 11	Target	Bonded	Closed	1.75E-03	0.66145
Bonded - 9 To 9	Target	Bonded	Closed	1.64E-03	0.66098
Bonded - 9 To 9	Target	Bonded	Closed	1.78E-03	0.66188
Bonded - 12 To 12	Target	Bonded	Closed	1.80E-03	0.66113
Bonded - 12 To 12	Target	Bonded	Closed	1.29E-03	0.66342
Bonded - 24 To 24	Target	Bonded	Closed	1.36E-03	0.66493
Bonded - 24 To 24	Target	Bonded	Closed	1.78E-03	0.66405

Bonded - 24 To 24	Target	Bonded	Closed	1.36E-03	0.66113
Bonded - 24 To 24	Target	Bonded	Closed	1.52E-03	0.66099
Bonded - 25 To 25	Target	Bonded	Closed	1.65E-03	0.66135
Bonded - 25 To 25	Target	Bonded	Closed	1.41E-03	0.66185
Bonded - 25 To 25	Target	Bonded	Closed	1.34E-03	0.6614
Bonded - 25 To 25	Target	Bonded	Closed	1.30E-03	0.661
Bonded - 8 To Upstream End Plate	Contact	Bonded	Closed	0.45185	1.8335
Bonded - 7 To Upstream End Plate	Contact	Bonded	Closed	0.45187	1.8215
Frictional - 7 To 8	Contact	Frictional	Near Open	0.67053	0.7
Frictional - 9 To 10	Contact	Frictional	Near Open	0.67073	0.7
Frictional - 34 To 26	Contact	Frictional	Near Open	0.51591	0.7
Frictional - 34 To 25	Contact	Frictional	Near Open	0.51621	0.7
Frictional - 7 To 8	Target	Frictional	Near Open	0.67049	0.7
Frictional - 8 To 9	Target	Frictional	Near Open	0.67052	0.7
Frictional - 8 To 9	Contact	Frictional	Near Open	0.67056	0.7
Frictional - 9 To 10	Target	Frictional	Near Open	0.67062	0.7
Frictional - 33 To 24	Target	Frictional	Near Open	0.51623	0.7
Frictional - 33 To 23	Target	Frictional	Near Open	0.51603	0.7
Frictional - 33 To 23	Contact	Frictional	Near Open	0.51614	0.7
Frictional - 26 To 25	Contact	Frictional	Near Open	0.53122	0.7
Frictional - 26 To 25	Target	Frictional	Near Open	0.53139	0.7
Frictional - 26 To 12	Target	Frictional	Near Open	0.47151	0.7
Frictional - 26 To 12	Contact	Frictional	Near Open	0.47186	0.7
Frictional - 26 To 11	Contact	Frictional	Near Open	0.38419	0.7
Frictional - 26 To 11	Target	Frictional	Near Open	0.38381	0.7
Frictional - 25 To 11	Target	Frictional	Near Open	0.3838	0.7
Frictional - 25 To 11	Contact	Frictional	Near Open	0.38416	0.7
Frictional - 25 To 10	Contact	Frictional	Near Open	0.47185	0.7
Frictional - 25 To 10	Target	Frictional	Near Open	0.47149	0.7
Frictional - 24 To 9	Contact	Frictional	Near Open	0.47185	0.7
Frictional - 24 To 9	Target	Frictional	Near Open	0.47145	0.7
Frictional - 24 To 8	Contact	Frictional	Near Open	0.38415	0.7
Frictional - 24 To 8	Target	Frictional	Near Open	0.38373	0.7
Frictional - 24 To 25	Contact	Frictional	Near Open	0.53128	0.7
Frictional - 24 To 25	Target	Frictional	Near Open	0.53117	0.7
Frictional - 23 To 8	Target	Frictional	Near Open	0.38381	0.7
Frictional - 23 To 8	Contact	Frictional	Near Open	0.38413	0.7
Frictional - 33 To 24	Contact	Frictional	Near Open	0.51634	0.7
Frictional - 33 To 34	Contact	Frictional	Near Open	0.54954	0.7

Frictional - 33 To 34	Target	Frictional	Near Open	0.54971	0.7
Frictional - 34 To 25	Target	Frictional	Near Open	0.51614	0.7
Frictional - 23 To 7	Target	Frictional	Near Open	0.4714	0.7
Frictional - 23 To 7	Contact	Frictional	Near Open	0.47185	0.7
Frictional - 34 To 26	Target	Frictional	Near Open	0.51583	0.7
Frictional - 23 To 24	Target	Frictional	Near Open	0.53118	0.7
Frictional - 23 To 24	Contact	Frictional	Near Open	0.53154	0.7
Frictional - 12 To 11	Target	Frictional	Near Open	0.67057	0.7
Frictional - 12 To 11	Contact	Frictional	Near Open	0.67064	0.7
Frictional - 11 To 10	Target	Frictional	Near Open	0.67041	0.7
Frictional - 11 To 10	Contact	Frictional	Near Open	0.67039	0.7